Numerical Analysis of Natural Convection Heat Transfer for Windows with Porous Screening Material

by

Neil Norris

A thesis

presented to the University of Waterloo

in fulfillment of the

thesis requirement for the degree of

Master of Applied Science

in

Mechanical Engineering

Waterloo, Ontario, Canada, 2009

I hereby declare that I am the sole author of this thesis. This is a true copy of the thesis, including any required final revisions, as accepted by my examiners.

I understand that my thesis may be made electronically available to the public.

ABSTRACT

A numerical study of natural convection across a window cavity with an insect screen was performed in order to investigate the effects of changing several variables on the heat transfer through the system. A two-dimensional, laminar model was created using the Computational Fluid Dynamics software FLUENT. The system was approximated by three rectangular zones, the largest representing the open room, a smaller area with an isothermal wall representing the window cavity and a thin area representing the insect screen, which connected the two other zones. The insect screen was assumed to be a porous media with a known pressure drop taken from experimentation and the Darcy-Forchheimer equation was applied to this zone. The factors that were changed in order to examine the effects were two window cavity heights and two widths, five different screen porosities and a variety of window, screen and ambient temperature combinations.

The model was compared to analytical solutions for a vertical flat plate, as well as a qualitative analysis done through a simple flow visualization experiment for a midrange porosity of 0.5. It was found that the model matched the analytical solution very well and exhibited the same flow patterns as in the experiment.

First a non-heated screen was used, simulating nighttime conditions. Velocity vector and temperature plots were created in order to see the changes in flow patterns as the porosity of the screen was decreased for the various geometries and as the temperature between the window and screen increased. Several flow patterns were observed. For small screen/window spacing, 0.0127m, the flow is fairly uniform for all porosities and follows the entire length of the cavity, slowing in velocity for decreasing porosities. For larger spacing, 0.0254m, there are recirculation zones present, one back up the screen, and one in the bottom corner which causes the flow to exit the cavity before it reaches the bottom.

The results were then non-dimensionalized and the heat transfer rates were examined by comparing the local and average Nusselt and Rayleigh number for each model. The results showed the effects of the flow patterns on the heat transfer, with end effects jumping the Nusselt number as the flow navigates the bottom corner. These effects are lessened with decreasing porosity. The average Nusselt number also followed the same trend as flat plate correlations, but with less heat transfer.

Finally, a methodology was proposed to approximate the heat transfer as resistor network in order to simplify the heat transfer calculations into a 1-D transfer analysis for building sciences applications. Each element of the system, the window, insect screen and open room, was reduced to an isothermal layer in order to describe the system solely by temperature differences in order to find the heat transfer rates. This final step was done in conjunction with ongoing research at the University of Waterloo Solar Thermal Research Lab.

ACKNOWLEDGEMENTS

I would like to give my thanks to Professor Mike Collins, for being the easiest supervisor to get along with and whose support through this thesis and my entire time at Waterloo has been invaluable. Also thanks to Professor John Wright for helping me to keep going with this project.

I am grateful to all the students of the University of Waterloo Solar Thermal lab, Omid, Victor, Veronique, Bart, Andrew, Sebastien and Nathan for making working in the lab at a computer screen for two years actually fun.

I give my sincere appreciation to Brian Gaunt for his expertise with everything to do with lasers.

Finally, to my parents for putting up with me for past several months while I finished this writing.

TABLE OF CONTENTS

LIST OF TABLES

LIST OF FIGURES

NOMENCLATURE

ρ	density (kg/m^3)
t	time
$\vec{v}$	velocity vector (m/s)
S_m	mass source term
∇P	Pressure gradient
$\bar{\bar{\tau}}$	Fluid stress tensor
$\vec{g}$	gravitational vector
$\vec{S}$	momentum source term
E	Total energy
k_f	fluid conductivity (W/m-K)
T	temperature (K)
S_h	Energy source term
β	coefficient of volumetric thermal expansion
R	gas constant
ρ_o	ambient density
T_∞	ambient temperature (K)
μ_o	ambient viscosity (kg/m-s)
C_p	Specific heat (J/kg-K)
α	permeability
$1/\alpha$	viscous loss coefficient
C_2	inertial loss coefficient
γ	porosity
Δn	medium thickness (m)
ρ_s	solid material density (kg/m^3)
E_s	solid material energy
k_{eff}	effective conductivity (W/m-K)
k_s	solid material conductivity (W/m-K)
ϕ	general transport variable
Γ	Diffusion Coefficient
T_g	glass temperature (K)
T_s	Screen temperature (K)
Nu_x	local Nusselt number
h	heat transfer coefficient (W/m^2-K)
L	characteristic length
Ra_x	local Rayleigh number
g	gravitational constant (9.81m/s^2)
Ra_c	critical Rayleigh number
Pr	Prandtl number
Q_g	heat flux through window (W)
Q_s	heat flux through screen (W)
Q_∞	heat flux through room (W)
R_i	Resistance to heat transfer (K/W)

CHAPTER 1
INTRODUCTION

1.1 BACKGROUND

With the cost of energy increasing, and a rising population creating a strain on energy demand, it has becoming increasingly apparent that new forms of energy production, and improvements on energy efficiency must be immediately addressed in order to have a sustainable future. G-8 countries account for some of the highest energy use per capita in the world. According to a 2005 StatsCan Report [Ménard, 2005], Canada ranks 2nd among those countries in terms of energy use per capita, with 0.3407 Tera Joules per person, or more than one metric tonne of oil equivalent (TOE) per person. This large amount of energy use can be attributed to many factors, including a dispersed population, cold climate and a high level of affluence in living conditions. However, these are not excuses to neglect a movement towards better energy efficiency in Canada.

The residential and commercial-institutional sector (office buildings) account for 17% and 13%, respectively, of the energy use in Canada [Cuddihy, 2005]. The breakdown of energy consumption in these sectors by end use is shown in Figure 1.1.

As seen in Figure 1.1, the majority of energy use is in space heating and cooling. One way temperature control can be influenced is through passive solar/heat transfer techniques, where heat can be used or rejected without requiring mechanical systems. Thermal mass, solar ventilation, insulation, windows and shading devices are all examples of where passive thermal designs are used.

Insect screens are commonly found on operable windows and doors in North America. In warm summer months, heat and insects can be serious discomforts. For homes or businesses without air conditioning, having operable windows is the easiest way to regulate indoor temperature and to meet fresh air requirements. Even when air conditioners are present, often it

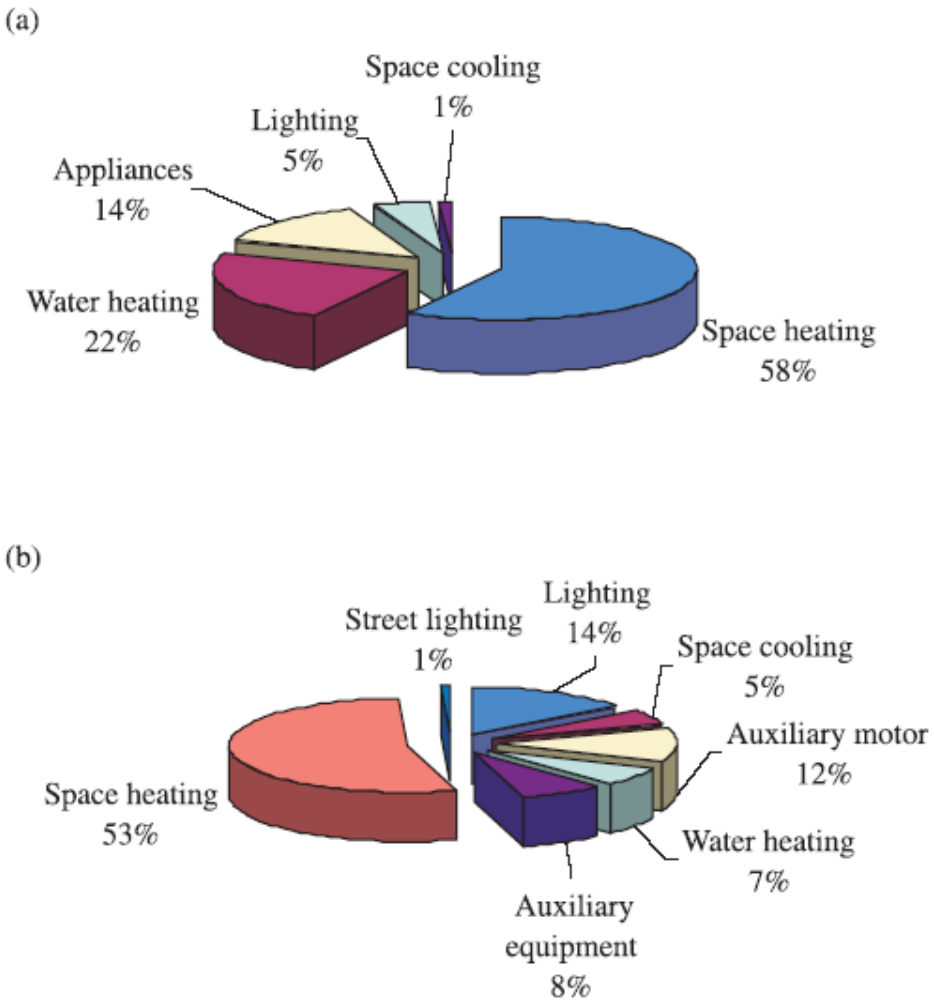

Fig.1.1. *Energy use in Canada; a) residential and b) commercial. [Cuddihy, 2005]*

is a cheaper and more reasonable alternative to simply open the windows than have an air system run constantly. By installing insect screens, the open windows or doors can allow fresh air in, while keeping bugs and debris out. Although it is not their intended usage, insect screens also serve to attenuate solar transmission in a window, and can therefore be called a shading device.

Insects have always caused problems for North American homes and since the 1800's screens have been employed on window openings to stop the spread of diseases like Yellow Fever. This still applies today, where insect screens are not only used for comfort considerations, but health as well. In North America, mosquitoes can carry potentially harmful viruses like the

West Nile Virus, where the first reported case in Canada occurred in 1999 [Public Health Agency of Canada, 2006]. The Public Health Agency of Canada suggests window screens be installed on all doors and windows in order to reduce the risk of infection. With this in mind, it is very unlikely that an insect screen would not be present on an operable window in North America.

These screens are not just used in residential homes. Some of the insect screen market is also devoted to serving the agricultural sector. In organic farming pesticide spraying is very minimal so other means of preventing insects from affecting crop yields must be used. In naturally vented greenhouses, screens are placed on all openings to prevent any insects from entering.

While keeping out insects and bringing in fresh air is the primary function of screens, they also have other effects. During the colder months of fall and winter, or whenever the windows are kept shut, rarely do people bother removing the insect screens. As a result, they can affect the heat transfer through windows since both the glass and the screen are directly between the outside and inside air.

Which type of heat transfer the screen will affect the most depends on the placement of the screen, which itself is dependent on the window configuration. Various types of residential window configurations are shown in Figure 1.2.

For the sliding and double-hung windows, the screens would be placed on the exterior side of the window. On the exterior, it is most likely that the primary mode of convective heat transfer would be forced convection due to wind. For any operable window that swings out, Awning, Hopper or Casement, the screen would be placed on the interior side. On the interior side, the primary mode of convective heat transfer would be natural convection because inside a home, the airflow has very low velocities. All of these window/screen configurations would also include radiation heat transfer.

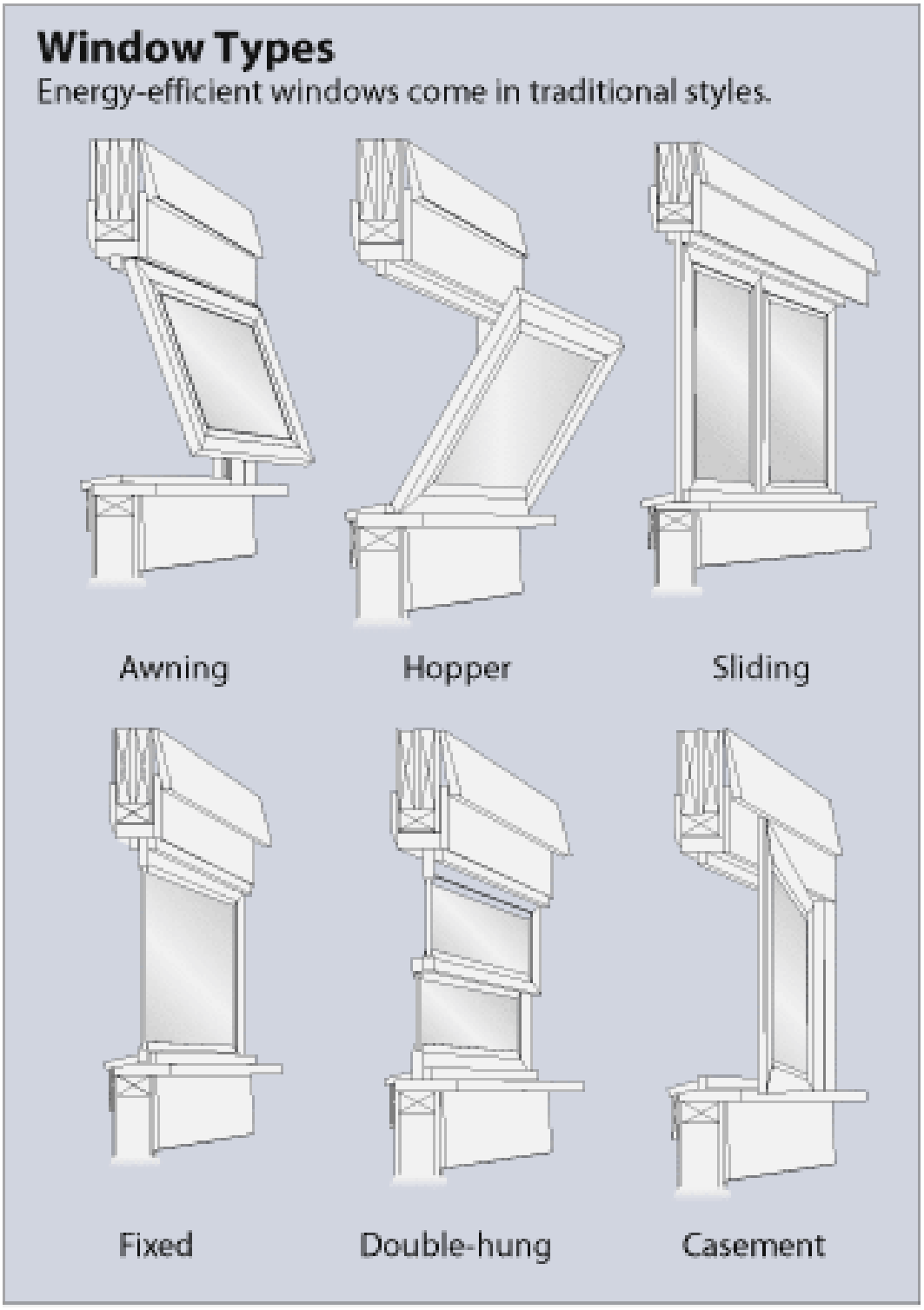

Fig.1.2. *Residential window configurations [U.S. Department of Energy, 2006]*

1.2 PRESENT WORK

The purpose of this current work is to numerically model the interaction between the insect screen and the window. The model was created to compare how different factors affect the heat transfer through the entire window configuration. For this study, the interior placed screen, dominated by natural convection, was analyzed. The results are intended to fit into the framework developed in the American Society of Heating, Refrigeration, and Air-Conditioning Engineers (ASHRAE) Research Project 1311 (RP-1311) [Wright et al., 2009] which was conducted by Profs John Wright and Mike Collins at the University of Waterloo. This project, ASHRAE RP-1311, developed new models and methodology by which windows, shaded windows in particular, could be included in the energy analysis of buildings. With regards to convective heat transfer, the current work will eventually be reduced to a thermal resistance network.

Computational fluid dynamics (CFD) can be used to predict the physical behaviour of airflows. CFD is a method where numerical models are used to analyze fluid flows by attempting to solve fundamental equations like the Navier-Stokes equations. The program used to create this model, Fluent, is a CFD software package offered by ANSYS, Inc. which uses the finite volume method. This involves creating a meshed domain, representing a physical geometry, with discrete points located inside. Surrounding each point is a small volume which is connected to other nodal volumes by their faces. Physical values for each node are calculated using the surface fluxes at the faces between the nodes and the boundary conditions for the limits of the domain. For more information on the finite volume method used, see Section 2.2.

Using CFD over experimentation is a common alternative since CFD can be very accurate, especially for simple flows, and is often more cost effective. Changing parameters using CFD (geometry shape, material properties, flow conditions etc.) is much easier than creating a new experimental setup each time a new condition is required. This reduces the time and cost for developing a system. However, the CFD results still need to be validated in some form in order to ensure that the physics of the system are being correctly modelled. Experimentation is very useful in conjunction with CFD for this purpose.

1.3 PREVIOUS WORK

Studies have been done to address how insect screens function and their effects on fluid flow. These studies are discussed below.

In Brunger et al. [1999], the effects of adding an insect screen to a window was investigated experimentally from a solar and thermal resistance sense in order to get a general impression for how insect screens should be included in energy rating systems. A single black fibreglass screen was used on a 1.495m (4Ft, 11in) high window, mounted 0.0254m (1in) away from the panes. For both the interior and exterior cases, 18 tests were performed using varying indoor and outdoor temperatures, high or low outdoor wind speeds and with and without solar irradiance to simulate day and night time conditions. From these tests two building sciences parameters, the solar heat gain coefficient (SHGC) and U value, were found for with and without the insect screen. The SHGC is the fraction of the radiative heat from sunlight that can pass through a window, indicated by a value between 0-1 where a higher number means more heat that can pass through. The U value is the overall heat transfer coefficient and is a measure of how well a system transfer's heat through itself. For building design it is used to determine heat loss, where the lower the U value, the more resistance there is to heat transfer. In this study, it was found that by having a screen on the outside, the SHGC is reduced by 46% and the U value is reduced by 7%. For cold climates this means that in the heating season, less heat is coming in from the sun through the window, but also slightly less heat is transferred out of the home. For the indoor case, the SHGC and U value was decreased by 15% and 14% respectively. The conclusion was that indoor screens can be kept on year round, while outside screens should be taken down during the winter months. Either way, screens were shown to have a significant impact on window performance. However, it was also noted that for the interior screens, since the U value is decreased, and the screens are not a moisture barrier, the inner glass pane is colder and condensation can cause a problem.

Miguel et al [1997], conducted several experiments on a variety of insect screens and shading materials in order to determine how to predict airflow through them. It was assumed that the screens acted like a porous media. For porous media flow, the Darcy-Forchheimer equation

from Forcheimer [1908], can be used, which relates velocity flow with the pressure loss across the material and the permeability, which is a measure of how well a material transmits fluid (For more information on the Darcy-Forchheimer equation, see Chapter 2.1.3). A test apparatus was constructed in order to find the pressure drop across the screen as air was forced through it. These experimental results were compared to the Darcy-Forchheimer equation and were found to be in good agreement, concluding that insect screens can be modelled as a porous medium.

In a follow up study, Miguel [1998 b], several screening materials were again tested for the pressure loss, however this time the relationship between air velocity through the screen and pressure drop was simplified into a second order polynomial equation. With experimental results organized this way, the permeability was not explicitly needed in order to define the screen characteristics. This is a much more useful form when inputting material properties into Fluent.

The majority of CFD studies using insect screens are focused on greenhouse simulation and the climate changes inside the greenhouse by adding insect screens on the natural ventilation. In Bartzanas et al [2002], the finite volume method was used to determine the airflow inside a tunnel greenhouse. The insect screen was treated like a porous media, the same approach as Miguel et al [1997], where the permeability and inertial factors were used to define a single insect screen. These values were used at the inlet and outlet, where the screens were placed, as boundary conditions for the incoming and outgoing air. From this simulation, velocity and temperature profiles were found for the airflow, including the influence of wind, however this was solely forced convection that was studied.

Similarly, in Fatnassi et al [2006], the optimization of a multispan greenhouse using insect screens was studied using both experimentation and CFD. For the experimentation, a miniature model was created and N_2O tracer gas was used to track the fluid flow. For the CFD simulation, the insect screen was again considered to be a porous media. Using the permeability, an overall pressure loss coefficient was determined using the Darcy-Forsheimer equation, which was then treated like a pressure sink in the governing equations (see Chapter 2 for more information). Like the Bartzanas study, air velocity and temperature profiles were found for the forced convection on the greenhouse.

In the solar lab at the University of Waterloo, work is currently being done to analyze heat transfer through windows for a variety of shading devices, like blinds, screens and drapes. The intent of the project is to model these shading devices in terms of radiation and convective heat transfer in order to create a straightforward and practical energy analysis of buildings that incorporate single or multiple window attachments. The approach taken for these models is a multi-layered framework and is detailed in Wright et al [2009], where each shading device is analyzed separately for various properties and then incorporated together as an overall system. The system is treated like a series of parallel layers, separated by air gaps and is shown in Fig 1.3.

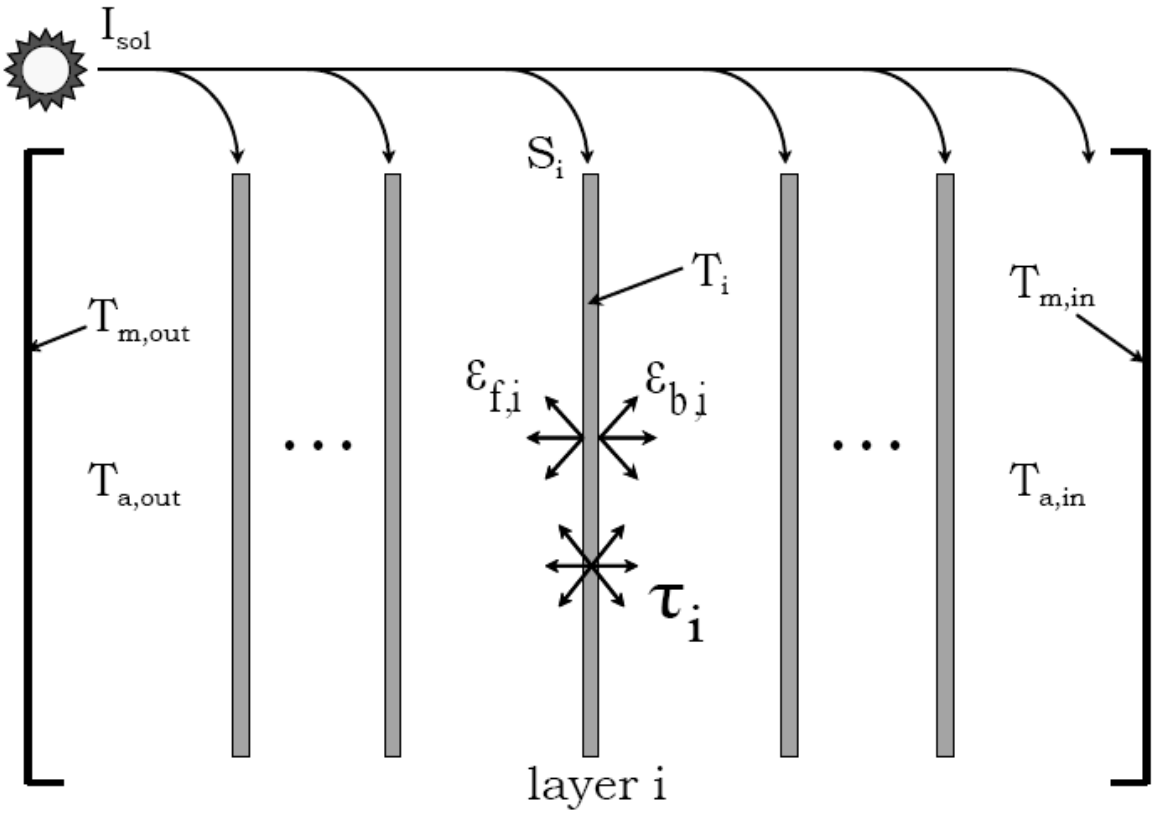

Fig.1.3. *Multi-Layer Structure [Wright, 2009]*

This multi layer structure requires a two-step analysis. First, the flux of absorbed solar radiation at each layer, S_i, caused by the incident flux, I_{sol}, is determined using the transmittance, τ, of the layer. Second, an energy balance is applied at each layer, accounting for heat transfer

across the system using the known set of S_i values and the material emissivity, ε, in order to obtain the set of layer temperatures, T_i, and the corresponding heat flux values.

Currently the majority of research has been developed on the radiation side of this project, which is used to calculate S_i. In Wright & Kotey [2006], a method for determining the solar optical properties of these shading devices was formulated and in Wright et al [2009] these methods were used to determine the material properties of drapes, roller blinds and insect screens in terms of radiation heat transfer. It was found that the emittance and transmittance of the materials were functions of porosity.

Further work is being done for this project in order to determine the heat transfer as part of the second step of the multi-layer system. In Collins & Wright [2006], the diathermanous layer system (window and shading device) was reduced to a thermal resistor network, where each path for heat flow contains a resistance to heat transfer. This resistance is simply the inverse of the heat transfer coefficient, h_c or h_r, depending on if the transfer is through convection or radiation. The heat flux through the system is described using a series of equations with the surrounding temperatures, the resistance value of the layer and the ambient conditions. An example of a thermal resistance network is shown in Fig.1.4.

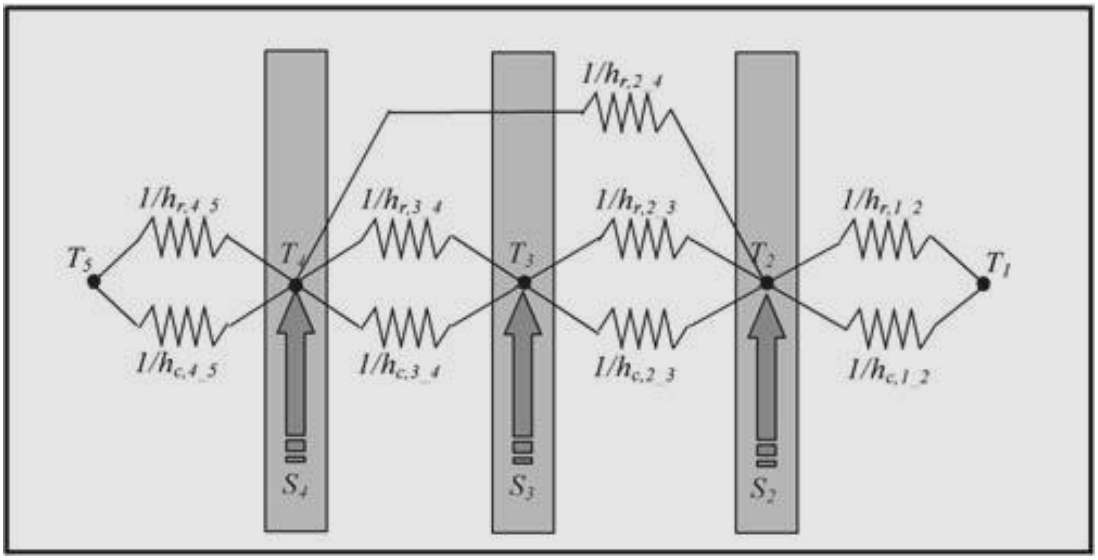

Fig.1.4. *Example of diathermanous resistance network for a double glazed window*

This current work uses this approach and is a further progression to these previous models, and the proposed methodology in Section 4.4 is intended to fill in the convection side of the heat transfer specifically for insect screens. From the CFD results, the heat fluxes can be found for each particular condition and the resistance values can be calculated using the resistance network equations. With correlations developed, the heat flux can be determined for any temperature set. For more information on the resistance network and determination of the resistance values for this model, see Section 4.4.

1.4 PROJECT SCOPE

Previous studies have shown how the window energy ratings can be impacted by insect screens, and how screens can affect forced convection in large open areas, however no in depth studies have been done to find the direct interactions between windows and insect screens. The overall goal of this study was to create a numerical model to determine what effects were based on the following parameters. First, there is the temperature difference between the interior and exterior air. This difference changes over the seasons in North America and is the main driving force for natural convection, which determines the magnitude of heat transfer. Also, insect screens come in varying porosities, which is a measure of how open a screen expressed as the fraction of screening material to open air. The porosity directly affects the amount of heated or cooled air that can pass through the screen. The porosity is given as a value between 0 and 1, where 0 is completely solid and 1 is completely open. The porosity and pressure drop characteristics of several screens were provided in Miguel [1998 b]. In that study, several screening materials of identical porosities but different wire geometries were tested to find the effects of yarn shape and mesh geometries have on air characteristics for a given porosity, γ. For instance, in Miguel [1998 b], there were two screens tested with a porosity of 0.63, yet the screens had two different wire diameters of 0.12mm and 0.45mm. In order to have the same porosity, yet different wire diameters, the smaller wire diameter screen would need to have more wire meshes present in the screen. This would decrease the pore size (size of the openings between the wires) and could potentially cause different air flows through these screens. Despite this, the two screens were still found to have almost identical pressure drops and it was concluded that these geometry factors have negligible influence on the pressure drop, at least for

the screens tested. It must be noted, however, this still can play a significant difference on the heat transfer, because of different surface areas. Since the pressure drop and porosity data used in this project has been taken from Miguel [1998 b], it has been assumed that the airflow through the screen can be considered a function of porosity only and not influenced by the wire geometry. The final variables examined were the window height and the sill size, which is the distance between the window and the screen. Varying these sizes changes the aspect ratio of the domain. The aspect ratio is important, especially when non-dimensionalizing the results. The aspect ratio also changes the physics of the domain and can produce a wide variety of flow patterns by changing this parameter. For further model parameter details, see Chapter 2.3.

In analyzing the data, first the dimensioned results were studied for flow patterns and other qualitative aspects of adding insect screens to a window. These are shown in Chapter 4.2. Then the data was non-dimensionalized so that the results from this study can be more widely compared to other geometries. The non-dimensionlization method is detailed in Chapter 2.12 and results are shown in Chapter 4.3. For the dimensionalized and non-dimensionalized results, the screen was in thermal equilibrium with the flow around it and only applied a pressure drop. In the final section, a proposed method of adding a heated screen was introduced and the system was simplified into a resistor network based on the work done in Collins & Wright [2006]. This simplification allows this current work to be integrated into the shading models that are being developed at the University of Waterloo. The resistor network methodology is shown in Chapter 4.4.

CHAPTER 2

GOVERNING EQUATIONS AND MODEL PARAMETERS

2.1 GOVERNING EQUATIONS

2.1.1 MOMENTUM, ENERGY AND THE NAVIER-STOKES EQUATIONS

The Navier-Stokes Equations represent the fundamental relationships used in analyzing fluid flow. Based on Newton's Laws of motion, they relate mass, momentum and energy together with fluid stresses in order to solve for the flow field. The Navier-Stokes equations for the conservation of mass, momentum and energy in a fluid are given in Eq.2.1, Eq.2.2 and Eq.2.3 respectively.

$$\frac{\partial \rho}{\partial t} + \nabla \bullet (\rho \vec{v}) = S_m \qquad 2.1$$

where ρ is the density, t is time, $\vec{v}$ is the velocity vector and S_m is a mass source;

$$\frac{\partial}{\partial t}(\rho \vec{v}) + \nabla \bullet (\rho \vec{v} \vec{v}) = -\nabla P + \nabla \bullet (\bar{\bar{\tau}}) + \rho \vec{g} + \vec{S} \qquad 2.2$$

where ∇P is the pressure gradient, $\bar{\bar{\tau}}$ is the fluid stress tensor, $\vec{g}$ is the gravitational vector and $\vec{S}$ is the momentum source term;

$$\frac{\partial}{\partial t}(\rho E) + \nabla \bullet (\vec{v}(\rho E + P)) = \nabla \bullet (k_f \nabla T + (\bar{\bar{\tau}} \bullet \vec{v})) + S_h \qquad 2.3$$

where E is the total energy, k_f is the thermal conductivity, T is the temperature and S_h is the energy source term.

These equations are the backbone of fluid flow studies and have been well established. An abundance of information is available on their development. These equations have been derived in many forms and those presented here are in a form that the CFD program, FLUENT, solves.

2.1.2 NATURAL CONVECTION AND THE BOUSINNESQ APPROXIMATION

Natural or free convection is a mode of heat transfer that occurs between a surface and a moving fluid, where the motion is created by buoyancy and gravitational forces acting on density gradients within the fluid. In natural convection the velocity is not forced by an external source besides the body forces, thus there is no motion in the freestream. Most commonly the density gradients are caused by temperature differences. In a heated fluid, warmer material becomes less dense than the surrounding cold fluid and rises due to buoyancy. Similarly, cooler fluid will fall due to an increase in density. The density changes in a substance due to temperature can be described using a material property called the coefficient of volumetric thermal expansion, β. For an ideal gas, β is given by

$$\beta = -\frac{1}{\rho}\left(\frac{\partial \rho}{\partial T}\right)_P \approx -\frac{1}{\rho}\frac{\rho_o - \rho}{T_o - T} = \frac{1}{\rho}\frac{P}{RT^2} = \frac{1}{T} \qquad 2.4$$

Here R is the gas constant and ρ_o is the gas density corresponding to the ambient temperature T_o. Eq.2.4. can be rearranged into the form

$$(\rho_o - \rho) \approx \rho\beta(T - T_o) \qquad 2.5$$

which gives the Boussinesq approximation. This approximation states that for small temperature differences, the density variations are very small, and density can be treated as a constant except for in the buoyancy forces when the density is multiplied by gravity, where it is inversely related to temperature by β. In natural convection flow, since there are no external gradients, the pressure forces are part of the buoyancy and gravitational forces. It follows that,

$$\nabla P = \rho_o \vec{g} \qquad 2.6$$

Combining Eqs.2.5 and 2.6 with the momentum equation, Eq.2.2, eliminates ρ from the buoyancy term and gives

$$\frac{\partial}{\partial t}(\vec{v}) + \nabla \bullet (\vec{v}\vec{v}) = -\rho_o \beta (T - T_o)\vec{g} + \frac{\nabla \bullet (\bar{\bar{\tau}})}{\rho_o} + \frac{\overrightarrow{S}}{\rho_o} \qquad 2.7$$

The flow in this model was assumed to be two dimensional, laminar (see Section 2.6 for details) and in steady state. With these assumptions, Eq.2.3 and Eq.2.7 can be further simplified for boundary layer flow against the heated window. The heated window in this model was assumed to be a flat plate and derivations of this boundary layer flow have been well established. Expanding the momentum equation gives the *x* and *y* momentums in Eq.2.8 and 2.9 respectively and the boundary layer energy equation is given in Eq.2.10.

$$v_x \frac{\partial v_x}{\partial x} + v_y \frac{\partial v_x}{\partial y} = g_x \beta (T - T_o) + \frac{\mu_o}{\rho_o} \frac{\partial^2 v_x}{\partial y^2} + \frac{S_x}{\rho_o} \qquad 2.8$$

$$v_x \frac{\partial v_y}{\partial x} + v_y \frac{\partial v_y}{\partial y} = \frac{\mu_o}{\rho_o} \frac{\partial^2 v_y}{\partial x^2} + \frac{S_y}{\rho_o} \qquad 2.9$$

$$v_x \frac{\partial T}{\partial x} + v_y \frac{\partial T}{\partial y} = \frac{k_f}{\rho_o C_p} \frac{\partial^2 T}{\partial y^2} + \frac{S_h}{\rho_o} \qquad 2.10$$

where v_x and v_y are the velocities in the *x* and *y* direction, μ_o is the viscosity, C_p is the specific heat of the fluid and g_x, β, T_o, ρ_o, μ_o and C_p are all constants. Since temperature appears in both the momentum and the energy equations, they must be solved simultaneously.

2.1.3 POROUS MEDIA MOMENTUM EQUATIONS

For this model, the same approach that was used in Miguel [1998 b] was employed, and the insect screen was assumed to be a porous medium. Darcy's Law is the primary relation in analyzing flow through porous media and is shown by

$$\nabla P = -\frac{\mu}{\alpha}\vec{v} \qquad 2.11$$

Darcy's Law relates the transfer of momentum to the permeability and the pressure loss through the medium, similar to how Fourier's Law treats heat conduction. The permeability, α, is a measure of how well fluid is transmitted through a material and is a property of the porous media, not the fluid. Permeability is based on pore characteristics and the flow path and is difficult to calculate without experimentation. In this model, the reciprocal of the permeability, $1/\alpha$, is termed the viscous loss coefficient.

For Reynolds number flows ($\mathrm{Re} = \rho v \alpha^{1/2} / \mu$) higher than unity, Forchheimer [1901] acknowledged the existence of a non-linear flow regime and as a result, Darcy's Law alone was insufficient to describe the pressure loss. The equation was modified with a squared fluid velocity term which includes a pore inertia coefficient that is a function of permeability, porosity and pore characteristics. Instead of a pore inertia term, FLUENT simplifies the equation with the use of a single inertial loss coefficient C_2, which is characterized as a loss per unit length in the flow direction. The Darcy-Forcheimer equation is

$$\nabla P = -\frac{\mu}{\alpha}\vec{v} + C_2 \frac{1}{2}\rho \vec{v}|v| \qquad 2.12$$

In FLUENT, the pressure loss through the porous media is handled as an added momentum source term (in this case a sink), which is included in the S term in Eq.2.2. The general form is shown in Eq.2.13. The pressure drop in a given direction can be related to the source term by simplifying the momentum equation, as shown in Eq.2.14.

$$S_i = -\left(\frac{\mu}{\alpha} v_i + C_2 \frac{1}{2} \rho |v| v_i\right) \qquad 2.13$$

$$\Delta P_i = -S_i \Delta n_i \qquad 2.14$$

where the *i*th subscript represents the x or y direction and Δn is the thickness of the medium in the *i* direction. The solid region in the screen is not modeled with the porous media approach in FLUENT; instead it is the momentum sink that creates the pressure drop in the porous zone instead of the volume blockage. Based on Eq.2.13, in defining the insect screen, the only information required are the viscous and inertial loss coefficients $1/\alpha$ and C_2. As stated before, these coefficients are difficult to define without experimentation and for this model the coefficients were determined using data from Miguel [1998 b]. This process is shown in Section 2.3.5.

2.1.4 POROUS MEDIA ENERGY EQUATIONS

In porous media regions, the energy equation, Eq.2.3, is modified in the transient and thermal conductivity terms. The modified energy equation is

$$\frac{\partial}{\partial t}(\gamma \rho_f E_f + (1-\gamma)\rho_s E_s) + \nabla \bullet (\vec{v}(\rho_f E_f + P)) = \nabla \bullet (k_{eff} \nabla T + (\bar{\bar{\tau}} \bullet \vec{v})) + S_{fh} \qquad 2.15$$

In this equation, the subscripts *f* and *s* represent values for fluid and solid. γ is the porosity, which is the volume fraction of fluid inside the porous region.

$$\gamma = \frac{V_f}{V_T} \qquad 2.16$$

Where V_f is the volume of fluid, in this case air, and V_T is the total bulk volume of fluid and solid in the porous medium. This corresponds to a value between 0-1, where 1 is completely open (no screen) and 0 is completely closed (solid wall). Since this model deals with steady-state only, the

transient terms drop out and the solid material properties ρ_s and E_s are not required. The thermal conductivity in Eq.2.3, k_f, has been replaced by k_{eff} by being treated as a volume average between the fluid and solid conductivities in the porous media,

$$k_{eff} = \gamma k_f + (1-\gamma)k_s \qquad 2.17$$

For night time conditions, when the screen is in thermal equilibrium with the surroundings, the inputted porosity was set to 1 so the effective conductivity is equal to the fluid conductivity, thus the screen for this condition is thermally non-participating. The actual porosity of the screen is not directly required for this model; however, the effect of porosity on momentum is contained within the pressure drop and porous media coefficients $1/\alpha$ and C_2. When the screen is heated and maintained at a constant temperature, an assigned heat transfer and temperature difference accounts for the heat transfer between the screen and the material, so again the porosity was set to 1. This way no additional material information for the screen is needed to calculate the heat transfer through the porous media.

2.2 FINITE VOLUME METHOD

The finite volume method is a process where numerical integration schemes are used over small control volumes in order to solve the Navier-Stokes equations. A series of nodal points are placed around the geometry. Boundary faces are placed mid-way between each of the nodes, such that each node is surrounded by a control volume cell. The governing equations are integrated over this control volume in order to solve for the flow field.

The governing equations given in section 2.1 can be more generally written for the finite volume method as the transport equation for ϕ,

$$\frac{\partial(\rho\phi)}{\partial t} + div\,(\rho\phi v) = div(\Gamma\, grad\,\phi) + S_\phi \qquad 2.18$$

where ϕ is a general variable which can be used to represent various fluid properties, such as temperature or momentum and Γ is the diffusion coefficient, which can represent coefficients like thermal conductivity, *k*. In words, Eq.2.18 can be more easily explained for a single control volume as

Rate of Increase of ϕ of fluid element	+	Net rate of flow of ϕ out of fluid element	=	Rate of increase of ϕ due to diffusion	+	Rate of increase of ϕ due to sources	

Eq.2.18 is integrated over the control volume in order to yield a discretised equation for the various flow properties. This has the advantage of having an equation with a clear physical interpretation where the fluxes of ϕ entering and exiting the control volume have to be balanced.

In order to solve the convection of ϕ, the magnitude and direction of the velocity field is required, however for the majority of problems, the velocity and pressure gradients are not known beforehand and a solution algorithm is needed. The solution algorithm determines how the flow field is calculated across the entire model geometry. What are known initially are the boundary conditions, like a heated surface or a wall, which can be used as a starting point for the calculations. Difficulty arises when trying to determine how to calculate pressure and velocity since these entities are coupled. Various solution algorithms use a guess and correct method for determining the pressure and velocity across the grid based on the boundary conditions. An example of this is the SIMPLE algorithm, and its procedure is shown in Fig.2.1.

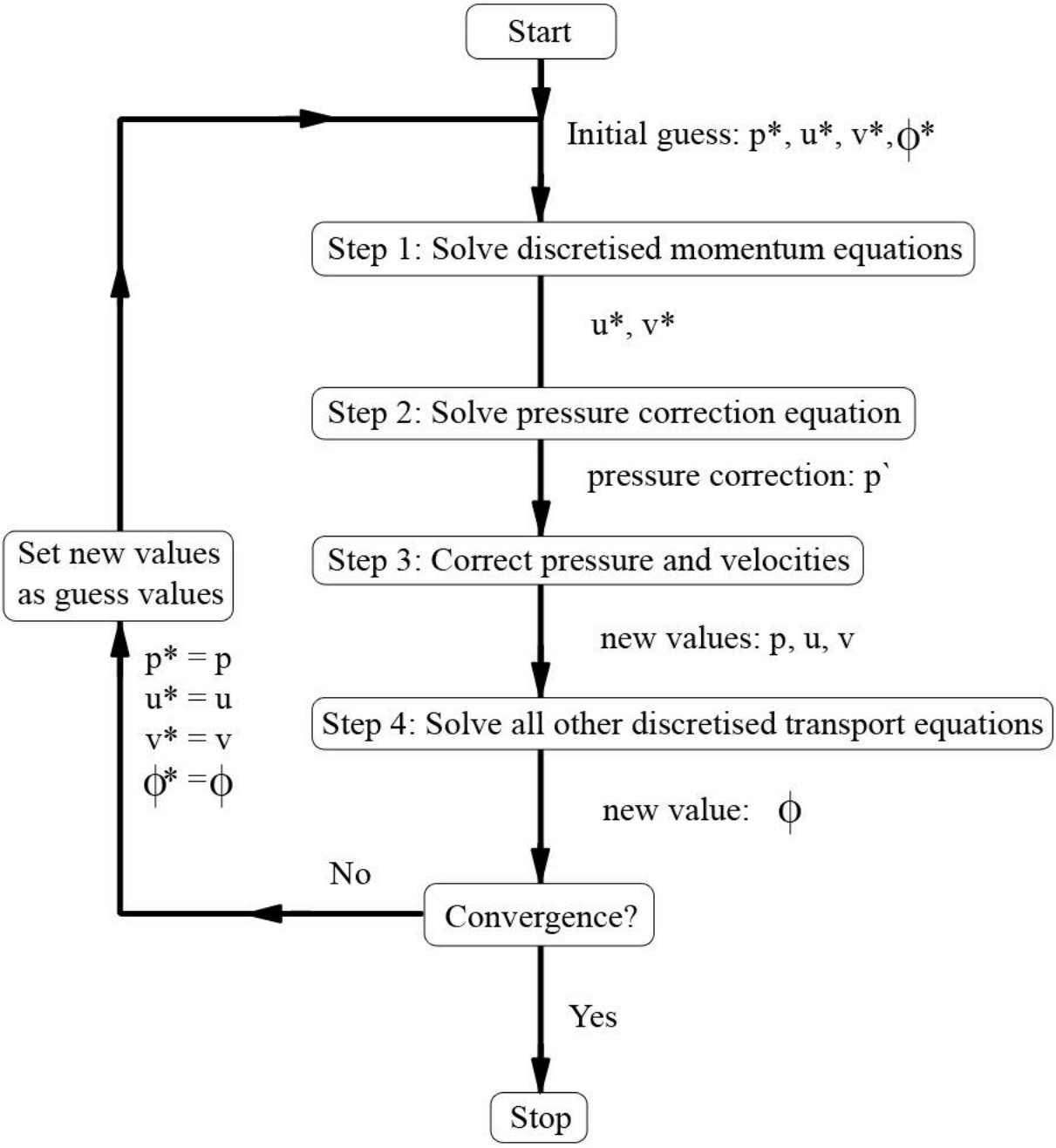

Fig.2.1. *SIMPLE algorithm solution process*

SIMPLE uses an iterative process by which an initial guess is made for the flow field properties. The discretized momentum equations are then calculated in the control volumes. Pressure and velocity corrections are found based continuity imbalances in the control volume that arise when the guessed values do not correctly match the boundary conditions. These corrections are used in calculating new pressure and velocity values which replace the guessed values. The rest of the flow properties are then recalculated using the new pressure and velocities which are then cycled back to the start of the process and the solution algorithm is run again. This continues until the results are converged, which is when the residuals, a measure of the overall conservation of flow properties, are very small. This convergence criteria, how small the residuals have to be, is usually set by the user and depends on the problem type as well as the expectations from the model.

2.3 MODEL PARAMETERS

2.3.1 GEOMETRY

Windows and window cavities come in a variety of sizes and configurations. In order for greater flexibility, the geometry was kept simplified. No turning mechanisms, grooves or window/screen framing were modelled. This was primarily done to decrease the computational time and so that the results could have a broader applicability.

In this regard, the domain consisted of two rectangular areas, the larger representing the open air of the room, and the smaller representing the window cavity. Two window heights were investigated; 0.61m (2ft) and 1.22m (4ft). Both of these are typical window sizes that would have insect screens attached. Also, two sill sizes, the distance between the window and the screen, were investigated; 0.013m (0.5in) and 0.025m (1in). By changing the window height and sill size, the aspect ratio of the window is altered, which is a very useful way of non-dimensionalizing the problem so that these results can be compared to other window sizes. The results are not intended to be applied to tall products such as patio doors. Four geometric models were created using the ANSYS modelling program GAMBIT (with two window heights and two sill sizes). The four models and their dimensions are shown in Fig.2.2 and Fig.2.3.

Fig.2.2 *Window Models, 0.6096m Height. All Dimensions are in metres.*

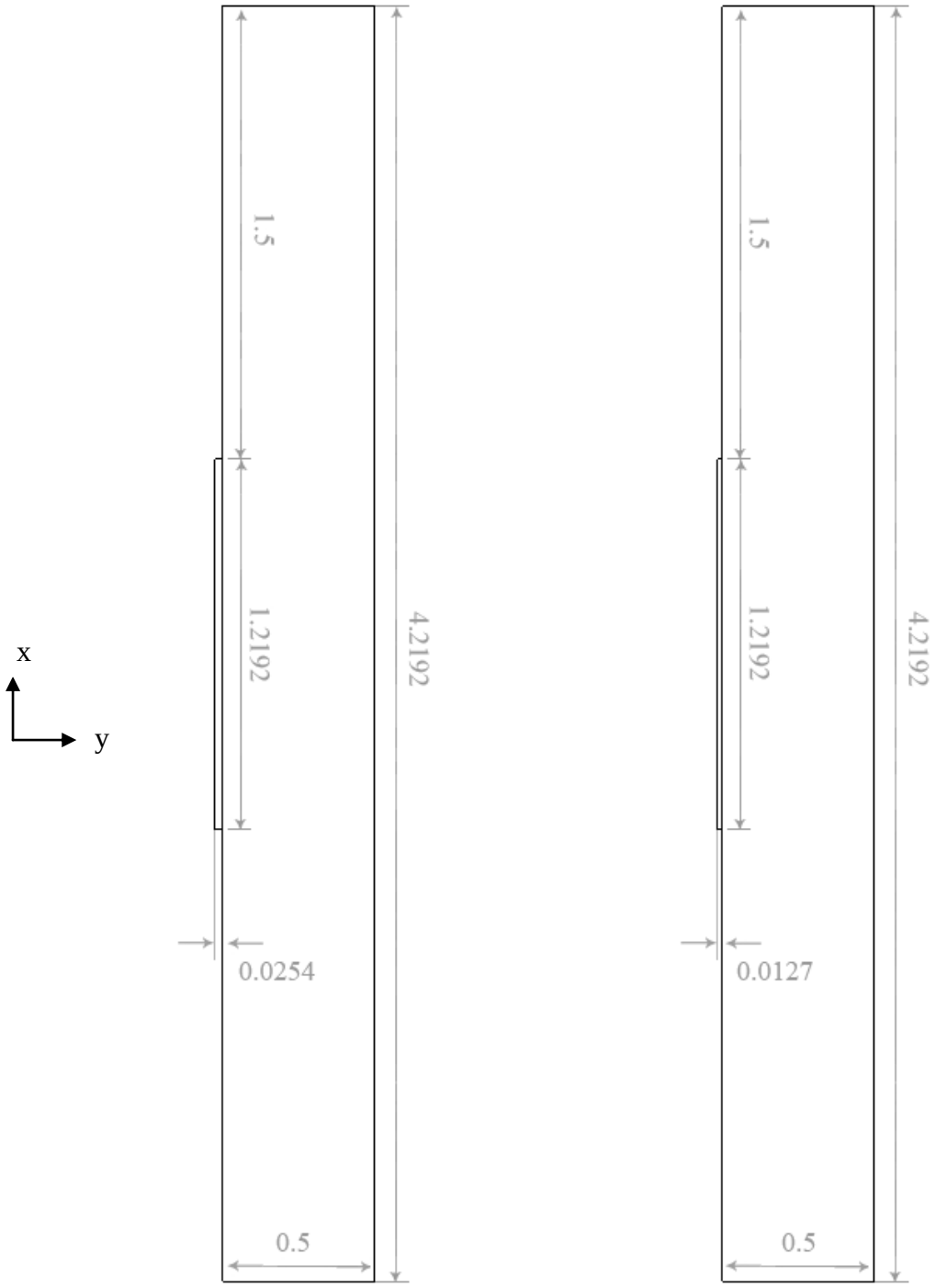

Fig.2.3 *Window Models, 1.2192m Height. All Dimensions are in metres.*

Through repeated trials it was found that the dimensions for the open air cavities given in Figure 2.2 were the most appropriate sizes. For CFD models, having too large a domain can greatly slow computational time by calculating excess and unneeded data. In this case in an open room where airflow should be zero, for a large domain the flow values and temperatures are still calculated far from the window and screen, which has no bearing on the flow inside the cavity. On the other hand, having too small of a domain can impact the results. A small domain may cut off a developing flow structure which can have upstream effects or can change the physics such that what originally was modelled is no longer accurately represented. The sizes used in Fig.2.2 and 2.3 were the smallest that could be used without affecting the flow inside the window cavity based on the temperatures and conditions used in this simulation.

The two rectangular cavities in the model geometries are connected by a very thin area, highlighted in Fig.2.4, which represents the insect screen. It is in this area where the porous media equations are used and is present on all four models. Insect screens come in a wide variety of thicknesses, all of which depend on the material used and how they are manufactured. Typically they range between 0.1-0.3 mm for polyester and aluminium screens. Rather than create a new geometry for every screen, a constant thickness of $\Delta n = 0.25$mm was used for the porous media zone. The difference between this and the actual screen thickness is accounted for in the calculation of the porous media coefficients, shown in Section 2.3.5, which governs the flow through the porous media zone.

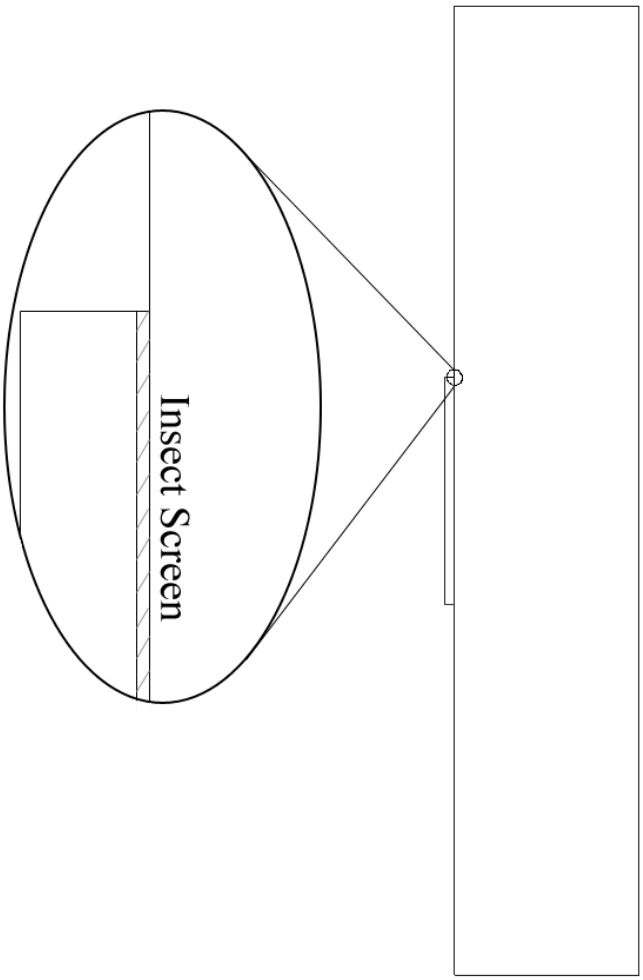

Fig.2.4. *Porous Media zone*

2.3.2 MESHING

The geometric models were meshed using the modelling program GAMBIT and a detailed view of the meshing is shown in Fig.2.5. Each area is meshed separately; however their connecting borders between areas must match in nodal spacing so that the finite volume method can be used. Since the boundary nodes must match, the areas were meshed in order of importance in the model.

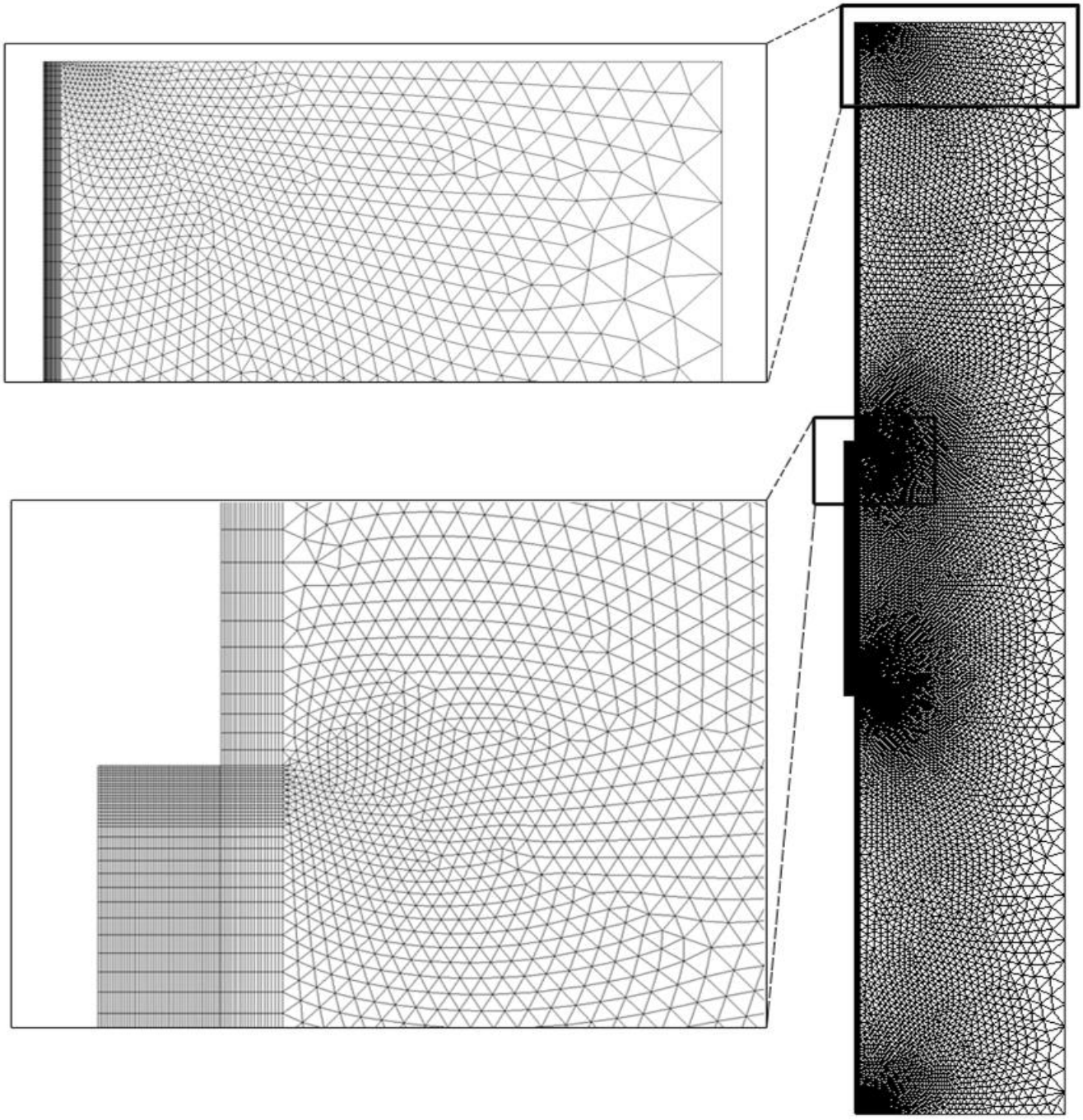

Fig.2.5. *Examples of meshing used*

The first meshed area was the window cavity zone, where the flow is created and where the majority of the data is analyzed. An inflated boundary layer was placed along the window side and the top and bottom walls representing the sill. An inflated boundary layer is one in which rectangular meshed volumes are created which increase in width with distance from with each new volume. An inflated boundary layer is useful in solving boundary layer flows close to walls. Also, because of its straight uniformed structure, it is much easier to interpret the velocity profiles close to the wall since all the nodes are located along a single horizontal line, unlike an unstructured mesh. This inflated boundary layer extended to the porous zone, so that the model would also be able to handle boundary layer flows along the screen when the screen is heated. Along the height of the window, the nodes were spaced in a bell shaped ratio, where there are a greater amount of nodes at the top and bottom, and less in the centre. This was done since it was expected that the area where the flow would most greatly change would be where the flow is turned and exits the cavity, which is at the top or bottom depending on the temperature inputs. This area warrants a greater amount of meshed volumes so that these changes can be accurately modelled. The porous zone was meshed in the same manner; however, for the width of the porous zone, only one volume was used. The size of the porous zone compared to the other areas is quite small, so splitting this area into smaller meshed volumes negatively affects the convergence and increases computational time. The fine details of the velocity inside the screen are not required; the porous zone is there only to apply the insect screen pressure drop on the flow. As a result, more volumes in this area are not necessary and one volume is enough to apply this condition.

The last meshed was the open air zone, where the flow exits the domain. Another inflated boundary layer was used along the entire left side of the open air zone, matching the window and porous zone in spacing. Outside of the inflated boundary layer, a non-uniform triangular mesh was used with a successive ratio where fewer volumes are created moving from right to left across the zone. Since in this area there is not boundary layer flow, the non-uniform mesh helps with convergence.

Since the four geometric models have different dimensions, the fine details in the meshing are also different. The general layout, however, as is explained above, is the same.

Overall, for the four geometric models, between 46694 and 53671 volumes were created. These meshings were found to be the most appropriate spacing for the objectives of this project. A grid dependency analysis was performed and is shown in Section 3.2. For a more comprehensive look at the meshing details for each geometric model, see Appendix A.

2.3.3 BOUNDARY CONDITIONS

The boundary conditions set on the geometric model are shown in Fig.2.6. Any non-labelled surface shown was treated as an adiabatic wall with a no-slip condition.

The window was treated as a no-slip wall with a constant temperature along its surface. This provides the driving force for the flow. FLUENT can calculate the amount of heat transfer through this boundary and produce the heat transfer coefficients needed for comparisons.

The pressure boundaries on the top and bottom of the open air zone set a pressure at these extremities. Both pressures were set to 0 Pa so that no external gradients were created and the flow is only generated by the temperature difference in the domain. Identical pressure boundaries achieve better convergence in natural convection cases compared to other methods, such as setting a velocity inlet/outlet to 0 m/s.

A zero-gradient condition was placed on the right boundary. It is sufficiently far enough away from the window that the natural convection does not affect anything near this boundary and the air in the open room zone is essentially still. Therefore it is safe to assume the zero-gradient condition since no mass or heat will be transferred out of this boundary. In FLUENT, this condition is inputted as a ‘symmetry’ boundary. This used when the flow/thermal pattern is expected to have a mirror image where no flux quantities are transferred across the boundary. For this case, the symmetry boundary acts as a zero-gradient, even though realistically there is not another window cavity on the other side of symmetry boundary layer.

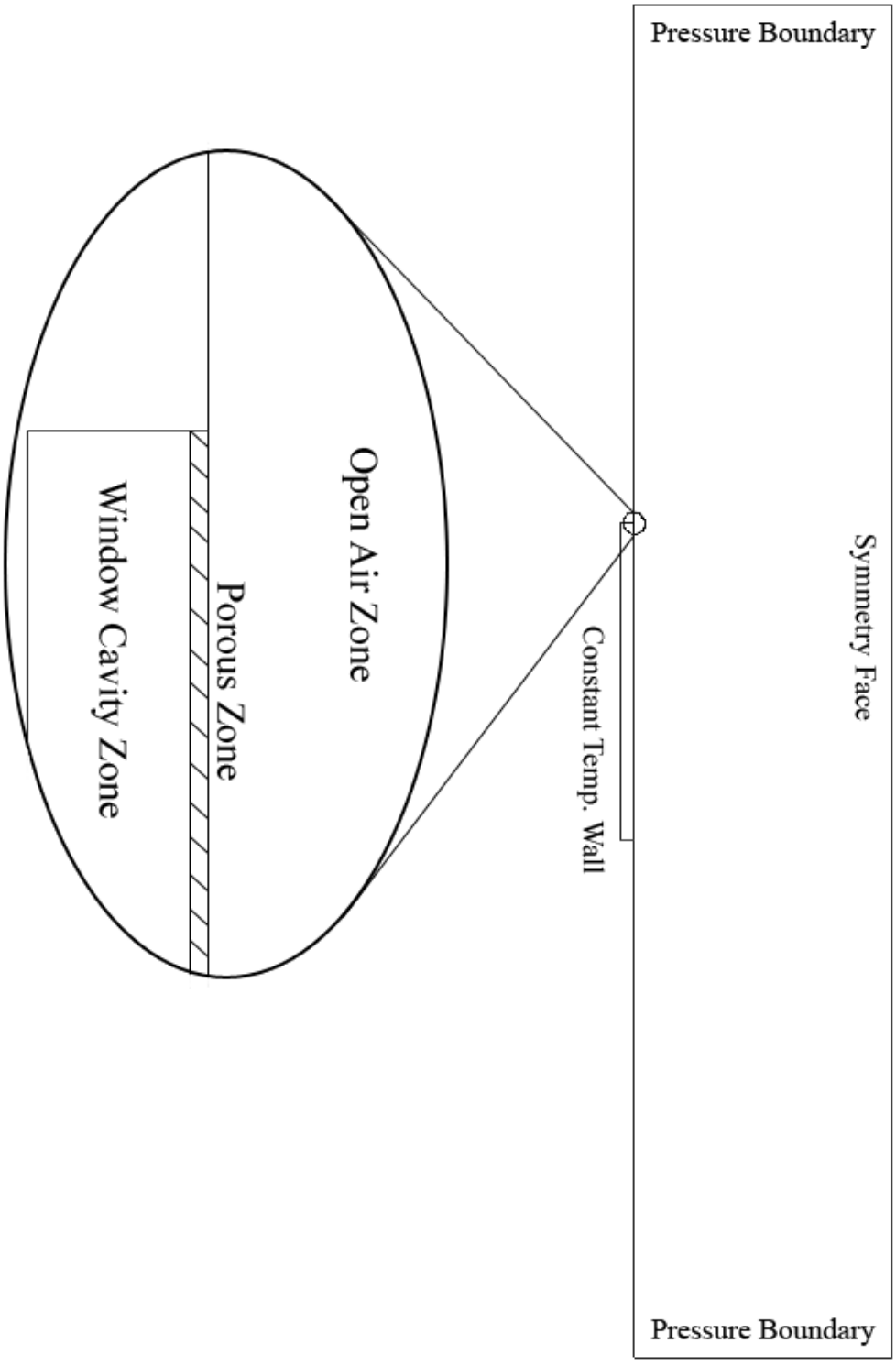

Fig.2.6. *Boundary Conditions. Any non-labelled surface can be considered an adiabatic wall*

2.3.4 TEMPERATURE DIFFERENCES

Three sets of temperature differences were used, between the window and the indoor ambient temperature, as shown in Table 2.1.

Table 2.1. *Temperature Differences Used*

Ambient T_o (K)	**Window T_g (K)**	**Difference ΔT (K)**
296	281	-15
296	290	-6
296	302	6

The window temperature T_g was set at the constant temperature window boundary, while the ambient temperature T_o was set as the initial domain temperature and at the pressure boundaries, which is required in case of any backflow.

The window temperatures were chosen based on outdoor temperatures for the city of Waterloo, ON Canada given by the University of Waterloo weather station, adjusted to meet typical window glass temperatures (i.e., even when the outdoor temperature is below 0^oC, the interior glass temperature would still be significantly higher). The ASHRAE Standard 55-2004 recommends indoor temperatures be set as 298K and 294K for heating and cooling seasons respectively. An intermediate 296K constant interior ambient temperature was used for this model.

2.3.5 INSECT SCREEN CHARACTERISTICS

For the porous zone, six different conditions were used. These corresponded to four types of insect screens of varying porosities as well as the no screen and fully enclosed situations. Miguel [1998 b], found the pressure drop, ΔP, through the screen could be defined using the flow velocity, u, in a second order polynomial equation:

$$au^2 + bu = \Delta P \qquad 2.19$$

The values a and b are characteristics of the screen and were found by fitting Eq. 2.19 to data from experimentation. These values and other characteristics were calculated in Miguel [1998 b] and, for the screens analyzed in this work, are shown in Table 2.2.

Table 2.2. *Screen Specifications and best fit equation for second order polynomial ($au^2 + bu = \Delta P$) Miguel, 1998 b*

Sample	**Description**	**Yarn Width (mm)**	**Porosity γ (m^2/m^2)**	**a**	**b**	**Correlation coefficient r^2**
Rw25	Woven screen regular mesh	0.25	0.25 ± 0.010	18.015	17.712	0.99
R50	Polyester regular mesh	0.20	0.50 ± 0.009	1.556	2.503	0.99
R63	Rectangular mesh	0.12	0.63 ± 0.015	0.911	2.285	0.98
Rw90	Woven screen regular mesh	0.10	0.90 ± 0.022	0.352	1.548	0.97

In order to be usable in this model, the screen characteristics must be defined by the viscous loss coefficient, $1/\alpha$, and inertial loss coefficient, C_2. From the porous media equations given in Section 2.1.3, Eq.2.12 can be compared to the second order polynomial given by Eq.2.19. It can be seen that a and b corresponds to the coefficients in front of the velocity terms, giving the following when rearranged:

$$\frac{1}{\alpha} = \frac{b}{\mu \Delta n_i} \qquad 2.20$$

$$C_2 = \frac{2a}{\rho \Delta n_i} \qquad 2.21$$

Using Eq.2.20 and Eq.2.21, the data given in Table 2.2 and the thickness of the porous zone where the pressure drop is applied (Δn = 0.25mm) the viscous and inertial loss coefficients for the insect screens were found and are shown in Table 2.3.

Table 2.3 *Viscous and Inertial Loss Coefficients*

Screen	**1/α (1/m^2) x10^{-8}**	**C_2 (m^2) x10^{-3}**
R_{w25}	30.97	119.300
R_{50}	5.60	10.304
R_{63}	5.12	6.034
R_w90	3.47	2.334

2.4 SOLUTION PARAMETERS

For solving the governing equations, the pressure based non-segregated algorithm SIMPLE-C was used. This algorithm obtains the pressure field by using a relationship between velocity and pressure corrections based on some initial guessed pressure field to enforce mass conservation, as explained in Section 2.6. The solution method is slightly different than SIMPLE in how it corrects for velocity, but the solution procedure is the same as what is presented in Fig.2.1. Since this flow is laminar and two dimensional, Zeng, et al [2003], suggests that SIMPLE-C is more robust and achieves faster convergence than other algorithms available in FLUENT.

In order to interpolate the values at the faces, the body-force weighted PRESTO! method was used for pressure and second order schemes were used for calculating momentum and energy. These are all commonly used in solving natural convection simulations.

2.5 CONVERGENCE CRITERIA

The residual limits, the minimum value the residuals much reach before convergence, were set in this model according to the values shown in Table 2.4. If the model converged to this minimum in less than an hour, the calculations were allowed to continue until at least an hour had passed, or the residuals levelled off and no longer decreased.

Table 2.4. *Residual Limits*

Continuity	X-Momentum	Y-Momentum	Temperature
$1e^{-6}$	$1e^{-6}$	$1e^{-6}$	$1e^{-8}$

For natural convection problems, since the majority of the flow is in the vertical direction and because of the velocity coupling, the Y-momentum and continuity are the most important residuals to converge. In order to help achieve convergence for the larger geometries, initially a low Rayleigh number was used by setting an initial window temperature close to the ambient. A lower Rayleigh number situation is more likely to converge faster because the buoyancy forces

are not as large. If initially the buoyancy forces are too large, it can lead to instabilities and the continuity residuals may not converge. After the lower Rayleigh flow converged, the temperature difference was increased, and the flow field was recalculated using the new flow field as the initial guess. This was done until the temperature difference was set to what was desired. Once each no screen condition model was completed for each temperature difference and geometry, this flow field was used as the initial guess for the 0.90 porosity model. Following this, the 0.90 flow field was used as the initial guess for the 0.63 model and so on. This greatly decreased the computational time for each model instead of iterating from the beginning each time.

2.6 NON-DIMENSIONALIZATION EQUATIONS

Since there are several geometries and conditions present in this work, in order for each model to be compared to each other, the results have to be non-dimensionalized. In natural convection flows, the two parameters for heat transfer that are most commonly compared are the Nusselt and Rayleigh Numbers.

The local Nusselt Number is interpreted as a dimensionless temperature gradient or the ratio of the convective to the conductive heat transfer at a surface at some point along a surface. It is defined regularly as

$$Nu_x = \frac{hx}{k_f} \qquad 2.22$$

Where h is a proportionality constant called the heat transfer coefficient and and k_f is the thermal conductivity of the fluid. x is the distance along the leading edge, so for instance along a heated flat plate, x would be the distance from where the heating begins.

The Rayleigh number is a product of the Grashof and Prandtl numbers and compares the buoyancy and momentum forces to the viscous forces and thermal diffusivity of the fluid. The Rayleigh Number is used to define the transition of natural convection flow from laminar to turbulent. The Rayleigh number is given as

$$Ra_x = g\beta(T_g - T_{oo})x^3 \cdot \frac{Cp \cdot \rho^2}{\mu \cdot k} \qquad 2.23$$

where g is the gravitational constant, β is the coefficient of volumetric expansion and T_g and T_∞ are the surface and ambient temperatures respectively. Cp is the specific heat, ρ is the density, μ is the viscosity and k is the thermal conductivity, which are all material properties.

In order to maintain the validity that this model is in laminar conditions, the Ra number was calculated for each of the model conditions and compared to the critical Ra number, Ra_c, where the transition to turbulence occurs. Ra_c is determined experimentally, and as a result it is very difficult to find the critical conditions in cavities with insect screens since there is very little literature available. As a limiting end, when the porosity of the screen is 1, the window should act like a heated flat plate, which has been extensively studied.

The critical Rayleigh number for a flat plate is $Ra_c \approx 10^9$. Any value above this begins to enter the transition region. The stability and transition effects for vertical flat plates using this critical value were extensively discussed in Gebhart [1988]. In order to find the maximum Ra number in the 1.0 porosity cases used in this model, x in Eq.2.23 has been replaced by a characteristic length L, which for flat plates is the total length of the plate, since the maximum Ra should occur at the bottom of the window cavity. The maximum Rayleigh number for each model is shown in Table 2.5.

Table 2.5. *Critical Rayleigh Number for 1.0 Porosity Models*

L (m)	T_g (K)	T_{oo} (K)	Ra_L
0.6096	281	296	3.915E+08
0.6096	290	296	1.456E+08
0.6096	302	296	1.325E+08
1.22	281	296	3.138E+09
1.22	290	296	1.167E+09
1.22	302	296	1.062E+09

For the 0.61m window height and 100% porosity, all the model conditions were found to be less than the critical value. For the 1.22m window height, the majority of the window remains below Ra_c for each of the temperature differences. However, at the lower portions of the window, the Ra value approaches and slightly exceeds Ra_c. For ΔT = 6, -6 and -15K, Ra reaches Ra_c at 0.03, 0.06 and 0.3m from the bottom of the window cavity. Despite entering the transition region, all the conditions still match very closely with laminar flat plate correlations. See Chapter 3 for more information on flat plate correlations. It must also be noted that if the boundary layer flow off the window extends to the screen (which occurs in the small sill depths), the roughness of the screen could also have a potential effects on the flow, where a very rough wire could increase the potential of entering into transition; however the flow velocities in this model are very low and the wire diameters are so small that it is unlikely to have a major effect.

CHAPTER 3

MODEL VERIFICATION AND FLOW VISUALIZATION

3.1 INTRODUCTION

A grid dependency study was done to confirm the appropriateness of the mesh sizing and distribution. The model results themselves have been checked qualitatively via simple flow visualization experiments, and quantitatively via accepted analytical correlations that were found in the literature. Details of those efforts are provided in the following sections.

3.2 GRID DEPENDENCY STUDY

For a grid dependency study, changes in a key parameter are observed as the number of grid meshes is increased. When the observed parameter is still very noticeably changing when the grid is increased, there are too few meshes, and some key physical changes in the system maybe be missed since the grid spacing may be too large to pick them up. At a certain point of grid sizing, the parameter should either meet accepted values, or if that is unknown, should stop noticeably changing. After this point, there are too many meshes, which will only add to computational time without any significant benefit to the precision or accuracy of the model.

In choosing the correct parameter, there were a few considerations. For this model the main concern is the heat transfer, thus most appropriately the Nusselt number should be observed. In order to use accepted values for comparison, the 1.0 porosity case was chosen. As stated before, the porosity of the screen is a measure the openess of the screen. The anticipation for this current work was that the results for varying porosities would be contained between the two ends: 0 porosity, where no air would pass into the cavity and the system, would behave like

an enclosure and 1.0 porosity, where there is no insect screen and the window would act like a vertical flat plate.

Similar to the critical Rayleigh number discussion in Section 2.6, it is difficult to verify the heat transfer values for the entire CFD model since there is very little literature or work available on insect screen heat transfer that is appropriate for comparison. However, the vertical flat plate has been well established by experimentation and analytical solutions, and was used as a basis for comparison for the grid dependency study.

For a flat plate, the laminar boundary layer profiles were determined by Ostrach [1953] using a similarity analysis. From that similarity solution, the following can be derived

$$Nu_x = \left(\frac{Ra_x}{4 \cdot Pr}\right)^{\frac{1}{4}} g(\mathrm{Pr}) \qquad 3.1$$

g(Pr) is an acknowledgement that the temperature gradient at the surface is a function of the Prandtl number, where the Prandtl number is defined as

$$Pr = \frac{Cp \cdot \mu}{k} \qquad 3.2$$

Le Fervre [1956] correlated the *g(Pr)* function in the following form

$$g(\mathrm{Pr}) = \frac{0.75 Pr^{1/2}}{\left(0.609 + 1.221 Pr^{1/2} + 1.238 Pr\right)^{1/4}} \qquad 3.3$$

This correlation was found to be within 0.5% and applies for $0 \leq Pr \leq \infty$. It must be noted that since this correlation was developed analytically, this correlation is based on the local Nu and Ra numbers, not the average values.

This flat plate correlation was then compared to the local Nusselt number for 3 different grid sizing. This comparison is shown in Fig.3.1. Nu_x and Ra_x values were determined by taking the local *h* values and their corresponding lengths from the leading edge (taken directly from the CFD program) and inserting them into Eq.2.22 and Eq.2.23. The grid outside the window cavity has a very minimal affect on the heat transfer inside the cavity. Outside there is almost no significant flow changes, even with the outflow of the air from the cavity. The main meshing that affects the heat transfer is inside the cavity, close to the window. Therefore, the meshing that was refined was inside the window cavity. These are the meshing numbers that are presented in Fig.3.1.

It can be seen that at 3500 elements, the trend does not exactly follow the Ostrach solution and over predicts the Nusselt number. The tail end that breaks off from the ostrich solution is where the flow meets the bottom of the cavity and has to navigate a step, hence the divergence from the flat plate correlation. When the meshing is increased to 6375 elements, the data follows very well with the Ostrach solution. When compared to the smaller meshing case, the tail end effects are quite different, where the smaller case has a much larger jump in the Nusselt number at the end. When the meshing is increased to 10000 elements, there is not much change, and again, there are slightly smaller end effects than the 6375 case, and much smaller than the 3500. Also with this case, the computational time has greatly increased, taking over an hour to complete. From this study it can be seen that 6375 elements is the most appropriate size to use.

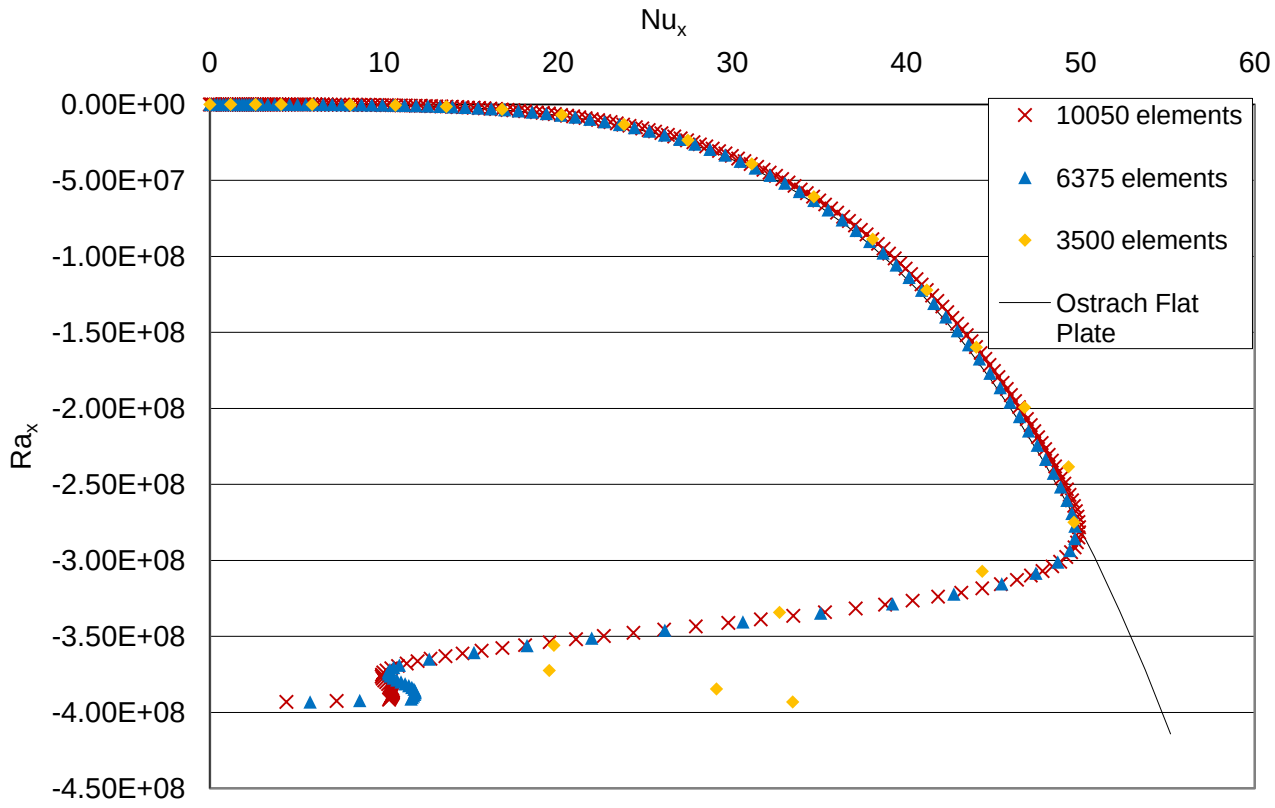

Fig.3.1. *Grid dependency on the local Nusselt number along window for 0.6096m height, 0.0254m sill and 1.0 porosity, compared to Ostrach flat plate solution.*

It must be noted that this was only looking at the local Nusselt number. For this project, the majority of the analysis is in local values and the in the flow structures that occur. For averaged values of Nusselt, these differences in end effects and deviation from the Ostrach solution have very little effect and the averaged Nusselt values are very similar. Therefore, if future use of this model involves averaged values, and flow structure is not a concern, it may be in better interest to use a less fine grid in order to reduce the computational time.

3.3 COMPARISON TO ANAYLITICAL RELATION

In order to validate results, the end limit of the 1.0 porosity case was again compared to the Ostrach solution. This time, however, it was compared against the 1.0 porosity case for all temperature differences and geometries. The combined Ostrach correlation and the model results are shown below for 0.0254m and 0.0127m sill depths in Fig.3.2 and 3.3 respectively. For these plots, the Rayleigh numbers for negative temperature differences have been taken as absolute in order to be compared with positive temperature differences. The solid markers represent the 1.22m height while the outlined markers represent the 0.6096m height.

In both the 0.0254m and 0.0127m sill length cases, all the temperature differences follow the flat plate solution with very good agreement along the correlation curve. Since the correlation is for flat plates, it does not take into account the end sill depth. The CFD results include the sill; hence the tail ends of the Nusselt number trail off for each of the model conditions as the flow reaches the end of the cavity and navigates around it.

In the other limiting case, when the porosity is 0%, it was expected that the system would act like an enclosure; however current enclosure relations do not accurately reflect the same physics that are modelled here. Enclosure relations are usually developed through experimentation where there are two walls of different, but constant, temperatures, enclosed top and bottom by two adiabatic walls. The heat transfer is then calculated between these two heated walls. In this model, without a screen that is heated by an external source, the temperature of the 0% porosity screen is allowed to fluctuate, transferring heat into the open room which acts as an infinite reservoir, while the window is the only wall that remains at a constant temperature. In addition, when the porosity reaches 0%, FLUENT does not treat this boundary as a wall, rather it still treats it as a fluid with a large pressure drop that prevents movement. This can affect the heat transfer as it is fluid to fluid, not fluid to solid. Thus because of these reasons, it would be inappropriate to validate this model using current enclosure correlations. This is also why porosities under 0.25 were not included in this model.

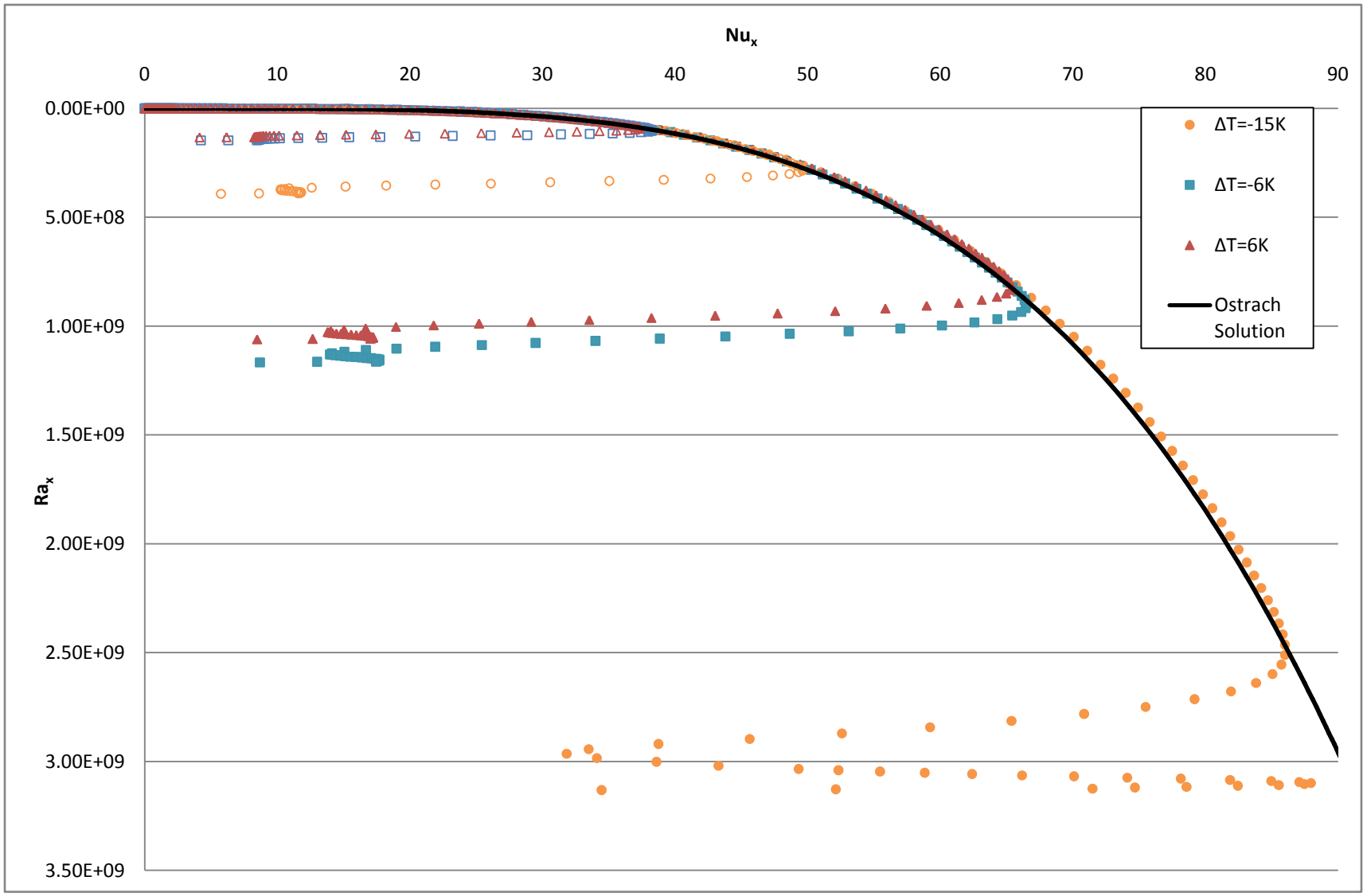

Fig.3.2. *Nu vs Ra: 0.0254m sill depth CFD Model results for 100% porosity and the Ostrach Flat Plate correlation (Ostrach, 1953).*

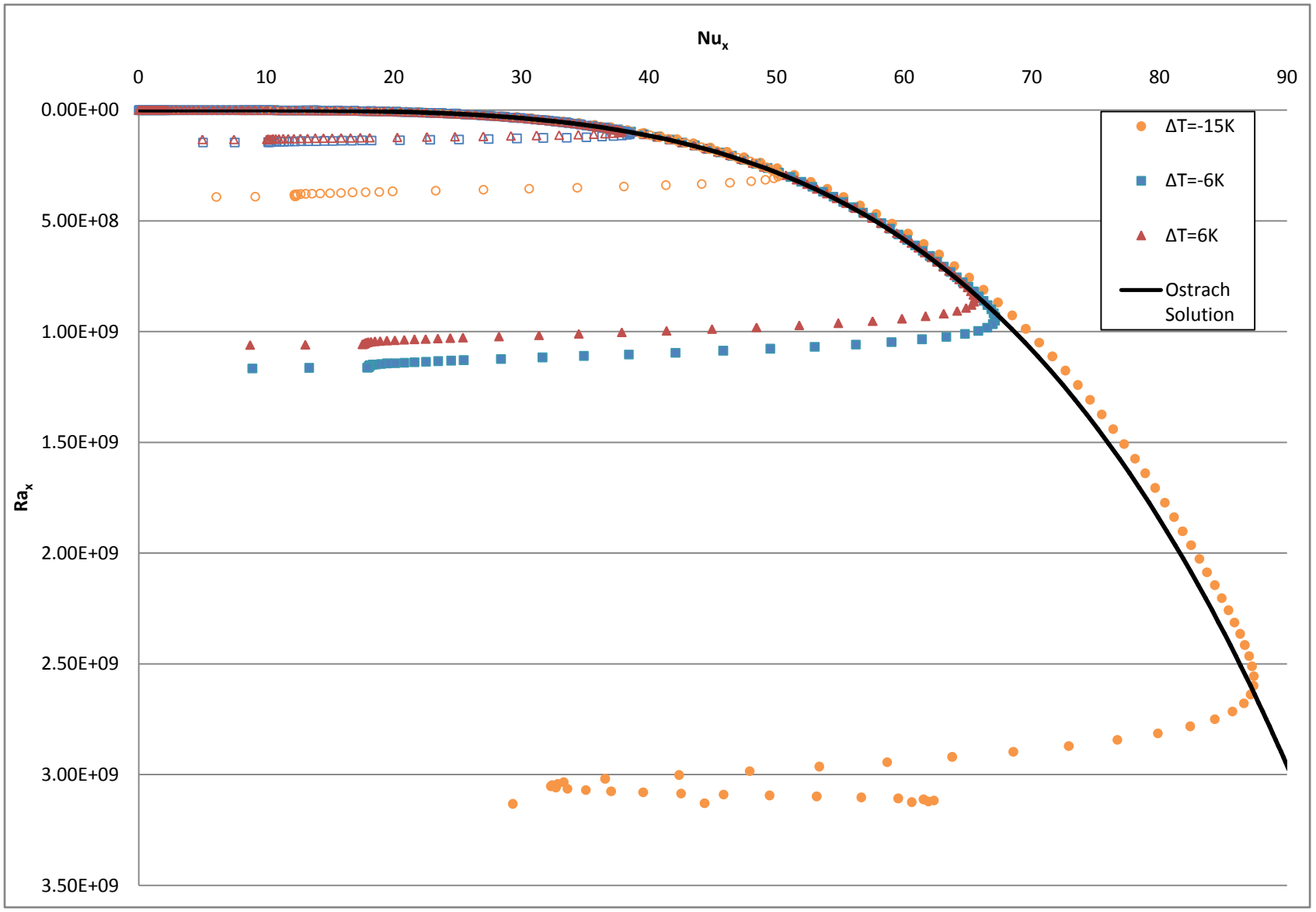

Fig.3.3. *Nu vs Ra: 0.0127m sill depth CFD Model results for 100% porosity and the Ostrach Flat Plate correlation (Ostrach, 1953)*

3.4 FLOW VISUALIZATION

In the previous section, the results for the end point of the model, 100% porosity were verified using an analytical solution. In order to gain more confidence in the model, a simple flow visualization experiment was created in order to qualitatively verify that flow structures were being accurately captured by the CFD model for porosities less than 100%.

3.4.1 EXPERIMENTAL SETUP

A window cavity with an insect screen was constructed and attached to a heated plate where smoke was used to trace the air flow along the screen. A low power laser was used to illuminate the smoke and photographs were taken of the flow patterns using a Nikon D50 D-SLR camera. The experimental setup is shown below in Fig.3.4.

The experiments were conducted in an isolated room previously used for fire simulations. The air vents were closed so that there was no air circulation in the room and were only opened if the seeding smoke became too concentrated. The room temperature was kept constant at 295 K (as it is set for the entire building), which was confirmed using a LaCrosse TX6U Wireless Temperature Sensor, and the temperature differences were created by changing the temperature of the heated flat plate.

The vertical flat plate consisted of a rear insulated metal plate filled with fluid channels and was attached to a temperature bath. Using water as the fluid, the temperature bath heated the fluid and circulated it through the flat plate in order to give it a constant temperature. In the CFD model, a cold window temperature was used with a warmer indoor temperature, however for the experimental setup, it was found to be easier to use a hot window temperature with a cooler room temperature, while still maintaining the same temperature difference. Since natural convection

Fig.3.4. *Experimental Setup*

flows on a flat plate are invertible for similar Rayleigh numbers, it was assumed that the same flow patterns could be observed. The temperature bath was set at two temperatures, 310K and 321K in order to test two differences of 15K and 26K. Unfortunately at a 6K temperature difference there was difficulty in obtaining reasonable photos, possibly because of the very low flow velocities, so they have been omitted.

The window cavity was created using three pieces of insulated foam, to act as adiabatic walls, and one piece of acrylic glass in order to view the cavity in profile. The cavity is shown in Fig.3.5.

Fig.3.5. *Experimental Window Cavity*

The foam and glass was cut to match the dimensions of the 0.61m window height and 0.026m sill length and were glued together. The insect screen was attached to a small aluminum frame and a slot was cut out of the insulated foam so the insect screen and frame could be slid into the window cavity. The screen itself was made of fibreglass with a porosity of 0.5 and a thickness of 0.22mm. The window cavity was mounted on the heated plate using four bar clamps on each corner.

The smoke used to visualize the flow was created with an insect repellent coil. The coil was placed under the window cavity and the smoke was entrained through the screen and along the heated plate. The smoke was illuminated using ILT 5500a Class IV Argon Laser. The laser placement is shown in Fig.3.6.

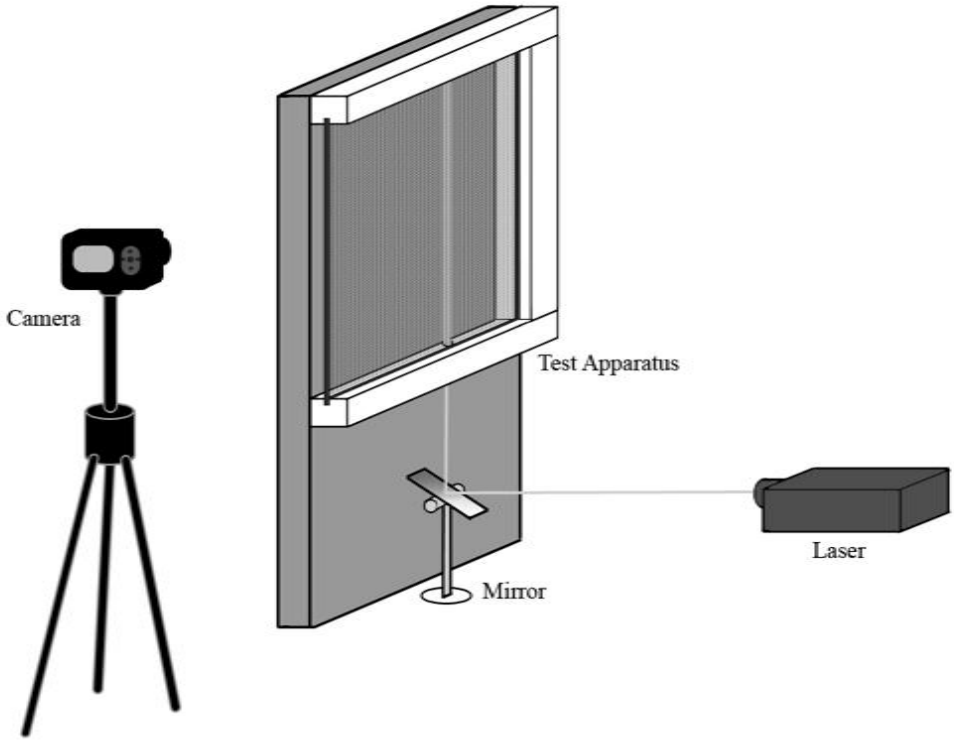

Fig.3.6. *Laser Placement*

The laser was placed perpendicular to the plate. The screen interfered with the laser when it was aimed directly into the cavity by creating shadows, so the laser had to be aimed beneath the cavity. A front surface mirror was used to reflect the beam upwards. A small hole was drilled into the bottom of the cavity which allowed the re-directed beam to enter without being blocked. A small concave piece of optical glass was placed over the hole in order to fan out the beam so the entire cavity could be illuminated. The camera was placed in line with the cavity and flat plate and was aimed through the acrylic glass as shown in Fig.3.7.

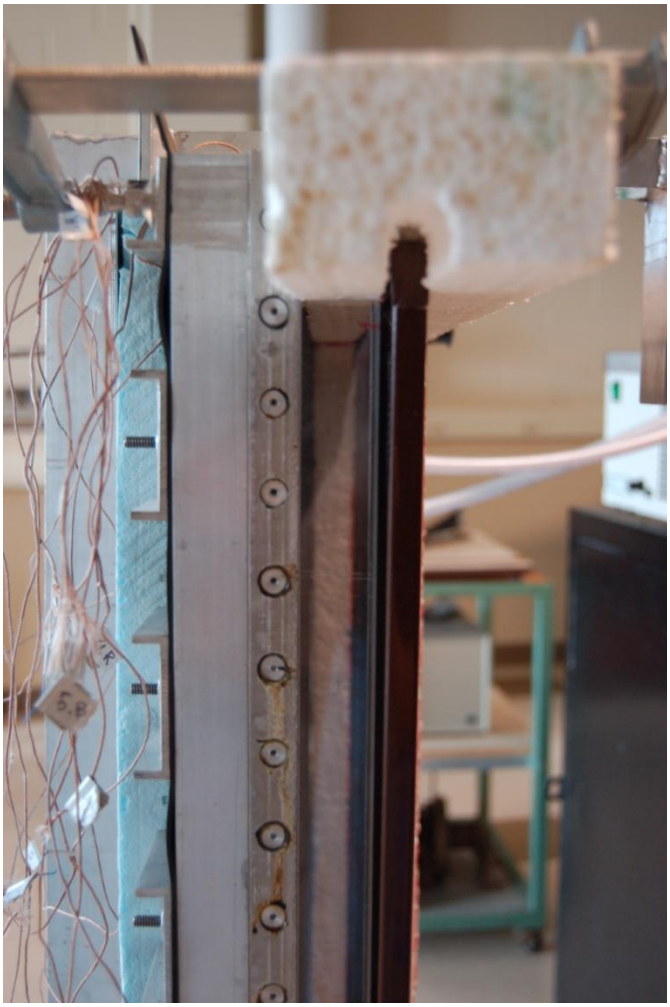

Fig.3.7. *Camera Alignment*

3.4.2 PHOTOS

The geometries examined in this work all have very large aspect ratios, so as a result visualization of the flow in the entire cavity is difficult to present, therefore the pictures taken focused on the top 20cm of the cavity, matching the velocity diagrams given in Chapter 4. The photos are presented with their corresponding velocity diagram from the CFD model for comparison. Additional photos are presented in Appendix B. Note again that these photos have been inverted to match the velocity diagrams.

From Fig.3.8, the profiles match up fairly well for a 15K temperature difference. The main body of the flow follows smoothly downward and exits the window cavity. There is a region of very slow moving air in the bottom left corner, which is likely why there are no smoke streaks in that area. In the top right corner, a turn in the flow can be seen in both the visualization and CFD results. Similarly, in Fig.3.9, the profiles again match well for a 26K temperature difference. A recirculation zone can be faintly seen in the visualization, and there is a very small area where this appears in the CFD results as well, though it is of very low velocity. From these photos it can be seen that qualitatively, the experimental and model flow exhibit similar flow structures. This was a simple qualitative experiment, only meant to examine the flow for similar patterns. A more quantitative approach, like particle image velocimetry or interferometry could be used with this apparatus, but due to time and equipment availability it was not performed. These types of experiments could be performed in the future.

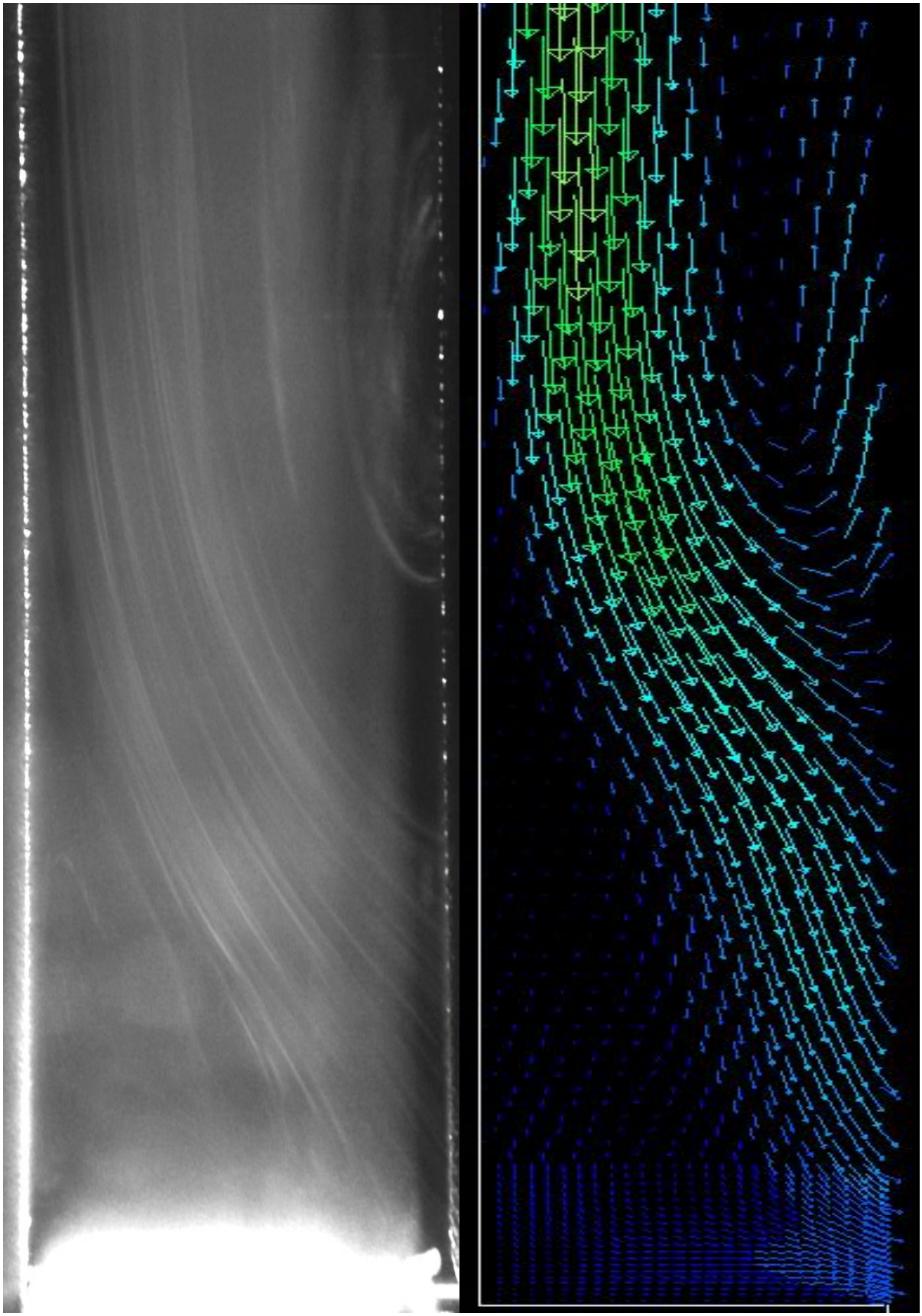

Fig.3.8. *Comparison of velocity profiles for Experimental and CFD results for 15K Temperature Difference*

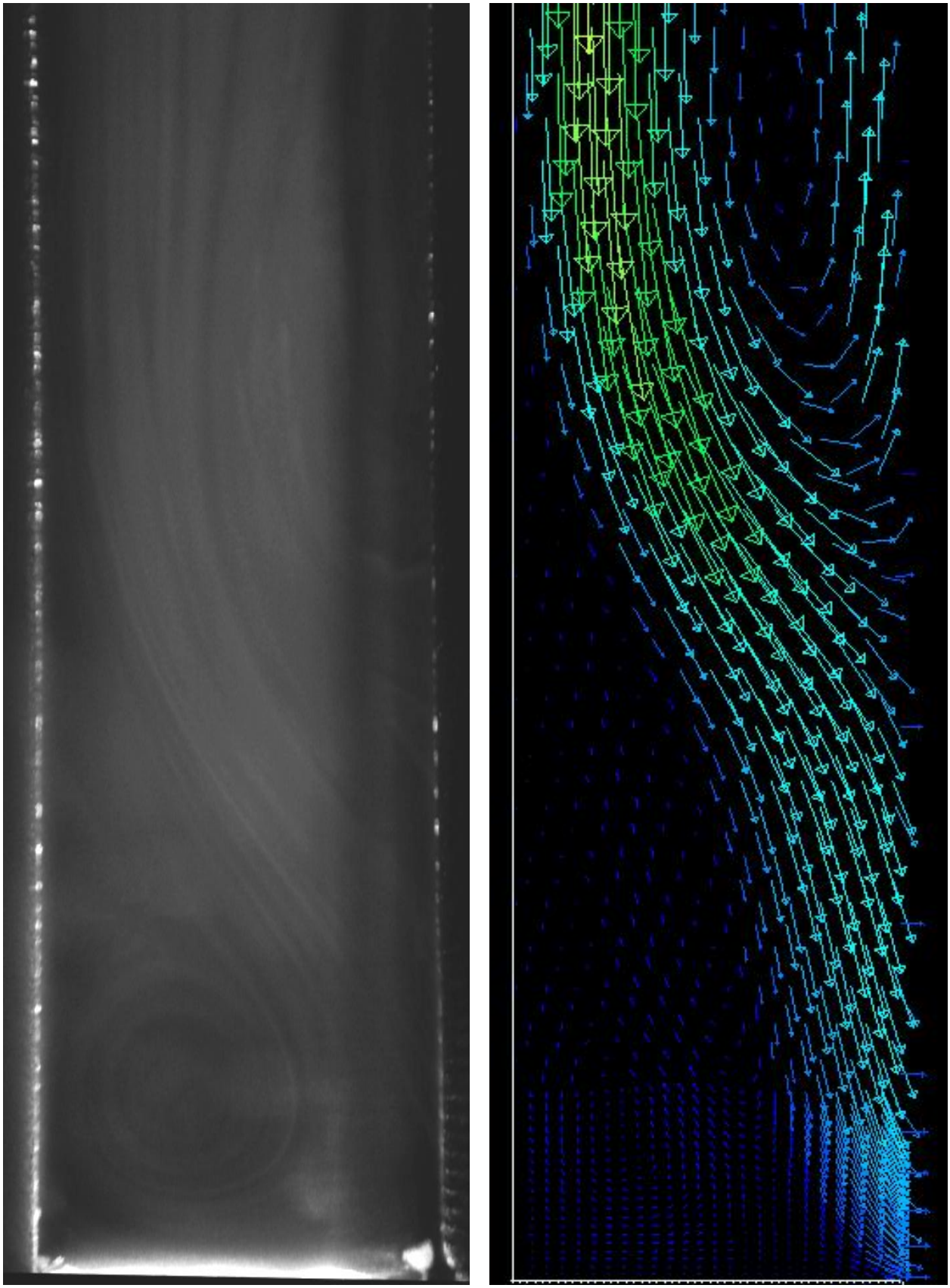

Fig.3.9. *Comparison of velocity profiles for Experimental and CFD results for 26K Temperature Difference*

CHAPTER 4

RESULTS

4.1 INTRODUCTION

The results have been divided into three separate sections; 4.2 Dimensionalized Results; 4.3 Non-Dimensionalized Results and 4.4 Resistor Network Methodology. Each model was run according to the convergence criteria detailed in Section 2.5. Every 1.0 porosity case took around 9000 iterations to reach convergence. Each screen case, using the previous flow fields, took around 1000 additional iterations to reach convergence.

4.2. DIMENSIONALIZED RESULTS

The following results were produced in order to visualize the velocity and thermal flow patterns that are created when a porous insect screen is placed on a window. These models were run under night-time conditions, with no heated screen, where the screen maintains the same local temperature as the flow. All four geometries were used, along with the temperature sets and porosities shown in Tables 2.1 and 2.3. Overall 48 models were run; however, since the Rayleigh numbers are very close between the 6K and -6K temperature difference, the velocity and temperature plots are very similar, so only the -15K and -6K temperature differences are presented. For all these results, the 6K and -6K results are similar; however the main purpose for creating the 6K model is for the effects when a heated screen is added in the Resistor Network analysis in Section 4.4. Similarly for simplicity, only the 1, 0.63 and 0.25 porosity conditions are presented.

As a result of the high aspect ratios, it is hard to visualize the velocity plots in its entirety; therefore the plots are focused on the bottom 0.1m and 0.15m of the cavities for the 0.6096m and

1.22m window heights respectively. This was chosen since the most notable changes in flow patterns are demonstrated in these regions. The insect screen is represented by a black line which is located in the middle of the flow, with its porosity located beneath the diagram.

4.2.1. 0.6096m WINDOW HEIGHT VELOCITY AND TEMPERATURE PLOTS

The first series of figures, Fig.4.1-4.4 show the velocity and temperature plots for the 0.6096m window height and 0.0127m sill length geometry for the two temperature differences of 6K and 15K. There are several notable flow patterns in Fig.4.1. In the no screen case, where porosity is 1, the flow follows smoothly along the wall until it reaches the bottom corner, where it detaches from the wall in order to navigate around it, leaving a small area of essentially dead air. When a screen is added, as in the 0.64 porosity case, the flow inside the window cavity has greatly decreased, but still follows along the wall smoothly until it reaches the bottom. With the pressure drop present, the flow cannot push as easily through the bottom of the cavity as before. Since the spacing between the window and the screen is so small, the flow has little room to manoeuvre. This causes a large decrease in air velocity and forces some of the air to exit the window cavity before it reaches the bottom step, which creates another flow outside the screen in the open air that is unrestricted. Using a finer meshed screen with a porosity of 0.25, the flow speed is decreased even further and there is very little air movement inside the window cavity. The flow is essentially backed up in the window cavity because of the large pressure drop and the majority of the air movement is now located outside of the cavity and screen, in the open air of the room.

In the matching temperature plot shown in Fig.4.2, the driving force behind the flow outside of the window screen can be seen. In the no screen case, the temperature profiles match the velocity profiles quite well. In the bottom corner, where there was an area of dead air in the velocity profile, there is a pocket of cold air. With a screen added in the 0.63 porosity case, the build up of slow moving air causes the cold pocket to increase in size, as well as further cold air penetration throughout the window cavity. On the outside of the screen, the thermal boundary layer increases in size steadily downwards, which is also why the flow on the outside of the

screen increases in magnitude. With a further decrease in porosity, the thermal boundary layer inside the window cavity has become more uniform. At this sill depth, as the porosity decreases the velocity in the cavity decreases and the heat transfer becomes more and more influenced by conduction instead of convection. This indicates that as porosity approaches 0%, conduction begins to dominate and the layers would act as a double pane window.

When the temperature difference is increased to 15K, there is very little noticeable change in the flow structure. In Fig.4.3, the flow velocity has increased, however the flow is very similar to the previous case. This is the same with the temperature plots in Fig.4.4, where the temperature difference has increased, but still retains the same thermal boundary layer shape as in Fig.4.2.

Plots for velocity and temperature for 0.6096m and 0.0254m sill size are shown in Fig.4.5-4.8. When the sill size is increased, it allows more room for the flow to move and recirculation starts to occur. In Fig.4.5, with a temperature difference of 6K, the flow in the no screen condition is the same as in previous cases; however the dead air zone in the bottom corner is larger since the step the flow has to navigate has increased. When the 0.63 porosity screen is used, the velocity profiles in the window cavity are more spread out than in the 0.0127m sill case, and as a result, are slightly lower in velocity overall. At this point, a very small recirculation has appeared, going up along the screen side. The velocity is still very small for this recirculation flow throughout the cavity. With a further decrease in porosity at 0.25, the recirculation is much more noticeable and takes up more space in the cavity, but the flow velocity is still quite small.

The temperature profiles in Fig.4.6 show a small influence due to the recirculation. In the 0.63 porosity profile, the low temperature region at the bottom of the cavity reaches up higher, and the contour lines are more horizontal, indicating that the small recirculation has moved the cold air upwards. For the 0.25 porosity case, because of such low velocities the recirculation does not have as noticeable an effect.

With an increase in the temperature difference to 15K, in Fig.4.7, the recirculation in the 0.0254m sill geometry becomes much more prominent. For a porosity of 0.63, the velocity magnitudes of the downward flow are similar to the 0.0127m sill case; however there is a much larger area of dead air. The flow seems to bypass the corner completely, and the main body of the flow detaches from the window and exits through the screen higher than in other cases. In both the 0.63 and 0.25 porosity profiles, the recirculation is much larger in magnitude. This shows its influence in the temperature profiles.

The profiles for the 15K temperature difference matching the 0.6096m x 0.0254m geometry are shown in Fig.4.8. In the previous 0.63 porosity case, the contours at the bottom of the cavity had a more horizontal shape. Now with the increase in the temperature difference and recirculation, a U shape in the contours can be seen near the bottom of the cavity, as the cold air is brought down the window, and then back up along the screen. With the 0.25 case, since the flow velocity is higher, the contours take on a more horizontal shape in the cavity unlike the 6K temperature difference case.

4.2.2 1.22m WINDOW HEIGHT VELOCITY AND TEMPERATURE PLOTS

The velocity and temperature plots for the 1.22m height, 0.0127m sill length geometry are shown in Fig.4.9-4.12. For all these cases, the velocity is higher at the bottom of the cavity than the 0.6096m cases, since the window height has increased which allowed the flow to be in contact with the constant temperature wall boundary for twice as long. Comparing Fig.4.1 and Fig.4.9 for the -6K temperature difference, and Fig.4.3 and 4.11 for the -15K temperature difference, other than an increase in flow velocity, the flow structures are very similar with no significant changes. Similarly, the -6K temperature profiles in Fig.4.2 and Fig.4.10 and -15K profiles in Fig.4.4 and Fig.4.12 show no major differences, only the 1.22m height cases having its profiles stretched out more with the height of the window.

When the sill length is increased to 0.0254m, the velocity plots in Fig.4.13 shows some changes from the 0.6096m velocity plots in Fig.4.5. In the 0.63 porosity case, there no longer appears to be any recirculation in the lower half of the cavity. It is only in the upper regions where there is a very slight recirculation. This may be due to the fact that in the 0.6096m case, the velocity boundary layer only reaches ¾ of the way through the window cavity and does not touch the screen by the time it approaches the bottom corner. This allows the recirculation to develop through the still air that is close to the screen. In the 1.22m height case, the developing region is longer, so by the time the flow reaches the bottom corner, the velocity boundary layer has developed large enough to reach the screen, and thus there is no room for the recirculation to develop. For the 0.25 porosity case, the recirculation is still present, though it is extremely small in magnitude compared to the main flow, unlike the 0.6096m height case where the recirculation flow was much more comparable. This may be due again to the fact that the velocity boundary layer is larger than in the previous geometries.

For the temperature profiles in Fig.4.14, there is not much difference. Since the temperature difference is not that large, the velocity magnitudes are small and the effects of the recirculation on temperature is minimal, so while there is differences in the velocity profiles between the 0.6096m cases and the 1.22m cases, the differences in temperature profiles is very small.

When the temperature difference is increased to -15K, the recirculation starts to reappear at the bottom part of the cavity as can be seen in Fig.4.15. In the 1.0 porosity case, the flow is strong enough at the bottom of the cavity that there is now a small recirculation in the bottom corner that was not present in previous cases. The flow structure in the 0.63 case is similar to the same in Fig.4.7 for the 0.6096m height; however the recirculation is smaller, it does not begin to develop until much higher up and it takes up much less width of the cavity. This may also be caused by the more developed velocity boundary layer as in the previous case, but because the flow velocities are higher, the recirculation is allowed to develop.

Finally, as before there are no major differences between the temperature profiles for the 0.6096m height, -15K temperature difference in Fig.4.8 and the 1.22m height in Fig.4.16 except for the 1.0 porosity case, where the low temperature pocket that was previously present is now much smaller because of the recirculation.

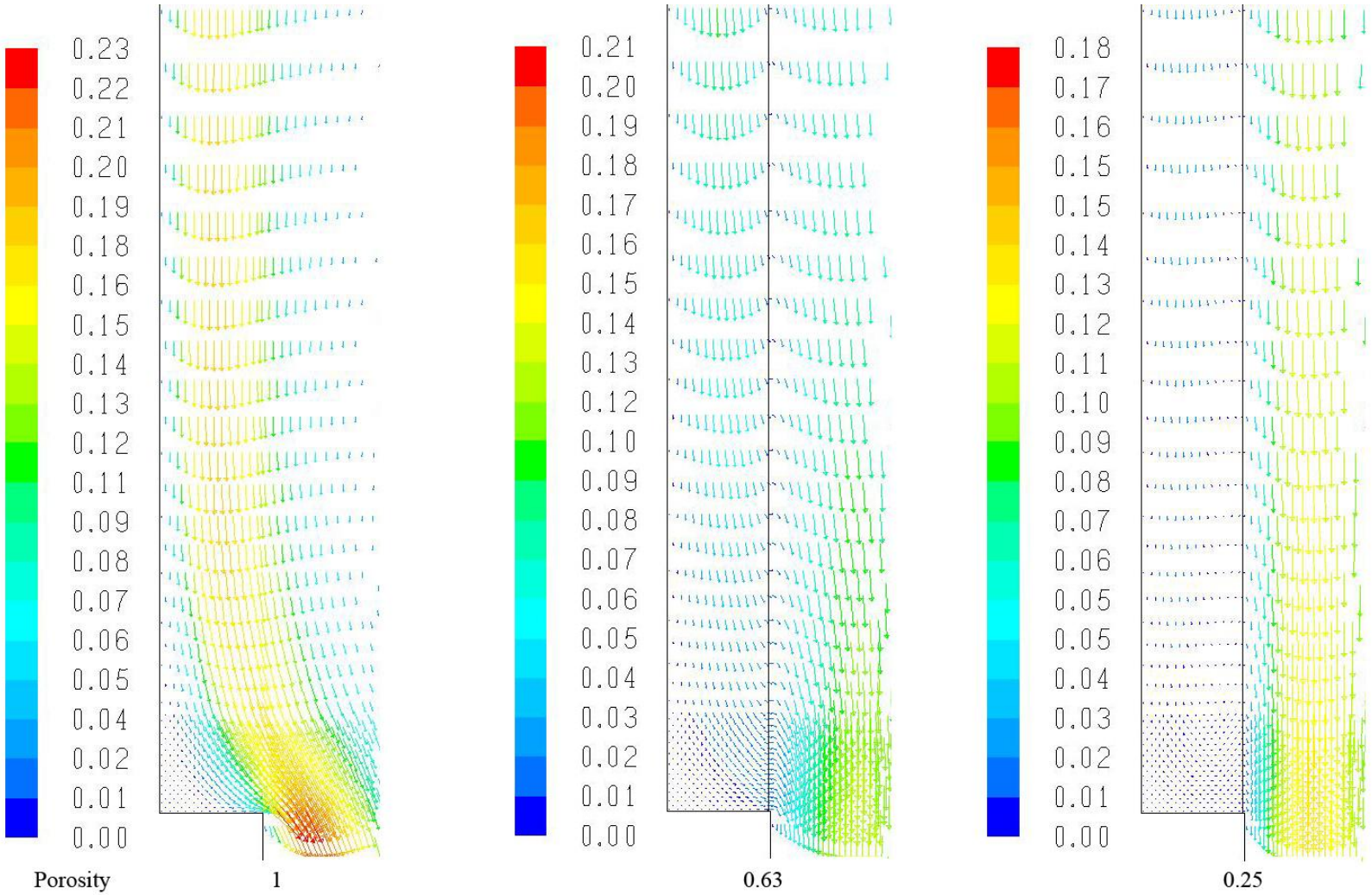

Fig.4.1. *Velocity Plots in m/s for 0.6096m height, 0.0127m sill window with T_g = 290, γ = 1.0, 0.63, 0.25*

Fig.4.2. *Temperature Plots in K for 0.6096m height, 0.0127m sill window with T_g = 290, γ = 1.0,* 0.63, 0.25

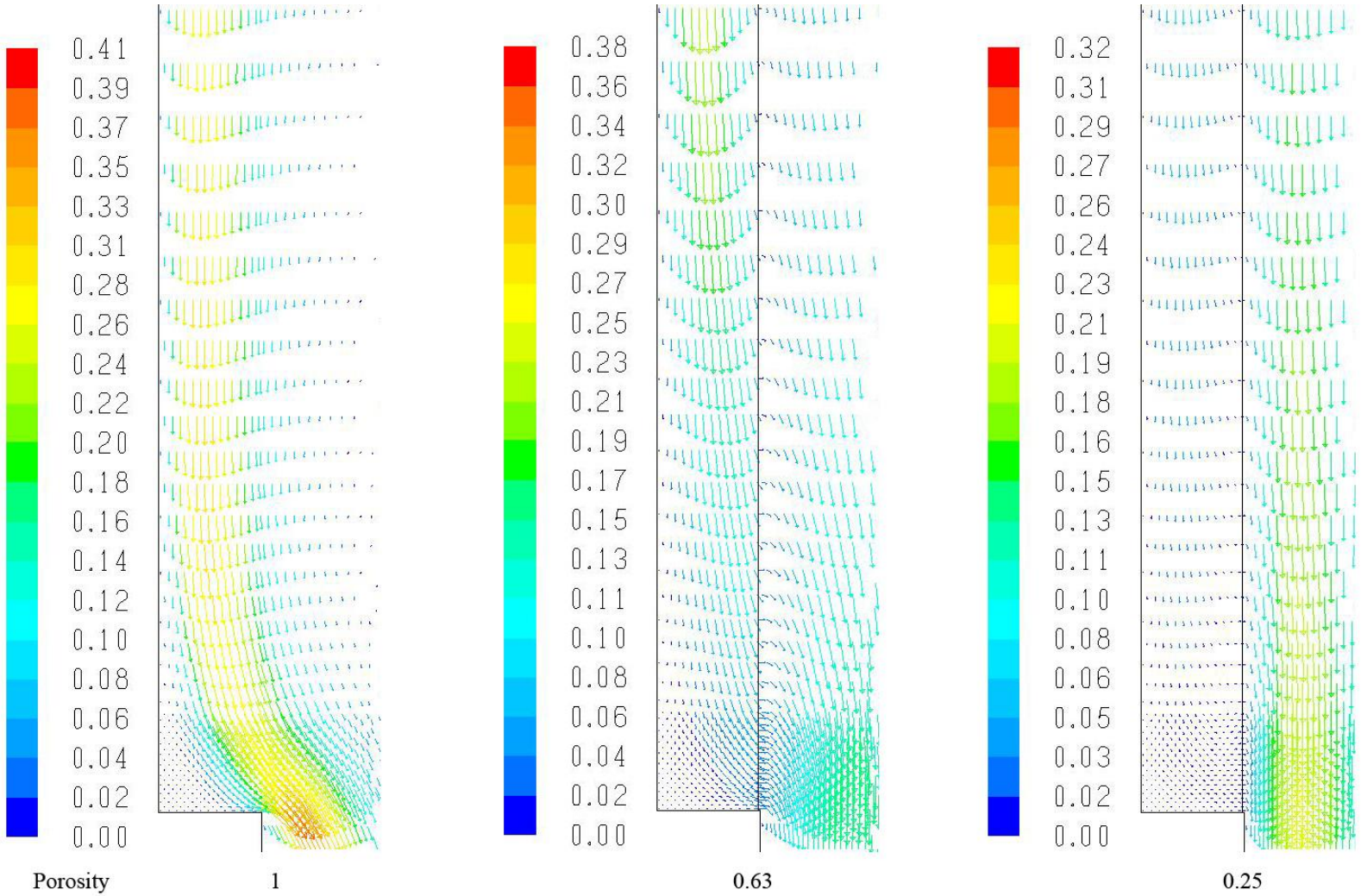

Fig.4.3. *Velocity Plots in m/s for 0.6096m height, 0.0127m sill window with* T_g *= 281,* γ *= 1.0, 0.63, 0.25*

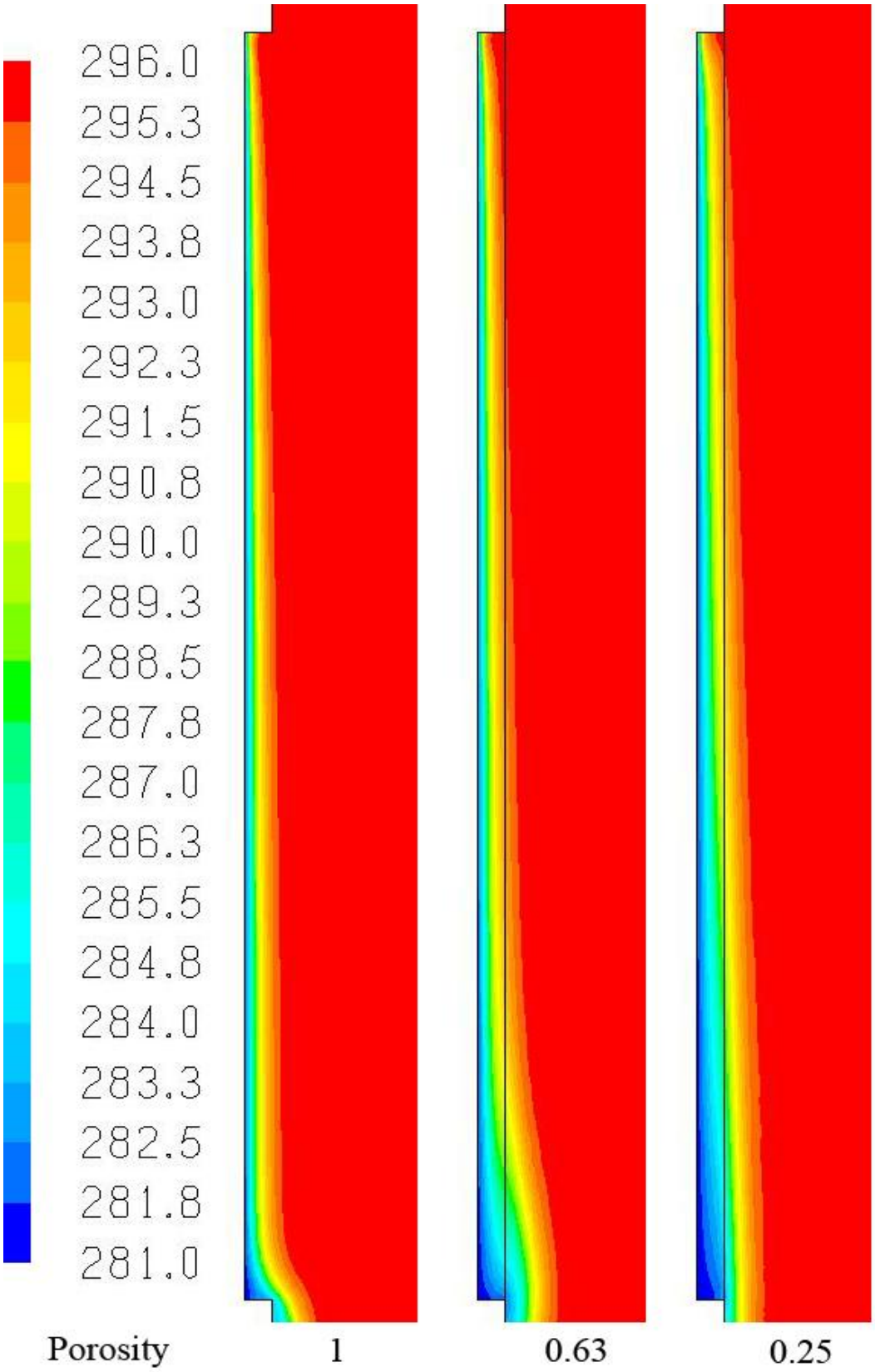

Fig.4.4. *Temperature Plots in K for 0.6096m height, 0.0127m sill window with T_g = 281, γ = 1.0, 0.63, 0.25*

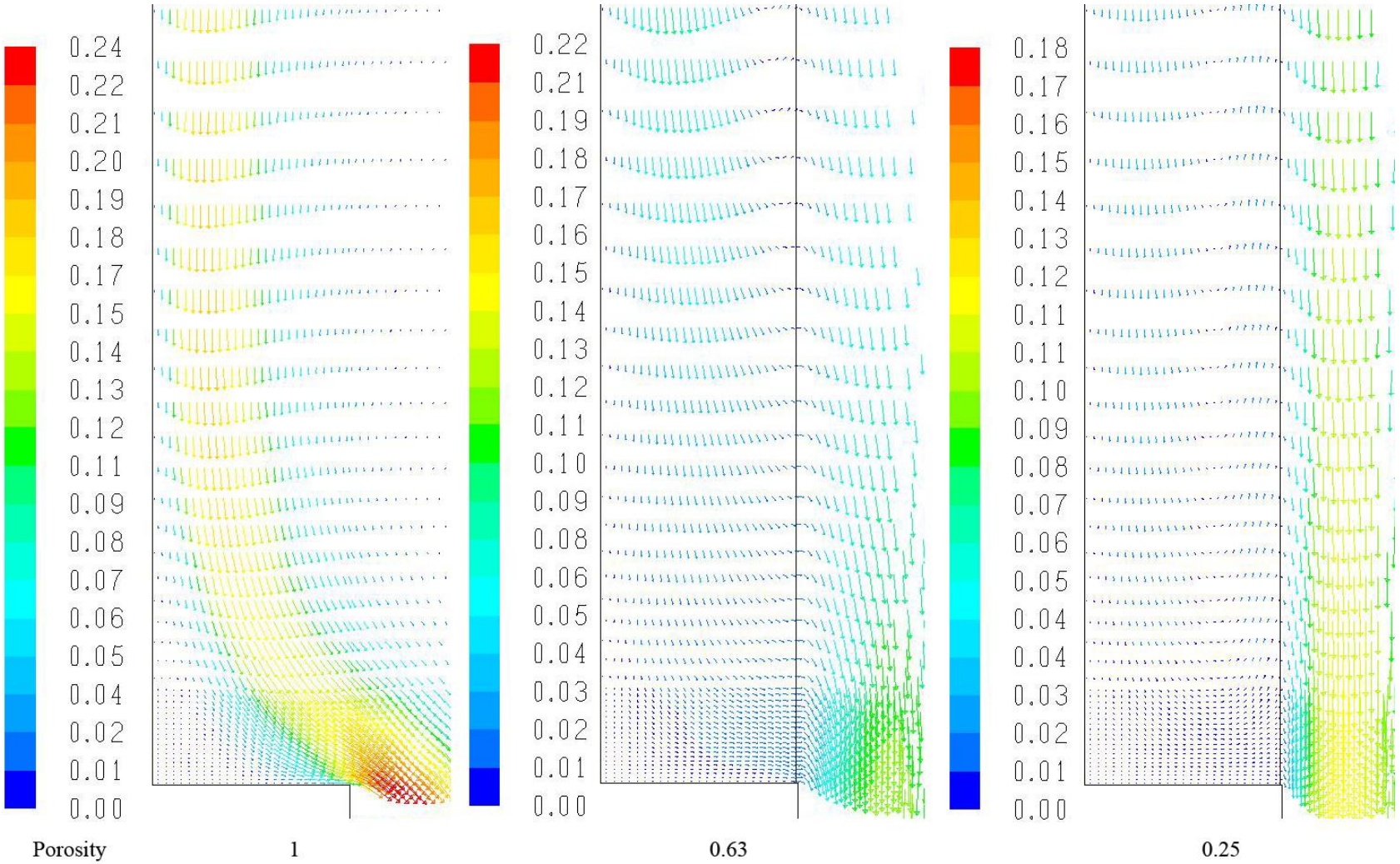

Fig.4.5. *Velocity Plots in m/s for 0.6096m height, 0.0254m sill window with T_g = 290, γ = 1.0, 0.63, 0.25*

Fig.4.6. *Temperature Plots in K for 0.6096m height, 0.0254m sill window with T_g = 290, γ = 1.0,* 0.63, 0.25

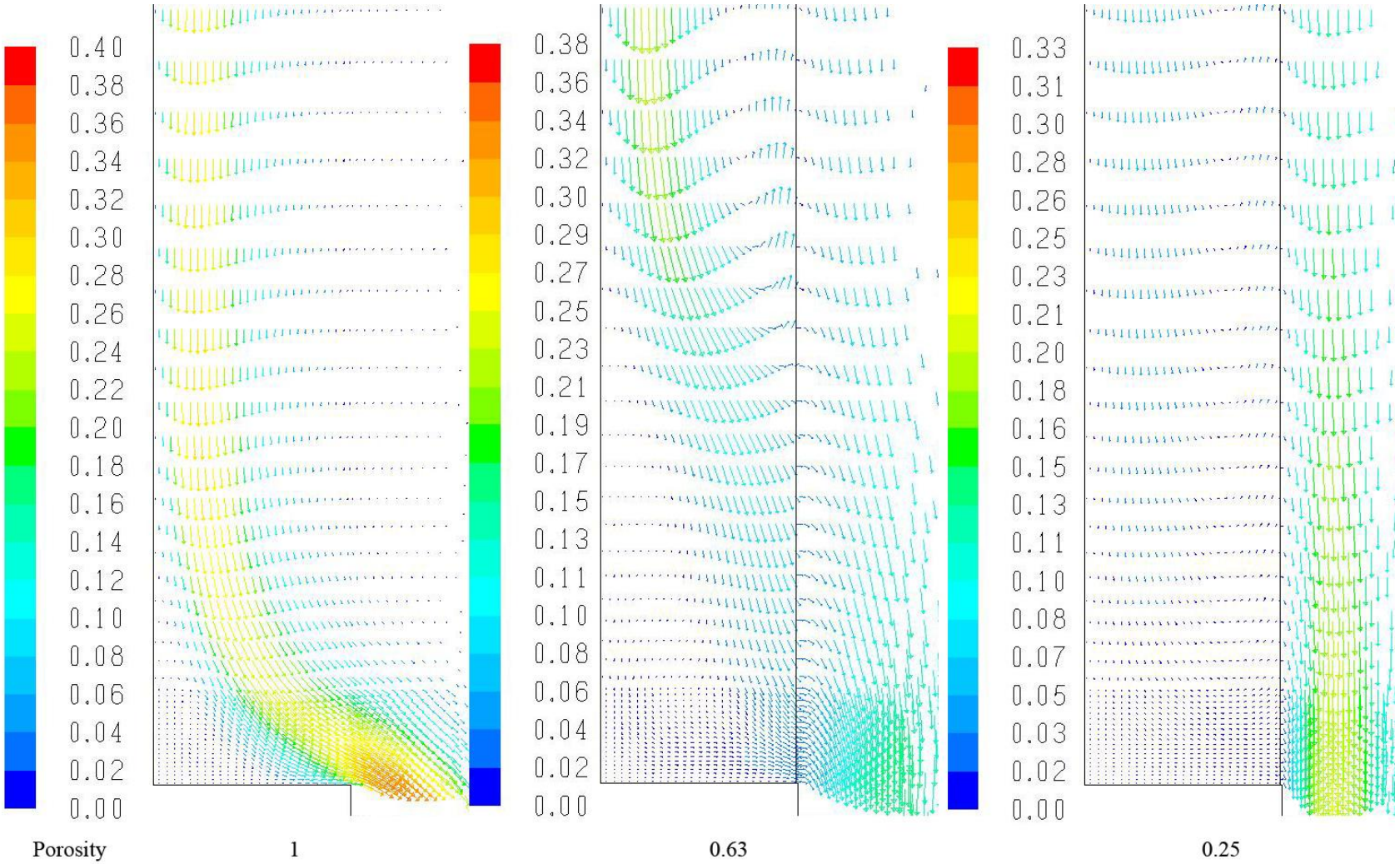

Fig.4.7. *Velocity Plots in m/s for 0.6096m height, 0.0254m sill window with T_g = 281, γ = 1.0, 0.63, 0.25*

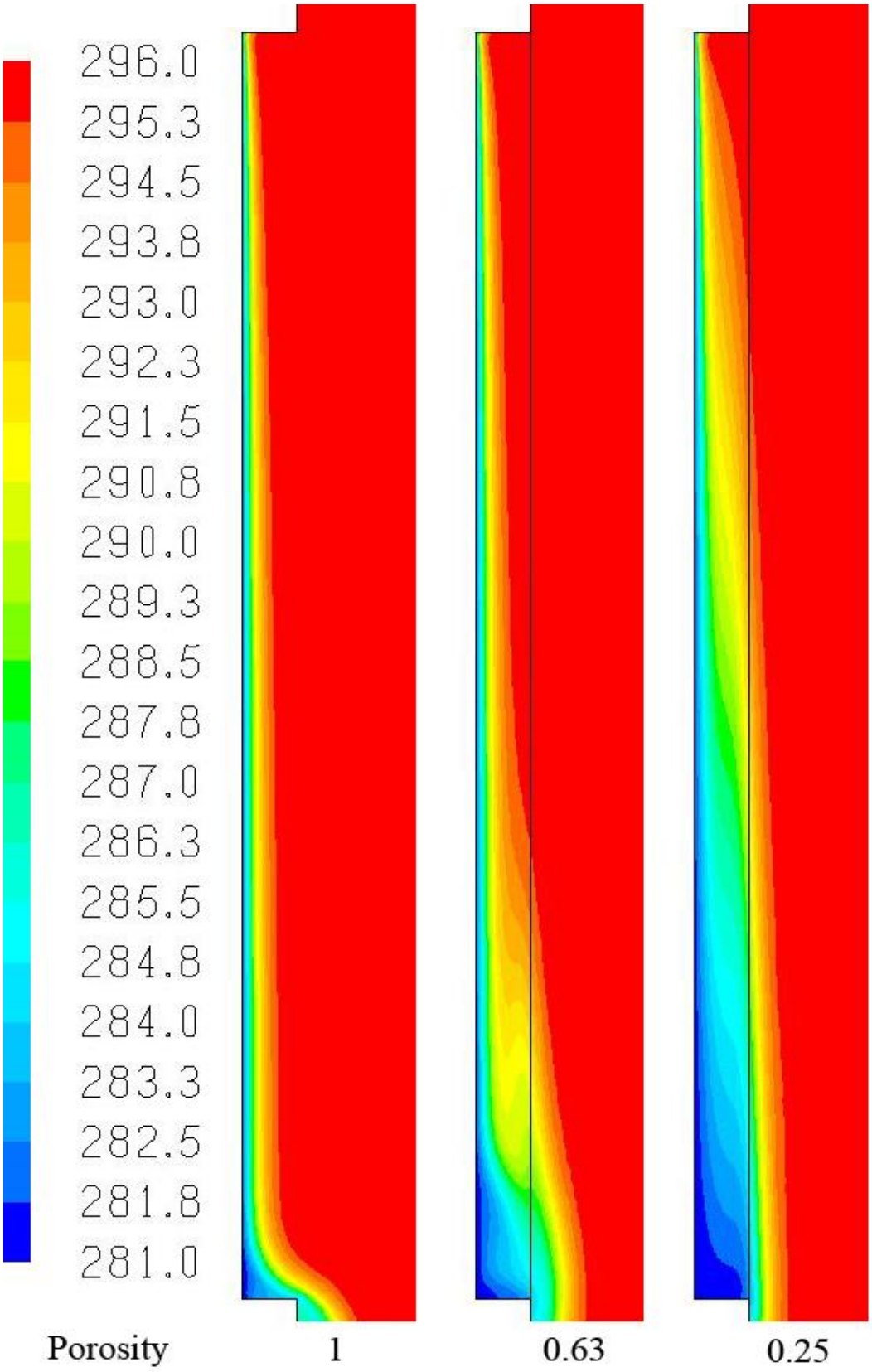

Fig.4.8. *Temperature Plots in K for 0.6096m height, 0.0254m sill window with T_g = 281, γ = 1.0, 0.63, 0.25*

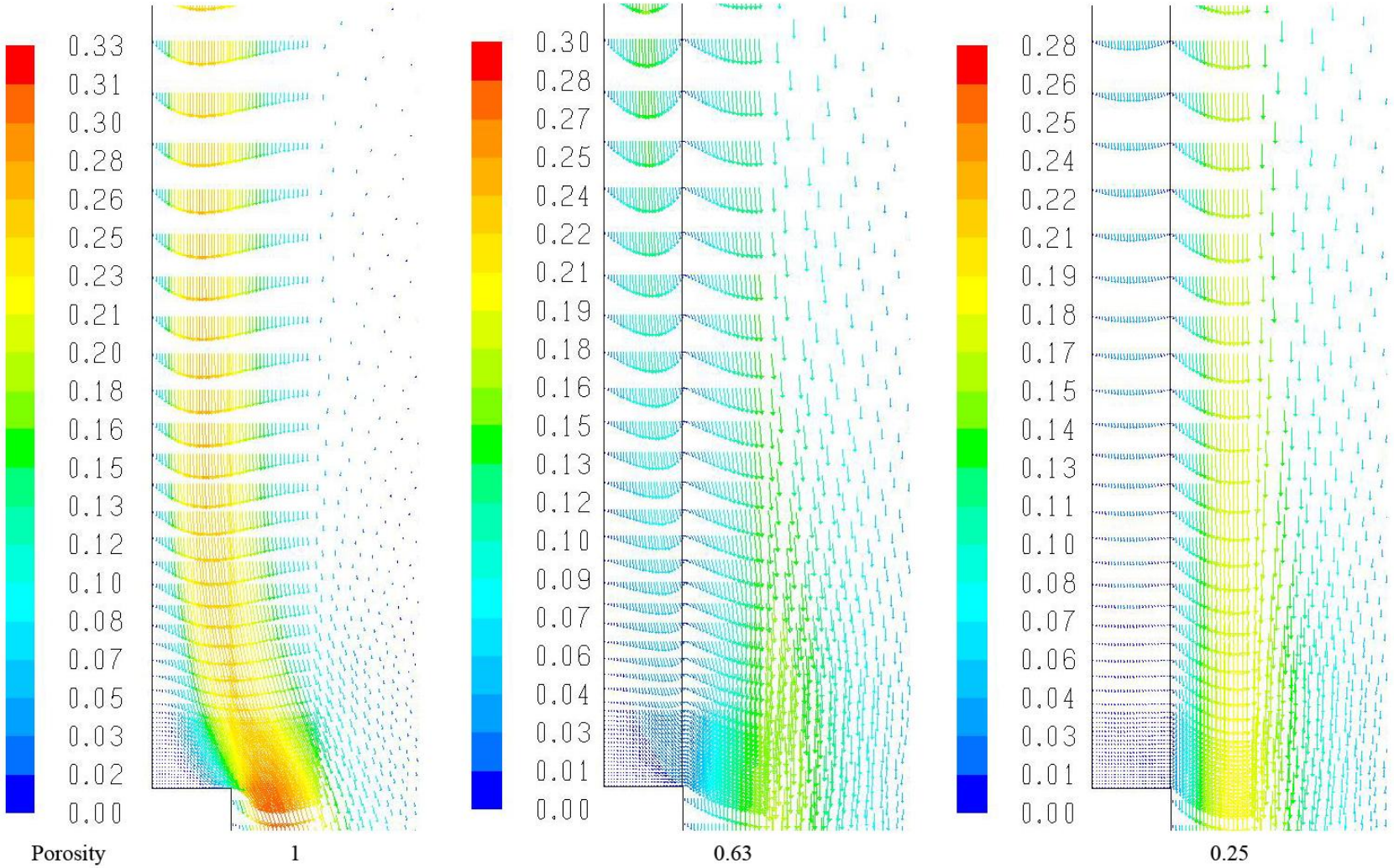

Fig.4.9. *Velocity Plots in m/s for 1.22m height, 0.0127m sill window with T_g = 290, γ = 1.0, 0.63, 0.25*

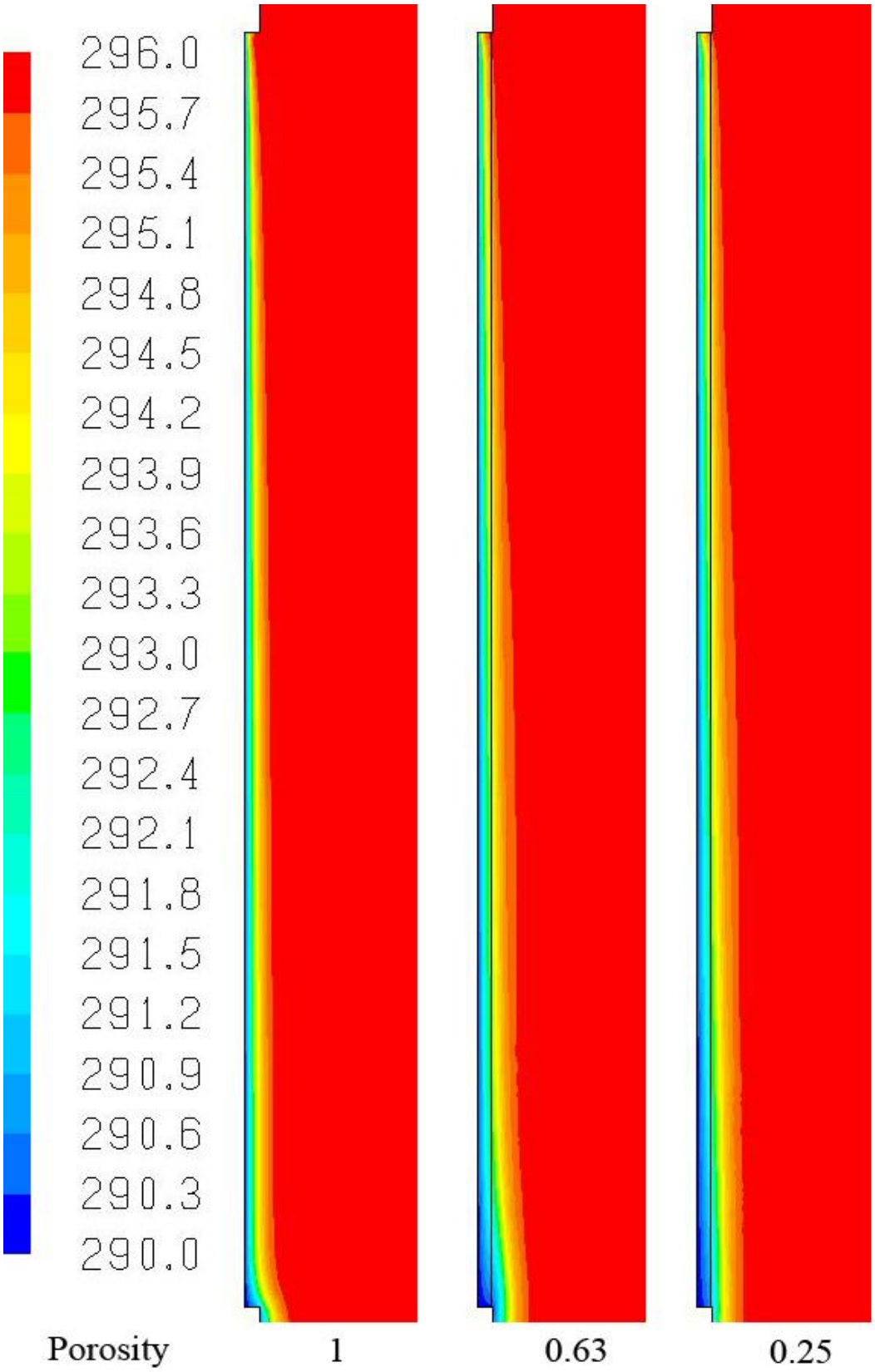

Fig.4.10. *Temperature Plots in K for 1.22m height, 0.0127m sill window with T_g = 290, γ = 1.0, 0.63, 0.25*

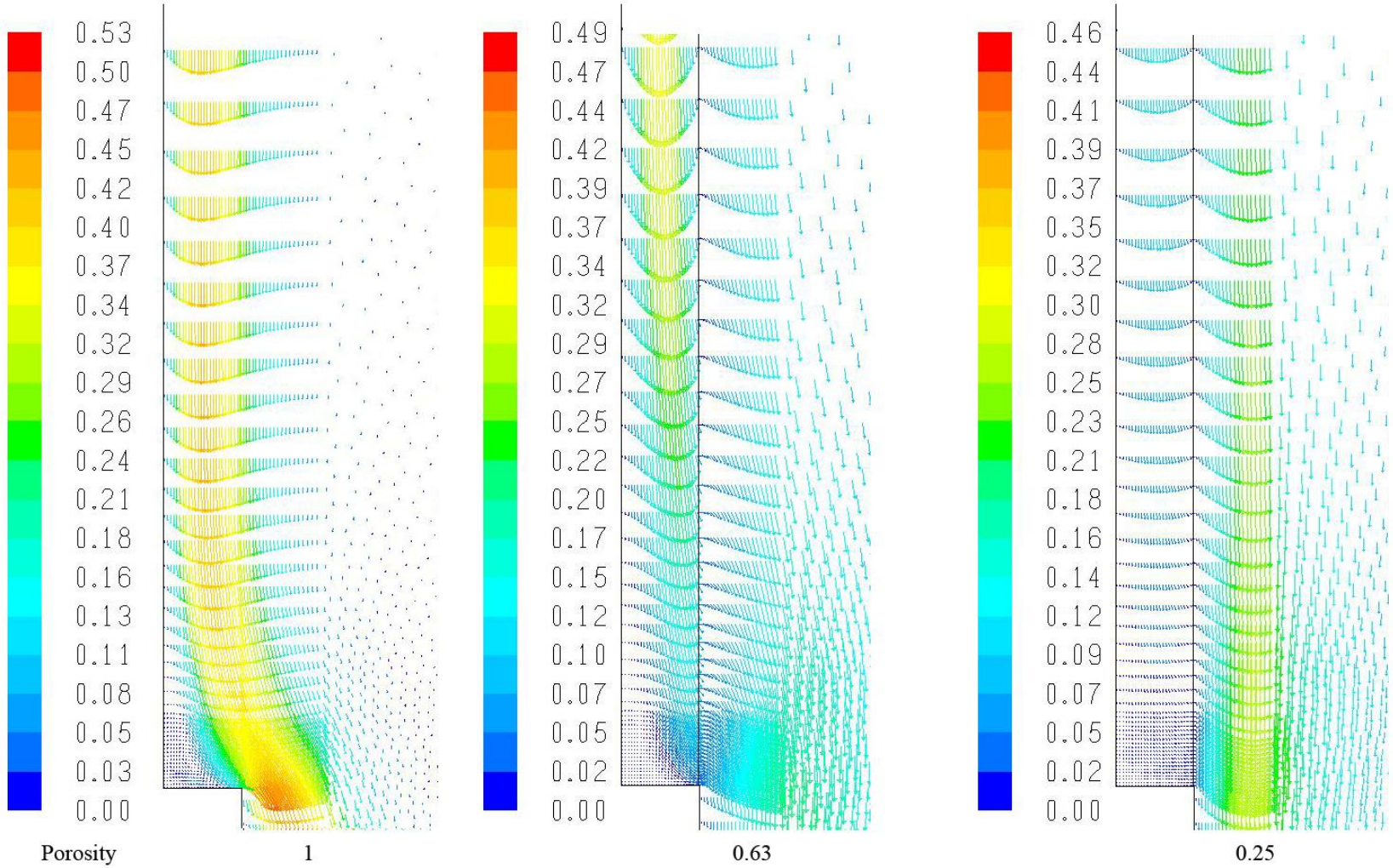

Fig.4.11. *Velocity Plots in m/s for 1.22m height, 0.0127m sill window with T_g = 281, γ = 1.0, 0.63, 0.25*

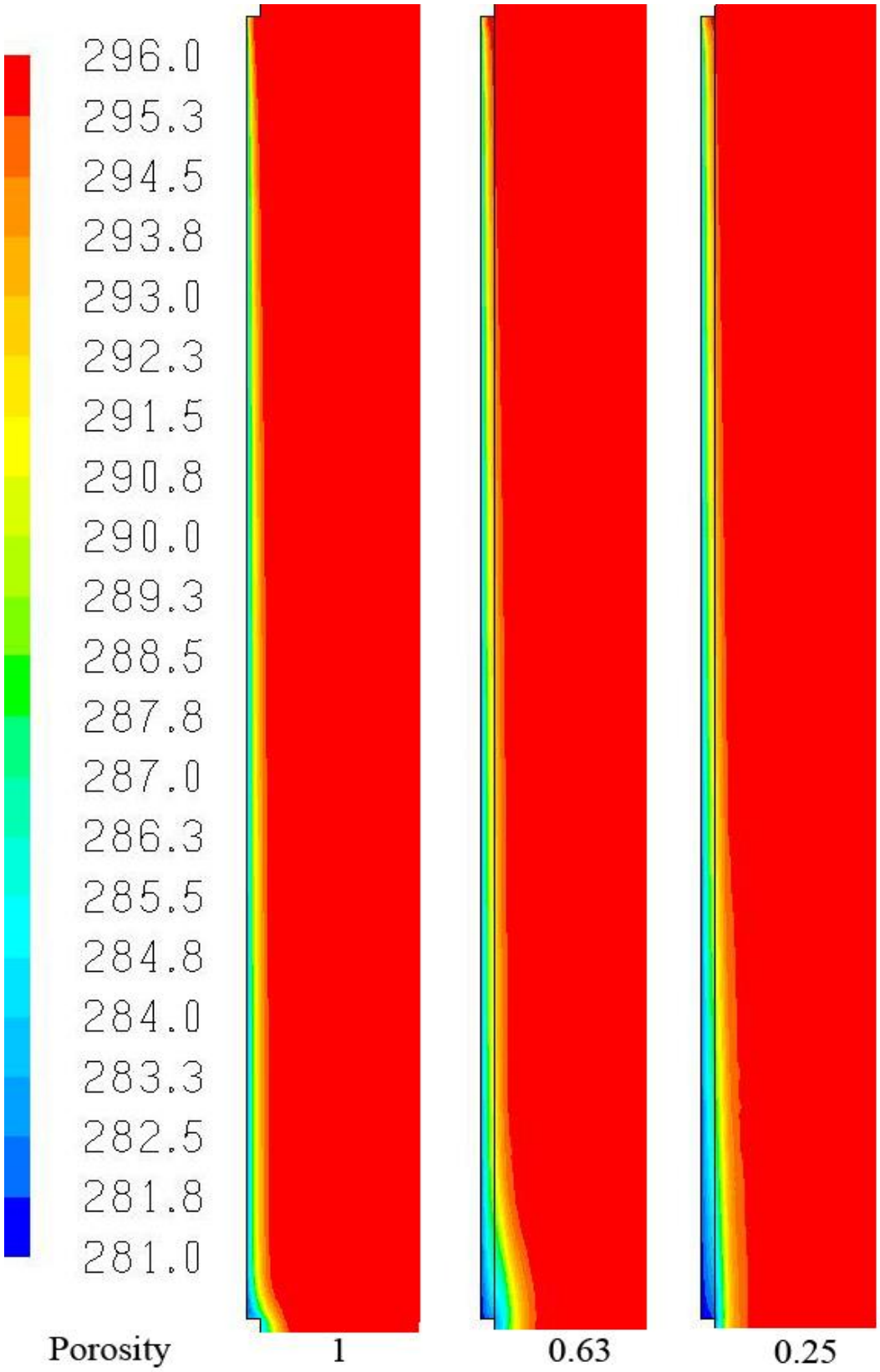

Fig.4.12. *Temperature Plots in K for 1.22m height, 0.0127m sill window with T_g = 281, γ = 1.0, 0.63, 0.25*

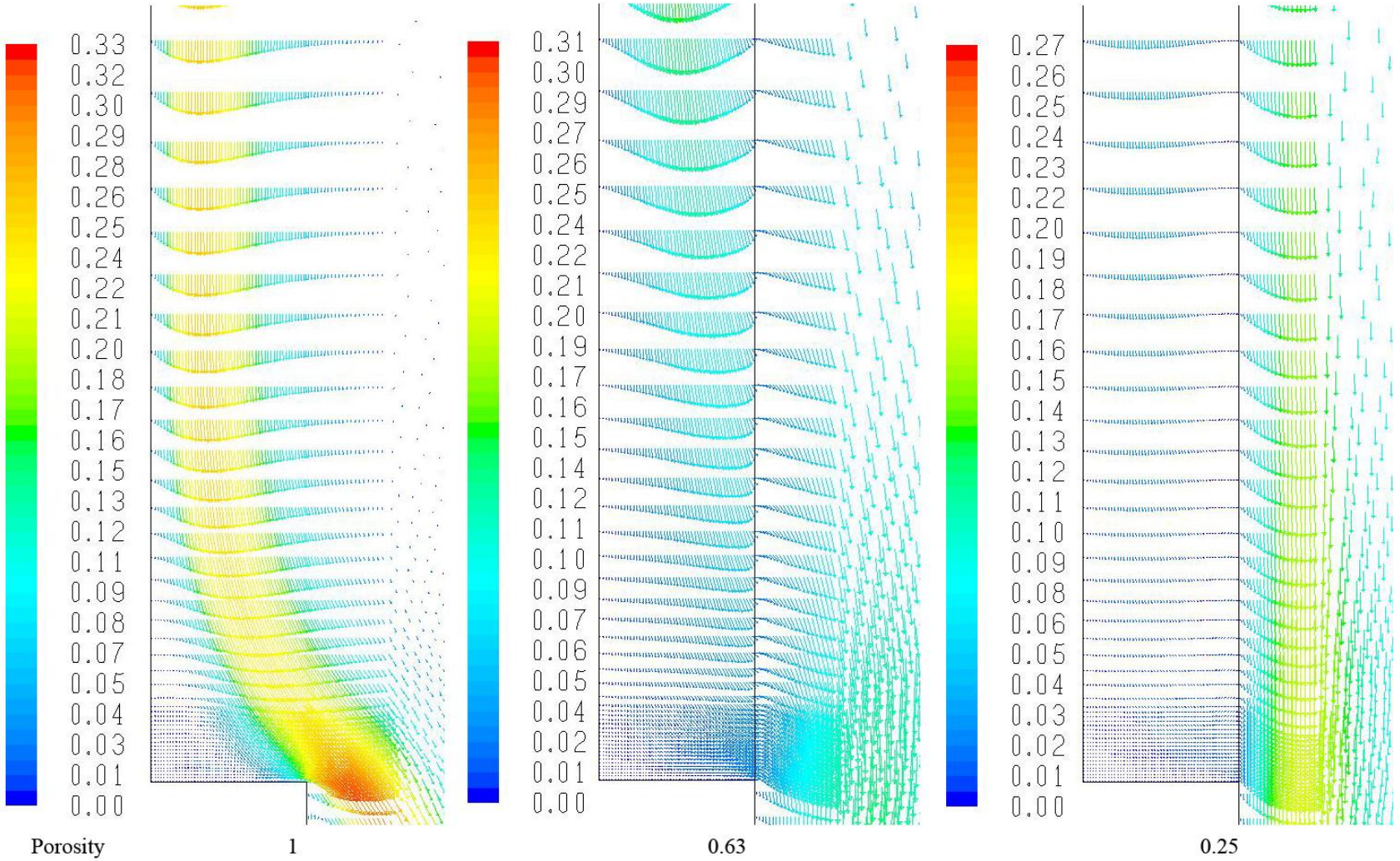

Fig.4.13. *Velocity Plots in m/s for 1.22m height, 0.0254m sill window with T_g = 290, γ = 1.0, 0.63, 0.25*

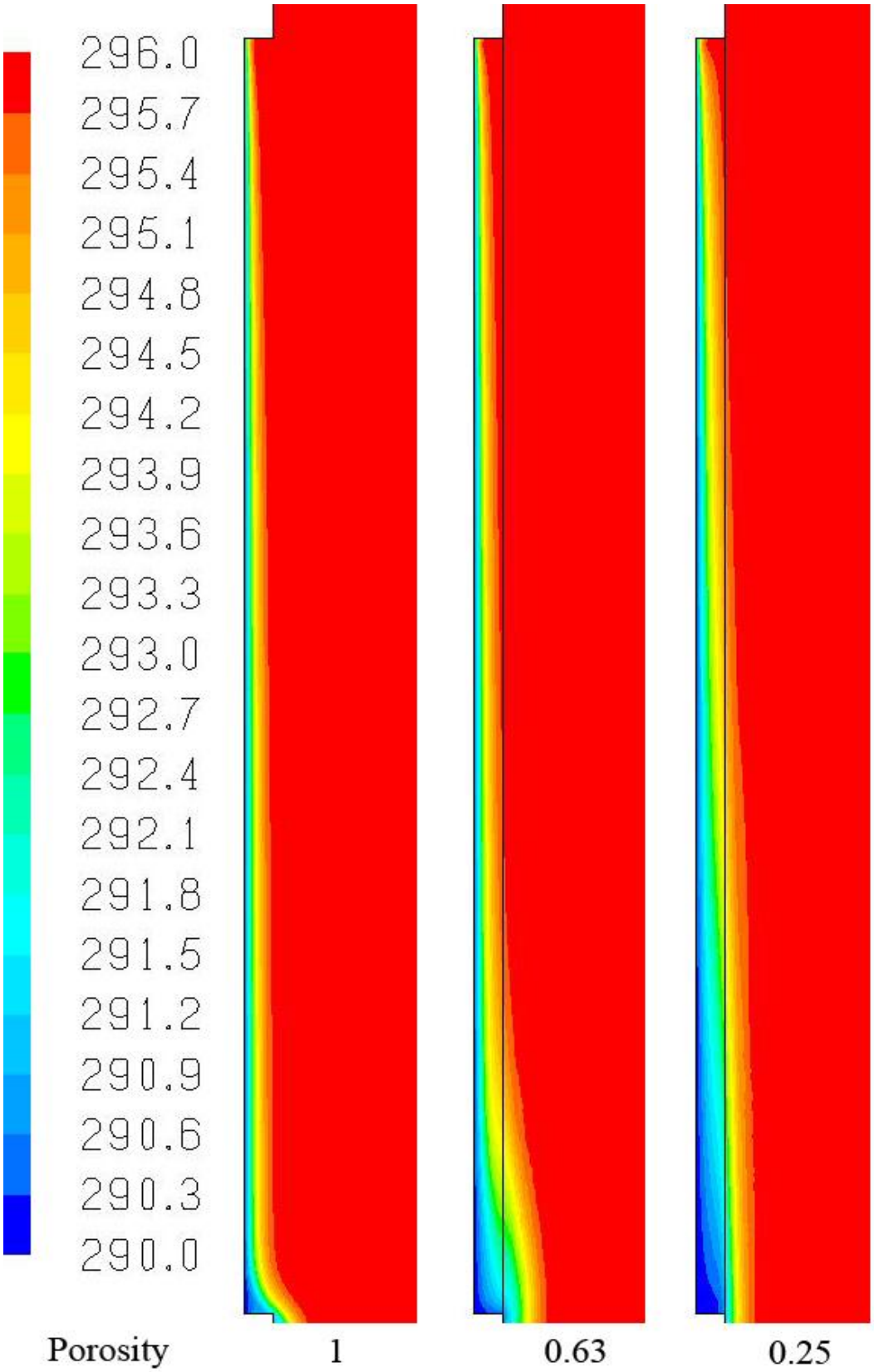

Fig.4.14. *Temperature Plots in K for 1.22m height, 0.0254m sill window with T_g = 290, γ = 1.0, 0.63, 0.25*

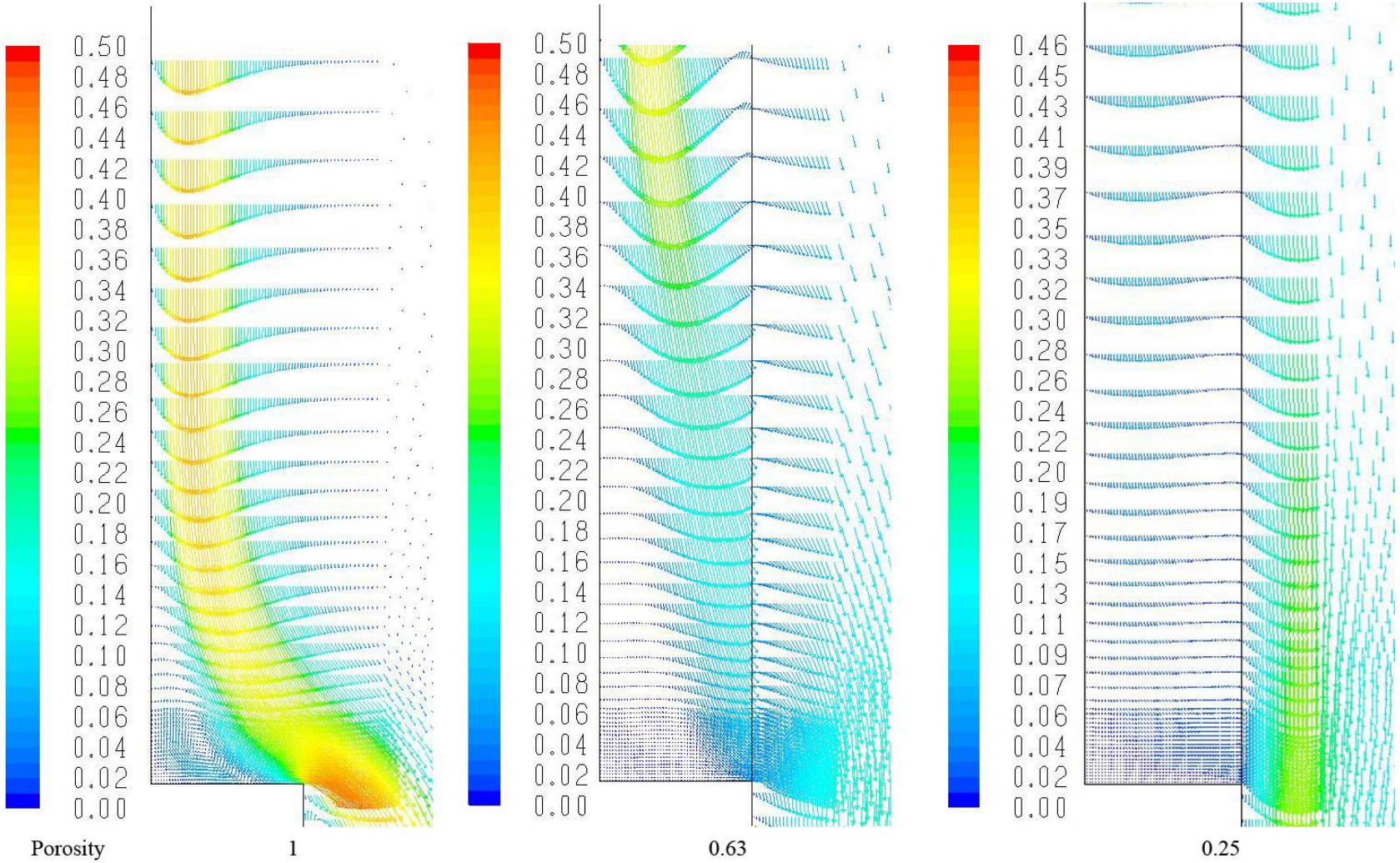

Fig.4.15. *Velocity Plots in m/s for 1.22m height, 0.0254m sill window with* $T_g = 281$, $\gamma = 1.0, 0.63, 0.25$

Fig.4.16. *Temperature Plots in K for 1.22m height, 0.0254m sill window with T_g = 281, γ =1.0, 0.63, 0.25*

4.3 NON-DIMENSIONALIZED RESULTS

For these results, the local heat transfer coefficient along the window was taken from the FLUENT model for each case. Using the length of the window as the base, the Nusselt and Rayleigh numbers were calculated using the equations in Section 2.6.

4.3.1 RESULTS BY TEMPERATURE DIFFERENCE

The following Figures 4.17-4.20 of Nu_L vs Ra_L are arranged for the varying porosities. In each figure there are two plots showing the results for the two window heights. Fig.4.17-4.18 show results for -6K and -15K temperature differences for the 0.0125m sill depth and similarly Fig.4.19-4.20 are for the 0.0254m sill depth. In all of these figures, it can be seen that with decreasing porosity, the heat transfer decreases overall and becomes more uniform across the centre of the cavity. For each case, with the higher porosities, there are end effects that can be seen and the flow tries to navigate the step at the bottom of the cavity. This translates to large drop in Nusselt number, or in some cases a sudden increase and the bottom of each plot. With decreasing screen porosity, there are less of these end effects, which is expected since as the porosity gets smaller, there is less flow that can pass through the screen. From the previous non-dimensionalized results in Section 4.2, when the porosity is decreased towards 0, the cavity begins to act like an enclosure, and the flow becomes more confined within the cavity. This allows fewer dead air zones or small pockets of recirculation to be created which cause these jumps in heat transfer. In all cases, the 0.90, 0.63 and 0.50 porosity cases all produce very similar plots, even at larger temperature differences. In Miguel [1998 b], the pressure drop for high porosities did not begin to significantly increase until after a porosity of 0.36. Looking at the pressure drop properties, calculated from the results in Miguel [1998 b], in Table 2.2, the loss coefficients are fairly close for the higher porosities but much larger for 0.25, so it follows that the heat transfer for these porosities would also not greatly change. When the Rayleigh number is by increasing the temperature difference, for all cases the Nu_L increases as well for all porosities and amplifies the end effects. These are all the general similarities between each of the plots; however there are also many items to note for the specific geometries and temperature differences.

In the 0.0125m sill depth and -6K temperature difference case, seen in Fig.4.17, for the two window heights, there is not much difference between plots a) and b), only that the larger window height plot in b) is stretched out because of the larger amount of energy in the system. This similarity follows from the previous section since there were no significant changes in flow structure between these geometries in the temperature and velocity plots for the -6K temperature difference.

With an increase in the temperature difference to -15K, shown in Fig.4.18, there are a few changes between the two window heights. In a), for the 1.0 porosity case, the Nusselt number drops at a Ra_L of about 3.00e+08, however at an Ra_L of about 3.75e+08, the Nusselt number stops decreasing and for a short distance it is steady. While not well seen in the velocity plot shown in Fig.4.3, most likely lost in the larger velocity magnitudes present, this indicates that there is a either very small recirculation in the bottom corner, or more likely since the velocities are so low in this region that there is conduction dominating, causing the constant heat transfer rate. With the window height increased in b), the recirculation area in much larger and its effects on the heat transfer can be more easily seen. In the 1.0 and now the 0.90 case, an "S" shape is created as the recirculation jumps the heat transfer up slightly and then back down as the window meets the bottom of the cavity at the sill.

When the sill length is doubled with a temperature difference of -6K, there are some changes in the heat transfer in Fig.4.19. In plot a) for the smaller window height, it can be seen there is the slight recirculation starting to occur in the 1.0 porosity case, and decreasing in effect with porosity. The 1.0 case shows a steadying of heat transfer at the very bottom. Similarly in plot b) the same effects can be seen, but amplified. The 1.0 porosity case for this height shows a slight increase in the heat transfer at the bottom, instead of approaching constant due to a greater amount of recirculation, however it is very slight. When compared to the previous 0.0125m sill depth case in Fig.4.17, these curves are much less parabolic, due to the influence of the smaller recirculation zones which begin to create the "S" shape.

This is even more noticeable when the temperature difference for the 0.0254m sill depth is increased to -15K in Fig.4.20. Comparing plot a) of Fig.4.20 to the velocity profiles in Fig.4.7 it can be seen that the higher porosities have a very slow moving air region in the bottom corners

where there is slight recirculation but where conduction could also play a role, which creates the constant heat transfer area in the lower section of plot a). Conduction is also likely when taking a closer look at the temperature plot in Fig.4.8, since in the bottom corner the temperature contours are essentially vertical. With the larger window height in plot b) of Fig.4.20, the 1.0 and 0.90 porosity cases have a much larger recirculation, causing the heat transfer to jump, thus creating the "S" shape once again.

4.3.2 NON-DIMENSIONALIZED RESULTS BY POROSITY

The following Figures 4.21-4.26 the same data as previous, but it has been rearranged to show the effects of temperature difference on the heat transfer, separated by porosity. In each plot, the solid markers are for the 1.22m window height and the outlined markers are for 0.6096m window height. In all the plots, the smaller window height follows the same heat transfer rate as the larger window height for each temperature difference, until the flow reaches the bottom of the cavity where the end effects appear.

The first three figures, Fig.4.21-4.23 are for a sill length of 0.0125m. For the no screen case in Fig.4.21, it can be seen that for all temperature differences, there is a small amount of recirculation which gets stronger as the Rayleigh number increases. With a 0.63 porosity screen, in Fig.4.22, with the screen so close to the flow, the end effects immediately disappear. The similar temperature difference cases (but different heights) all line up together, however the different temperature differences start to deviate from each other slightly. This shape also occurs in the 0.90 and 0.50 porosity cases. A possible cause for this is since the screen is so close to the flow, increasing the Rayleigh number by increasing the temperature difference affects the flow much higher in the cavity and causes these changes in the heat transfer. In Fig.4.23 when the porosity is decreased to 0.25, this slight deviation disappears.

In Fig.4.24-4.26, the sill length is increased to 0.0245m. In Fig.4.24, we again see recirculation zones in the bottom corner as the flow navigates the step. With an added screen of porosity 0.63, shown in Fig.4.25, the effect of the recirculation zone has greatly decreased, however for the -15K temperature difference; there is still the presence of the "S" curve in the heat transfer. This larger sill size does not immediately quell these recirculation zones since the flow still has room to manoeuvre around in the cavity. With the smaller porosity of 0.25 in Fig.4.26, the end effects have disappeared and the heat transfer rates have taken on a more parabolic shape.

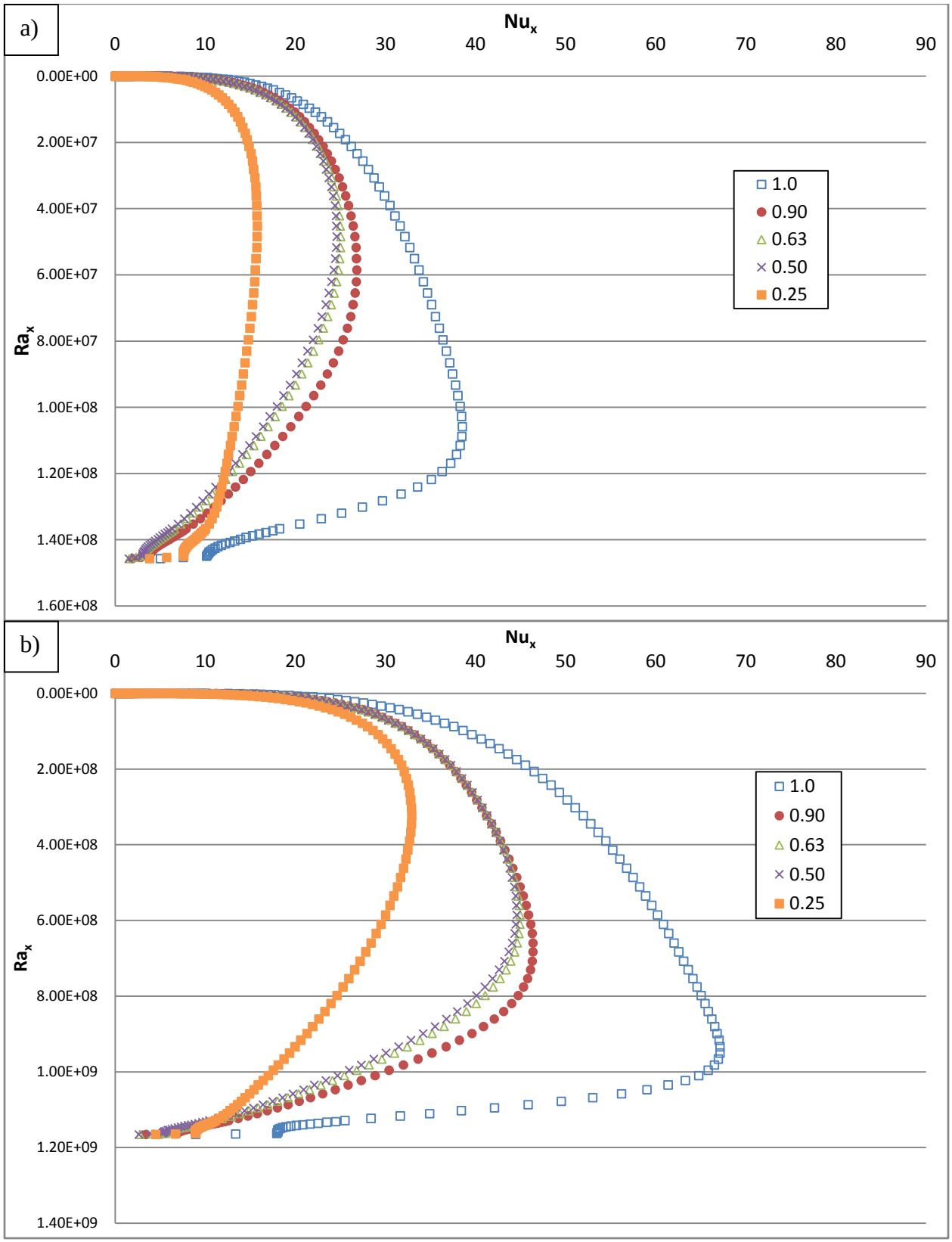

Fig.4.17. *Nusselt vs Rayleigh for -6K Temperature Difference for a) 0.6096m Height and b)1.22m Height and 0.0125m Sill depth as a function of porosity*

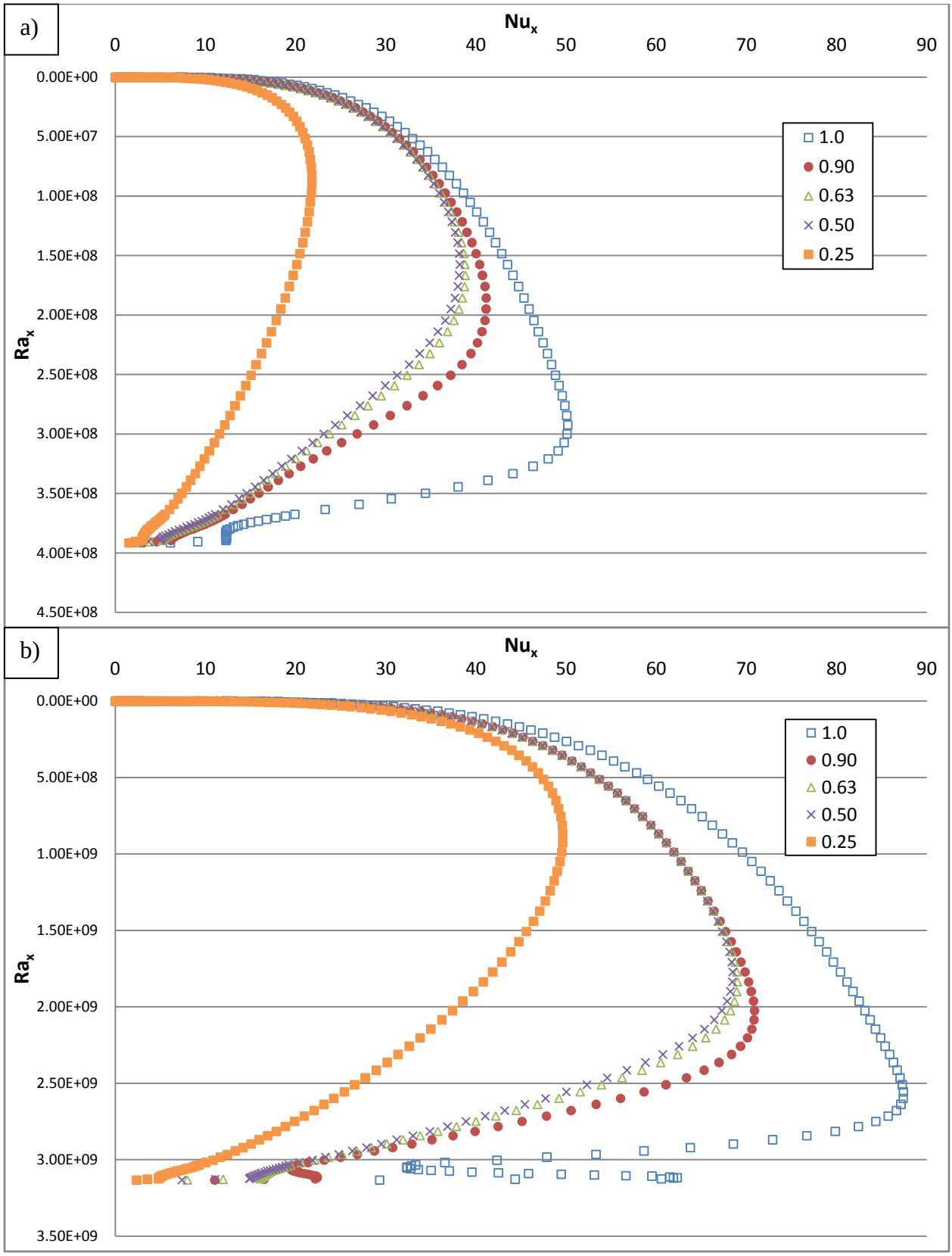

Fig.4.18. Nusselt vs Rayleigh for -16K Temperature Difference for a) 0.6096m Height and b)1.22m Height and 0.0125m Sill depth as a function of porosity

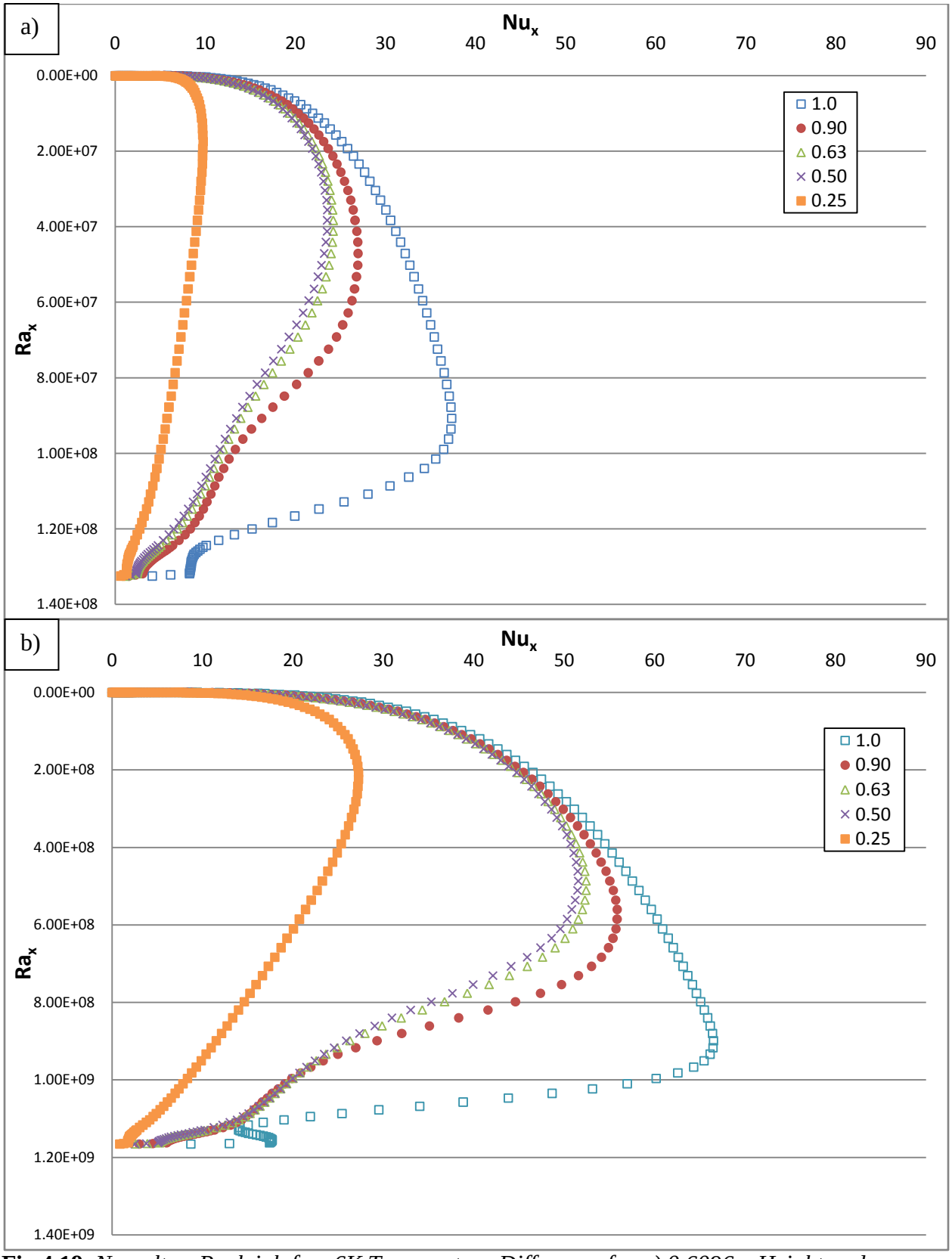

Fig.4.19. *Nusselt vs Rayleigh for -6K Temperature Difference for a) 0.6096m Height and b)1.22m Height and 0.0254m Sill depth as a function of porosity*

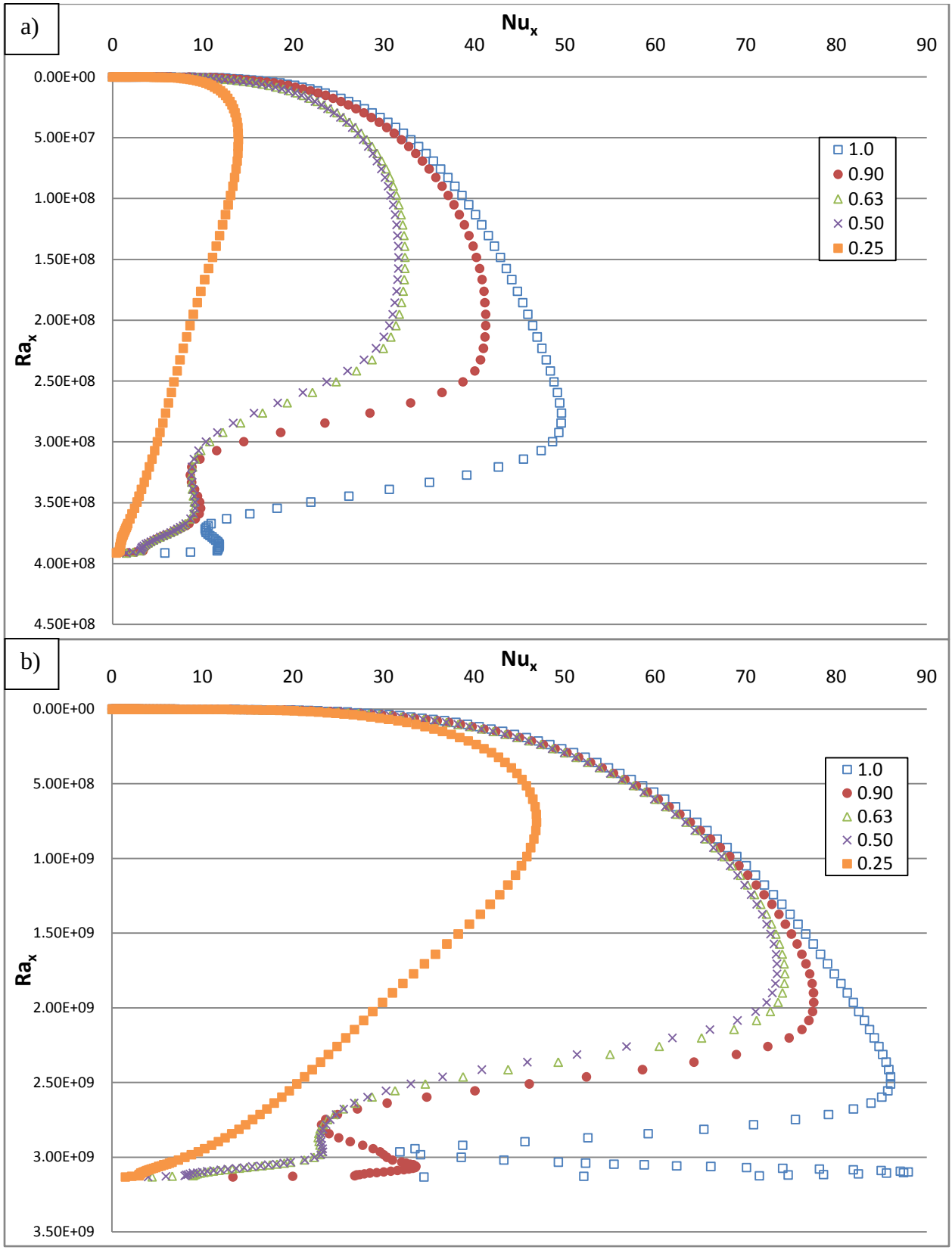

Fig.4.20. *Nusselt vs Rayleigh for -15K Temperature Difference for a) 0.6096m Height and b)1.22m Height nd 0.0254m Sill depth as a function of porosity*

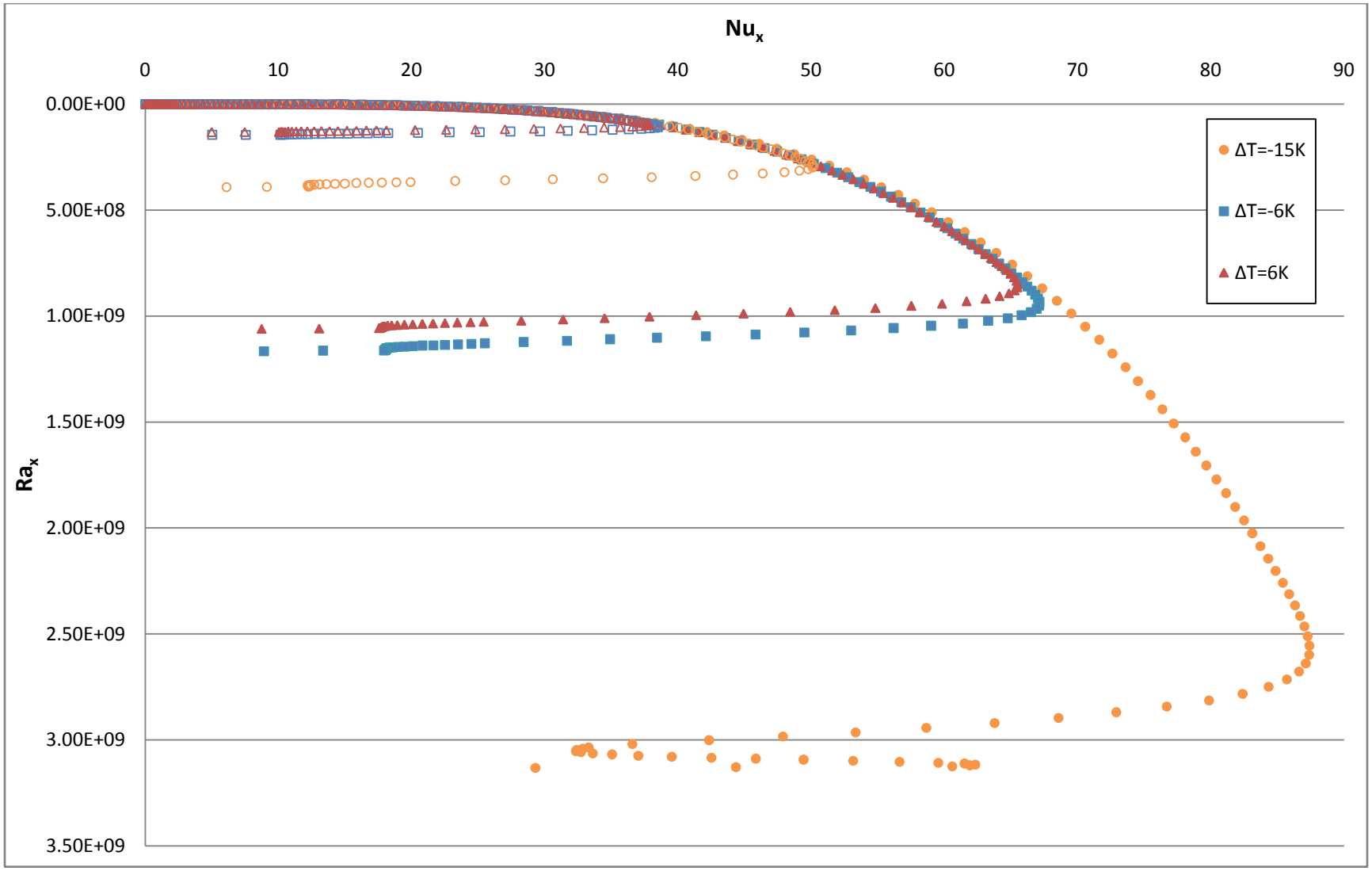

Fig.4.21. *Nusselt vs Rayleigh for γ=1.0 and 0.0125m sill depth*

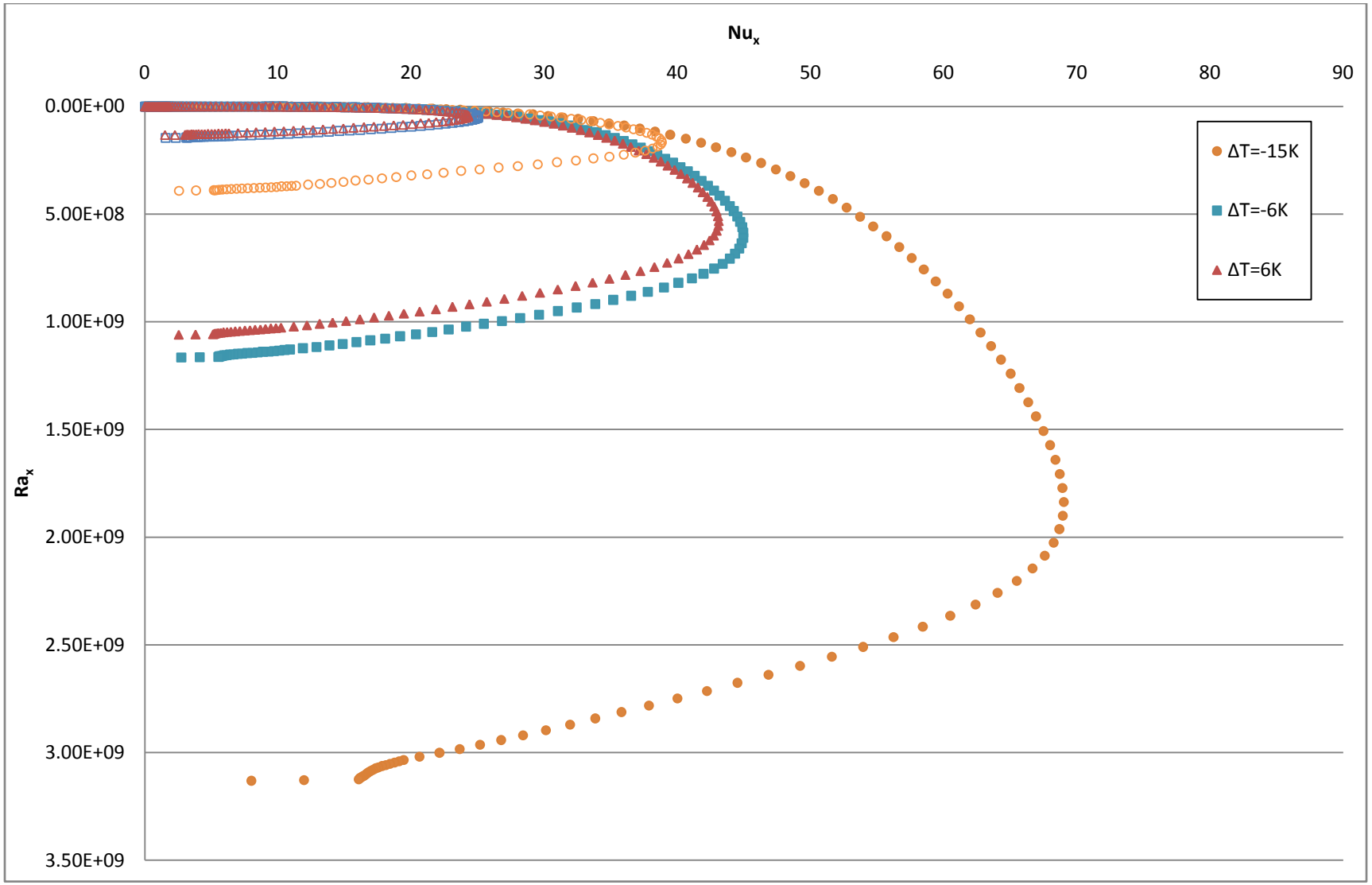

Fig.4.22. *Nusselt vs Rayleigh for γ=0.63 and 0.0125m sill depth*

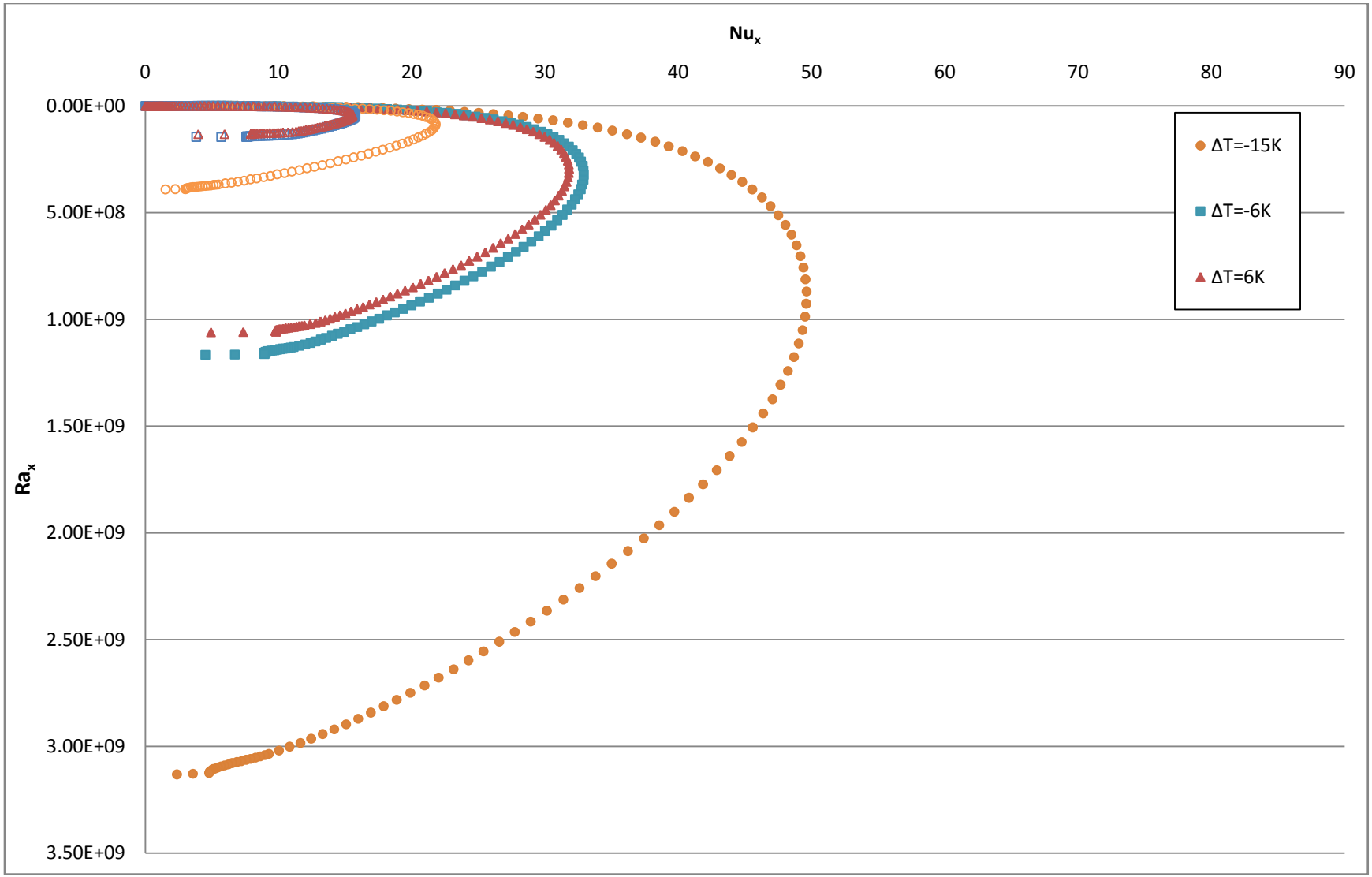

Fig.4.23. *Nusselt vs Rayleigh for γ=0.25 and 0.0125m sill depth*

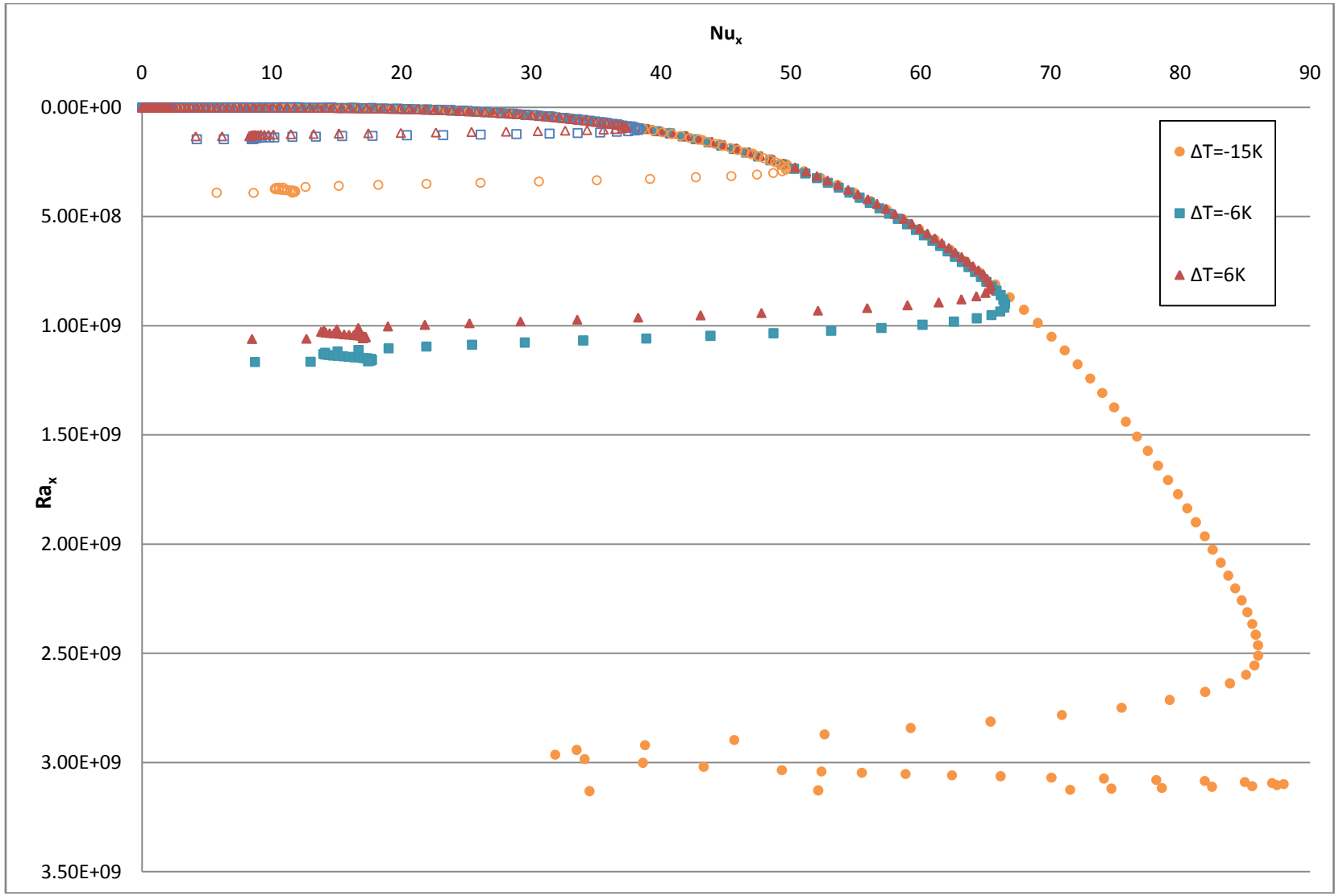

Fig.4.24. *Nusselt vs Rayleigh for γ=1.0 and 0.0254m sill depth*

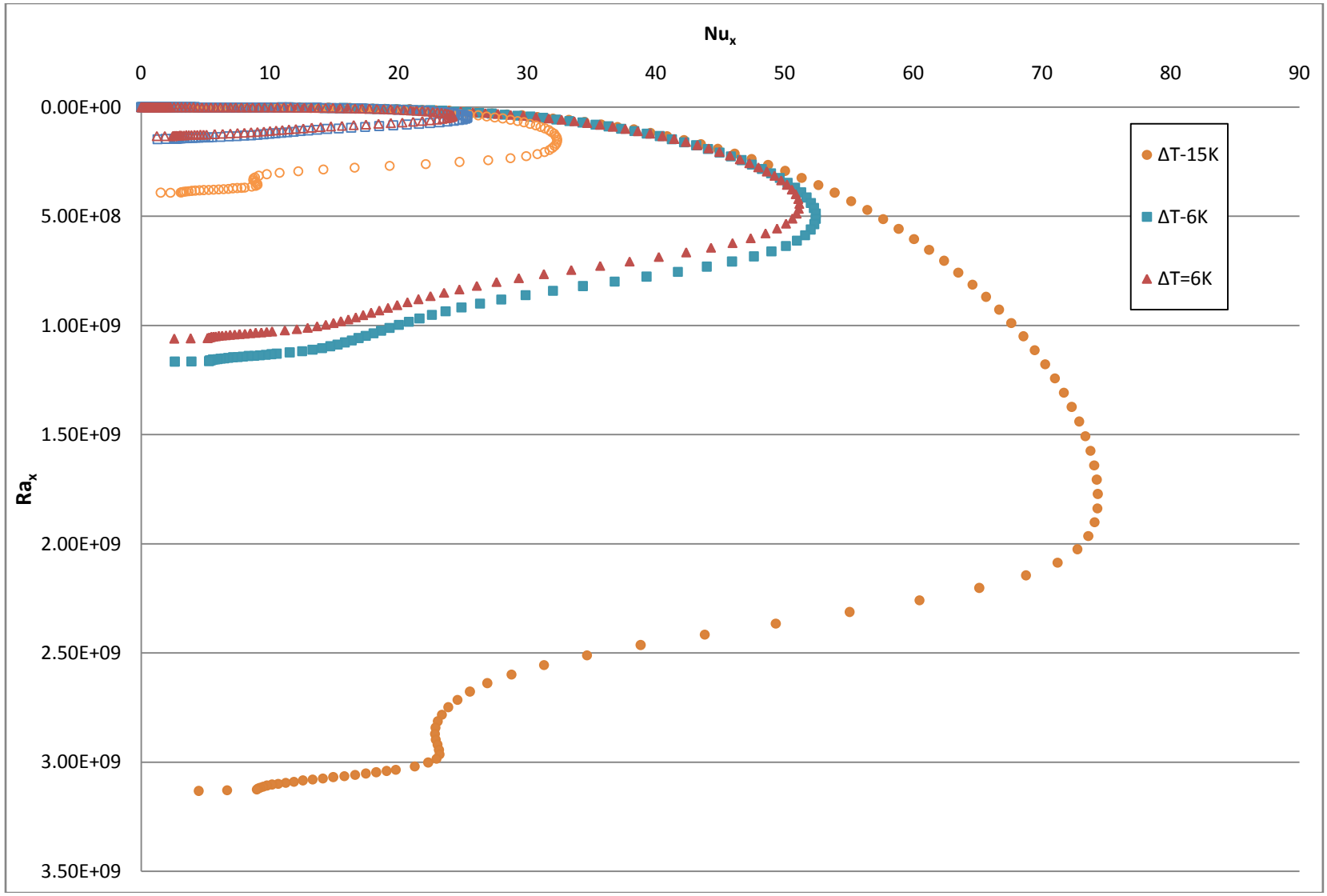

Fig.4.25. *Nusselt vs Rayleigh for γ=0.63 and 0.0254m sill depth*

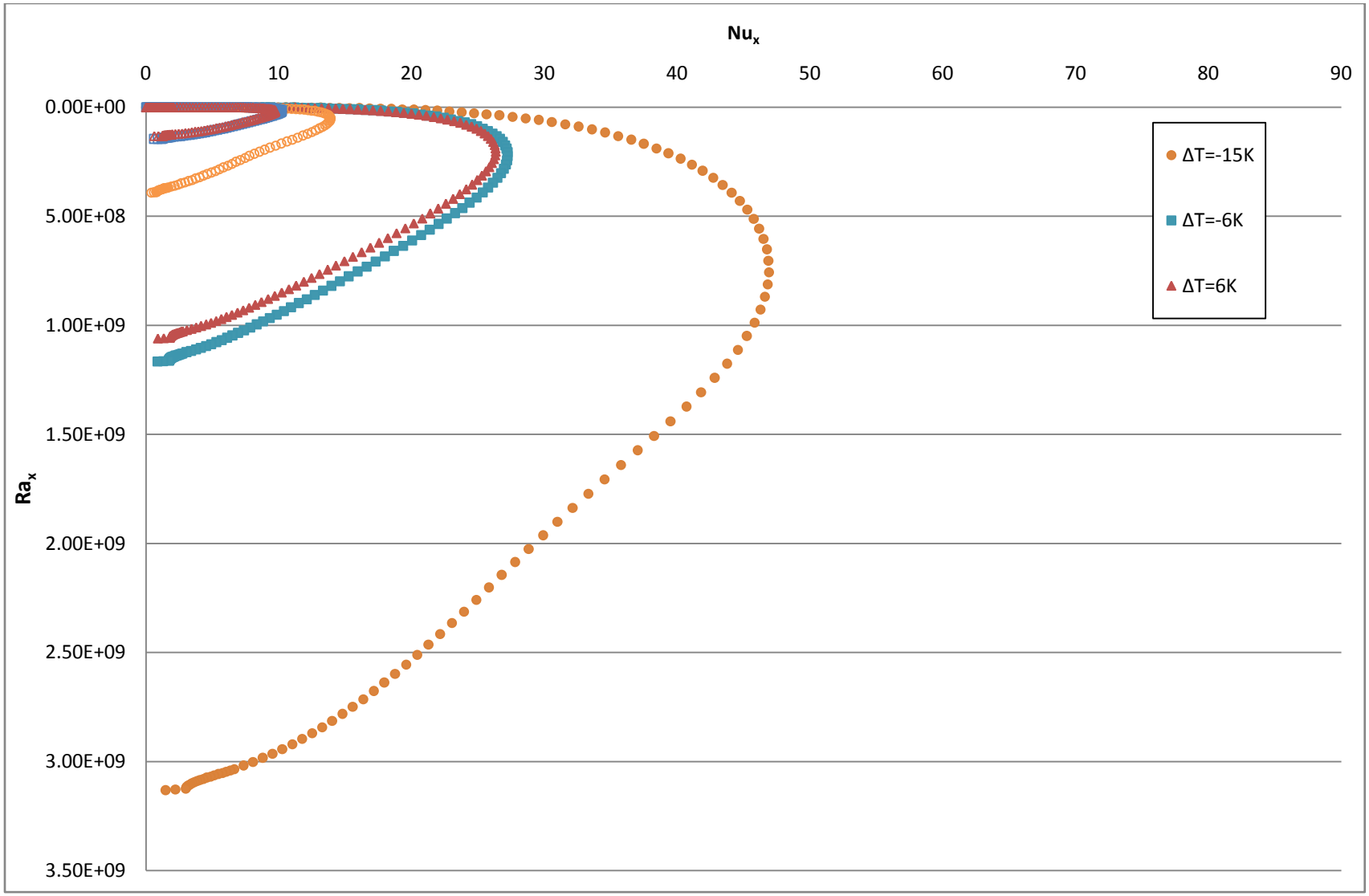

Fig.4.26. *Nusselt vs Rayleigh for γ=0.25 and 0.0254m sill depth*

4.3.3 AVERAGED RESULTS

The previous non-dimensionalized plots were formulated at the local level. Often for faster comparisons, averaged Nusselt numbers based on these local values are calculated. Empirical correlations are typically based on these averaged Nu values. The equation for the averaged Nusselt, $\overline{Nu_L}$, is

$$\overline{Nu_L} = \frac{\overline{h}L}{k} \qquad 4.1$$

where $\overline{h}$ is the area-weighted average of the local heat transfer coefficient along the plate and L is the total length of the plate, in this case the height of the window. The Rayleigh number is the same as in Eq.2.22, with L as the length of the plate.

Previously the analytical solution to the flat plate was presented from Ostrach[1953] and LeFevre [1956]. In Churchill [1975], the following correlation was developed for the average heat transfer for $Ra_L \leq 10^9$

$$\overline{Nu_L} = 0.68 + \frac{0.670Ra_L^{1/4}}{\left[1+(0.492/Pr)^{9/16}\right]^{4/9}} \qquad 4.2$$

It was stated before current enclosure correlations are inappropriate for comparison, since, in these models, the assumptions begin to break down at very low porosities. In order to highlight this, the following enclosure correlation from Shewen et al [1996] has been presented with these results for Aspect Ratios ≥ 40 and $Ra \leq 10^6$,

$$\overline{Nu_L} = [1 + (\frac{0.665Ra^{1/3}}{1+(\frac{9000}{Ra})^{1.4}})^2]^{1/2} \qquad 4.3$$

The heat transfer coefficient was averaged over the length of the window, with approximately 125 values. Plots for the averaged values for the 0.0254m and 0.0127m sill depths are shown in Figure 4.27 a) and b) respectively.

As seen from both these plots all the values taken from the model follow the same arc as the correlations. The flat plate Churchill curve follows very closely with the equivalent model results from the 1.0 porosity case. In both cases, the high porosities fall between the two correlations, while the 0.25 porosity case falls below the Shewen correlation. The vast majority of insect screening material available for use in homes or businesses has porosity of around 0.40 or higher. Any lower than that and low visibility through the screen can start being a problem. Usually the low porosity screens are intended for greenhouses or industrial applications.

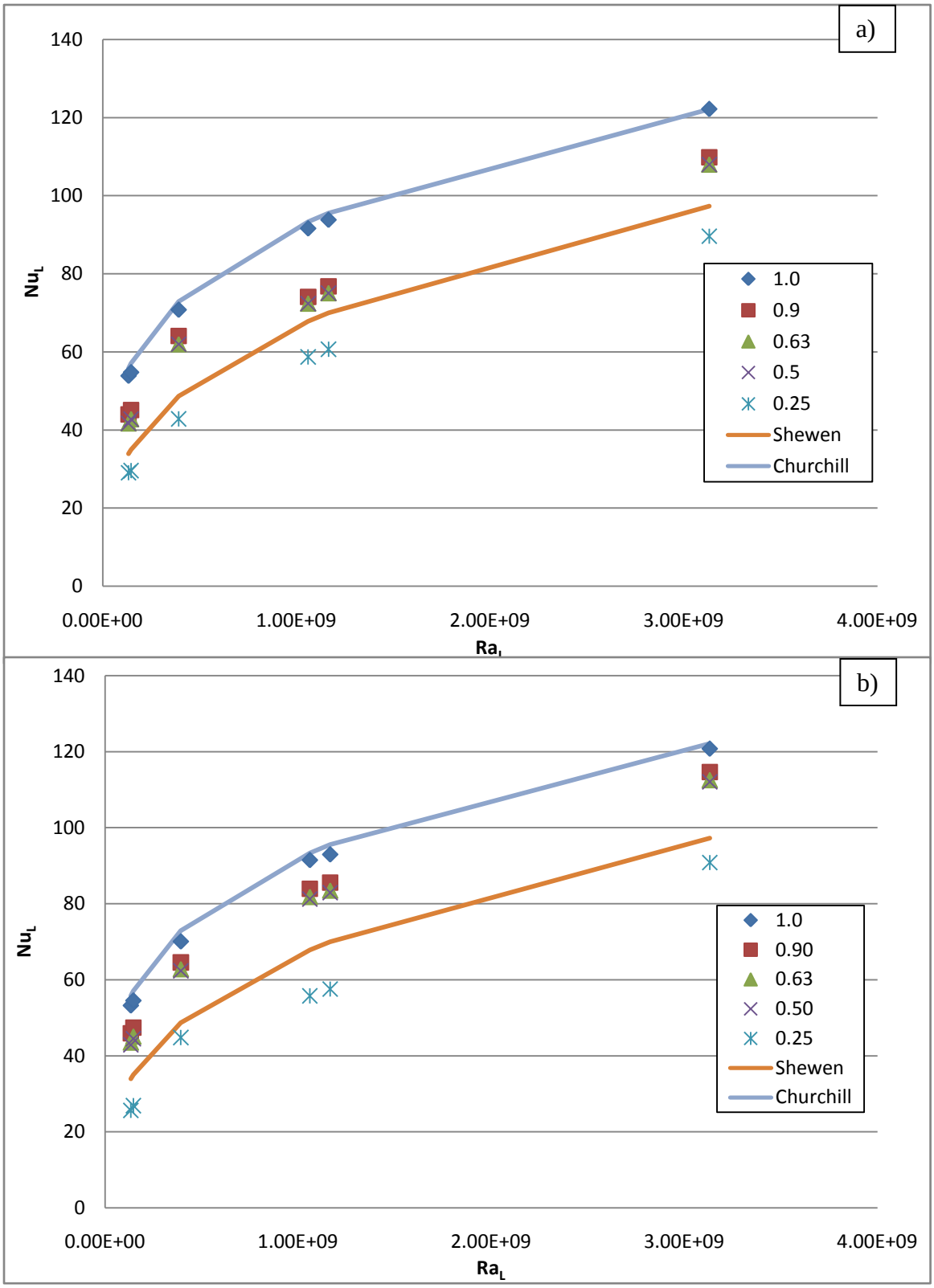

Fig.4.27. *Average Nu vs Ra for a) 0.0127m and b) 0.0254m sill depth with Churchill [1975] flat plate and Shewen [1996] enclosure correlations.*

4.4 RESISTOR NETWORK

4.4.1 RESISTOR SETUP

The results presented so far have been focused on flow patterns and the physics of adding screens to windows. In order to be more useful for building sciences, a more general approach is required in finding the heat transfer rates. Running the CFD model involves many complex equations and potentially long computing and analyzation time. Ideally a simplified model would be used that can be solved quickly by correlations found by the CFD model by using only known temperatures to get the heat transfer.

The resistor network simplifies the system by dividing each heat transferring surface into a layer. The layered system assumes that each surface is held at a constant temperature and transfers heat in individual paths to the other layers. This follows the centre of glass approach when studying windows, where essentially when heated, windows have a constant temperature across the glass except for the outer edges close to the frame. How easily the layers transfer heat between each other is measured by the proportionality coefficient h, and therefore the inverse of h can be considered a resistance. If the resistances are a function of temperature, then the only required inputs to solve the system would be the different layer temperatures. The dependence of the resistance can be found by running the CFD models. By taking the heat fluxes from each model run, the resistances can be calculated for specific conditions. By plotting the resistances to the various temperature conditions, a correlation can be developed and thereby the heat fluxes can be found for ideally any temperature difference.

With the introduction of a layered system, a screen temperature, T_s, must now be introduced. A heated screen mimics the effects of solar radiation, where on a very sunny day, the screen could potentially have a much higher temperature than the window or the ambient surroundings. Since the screen was assumed to have no thermal mass, any energy that enters it must leave, and since the walls above and below the screen were adiabatic, there is an implied condition that any heat transfer from the screen must be **into** the system. While energy can be put into the system through the screen as radiation, represented by a heat flux Q_s, it cannot leave the

system in the same manner. The screen does not act like a black body, where it is able to radiate out the same amount of energy than it can receive. Each test case for the heated screen must be checked for realistic behaviour. When Q_s is positive, there is energy entering the system through the screen, however if Q_s is negative, then energy is trying to leave through the screen and should be neglected. This would be a condition where the screen is lower than the ambient or window temperatures, so the system would attempt to transfer heat to the screen. A screen temperature lower than both the ambient or window temperatures is not a realistic condition, which would imply a 'chilled' screen. There is the possibility of allowing a slightly negative Q_s value to represent some small amount of radiation heat transfer out from the screen, but this would depend on the material properties of the screen and changes with porosity and material type.

In FLUENT, the approach was to model the screen for heat transfer similar to a radiator or heat exchanger, where air passing through this boundary would have a certain amount of energy transferred to it. The convective heat transfer equation is applied,

$$Q_s = h(T_s - T_f) \qquad 4.4$$

where Q_s is the heat flux (W/m^2), in this case due to solar radiation, h (W/m^2-K) is the heat transfer coefficient and T_f (K) is the temperature of the fluid as it passes through the screen. In this resistor network, we are trying to determine Q_s, we input the value of T_s and T_f is calculated by the model as it is run. Thus the parameter needed is *h*.

The difficulty in this approach is in the calculation of the heat transfer coefficient *h*. In Miguel [1998 b], the screen properties were only analyzed for momentum transfer, not heat, thus the change in *h* for fluid velocity is not empirically known. The coefficient *h* is based on the geometry of the body that the fluid flow passes over as well as the fluid speed. There are several correlations that could apply to the geometry of the screen. One approach is to assume the system is the same as flow over a cylinder, which there are many correlations for. Adding to the complexity of this situation is that at the bottom of the screen cavity, there are air velocities that are interacting in cross flow with the screen, which can be considered forced convection, while the screen is still affected by buoyancy forces, thus, very close to the screen, there is the

possibility of mixed convection. In order to determine this, the Grashof and Reynolds numbers are required,

$$Gr = \frac{g\beta(T-T)D^3}{v^2} \qquad 4.5$$

$$Re = \frac{VD}{v} \qquad 4.6$$

where *Gr* is the grashof number, similar to *Ra*, where it is a ratio of buoyancy to viscous forces, *Re* is the Reynolds number and is a ratio of the inertial to viscous forces, *D* is the diameter of the wire, *V* is the velocity of the air and *v* is the kinematic viscosity, or

$$v = \frac{\mu}{\rho} \qquad 4.7$$

The ratio of *Gr* and *Re* determines the type of convection that is present, either forced or natural, bounded by the following conditions:

$\frac{Gr}{Re^2} \gg 1$ natural convection

$\frac{Gr}{Re^2} \ll 1$ forced convection

$\frac{Gr}{Re^2} \approx 1$ mixed convection

Taking *V* as an averaged velocity through the screen from the previous non-heated screen conditions, for each wire diameter and temperature condition used in this model, this ratio was found to be between 0.1 and 0.7, confirming that there is mixed convection.

For mixed convection on a cylinder, the following steps to determine the Nusselt number (and thus *h*) was determined in Morgan [1975] based on previous work done for combined convection for low speed flows in Hatton [1970], first the thin layer Nusselt number is found,

$$Nu^T = 0.772\overline{C_l}Ra^{1/4} \quad 4.8.$$

where Nu^T is the thin layer Nusselt number and $\overline{C_l}$ is a universal function of Prandtl. For air with Pr = 0.71, $\overline{C_l}$= 0.515. With this, the average Nusselt number over the body is found.

$$Nu_l = \frac{2f}{\ln\left(1+\frac{2f}{Nu^T}\right)} \quad 4.9.$$

Where

$$f = 1 - \frac{0.13}{(Nu^T)^{0.16}} \quad 4.10.$$

Using this laminar Nusselt number, the Reynolds number for where forced and natural convection are equal is found by the following equation,

$$Re_i = \left[\frac{Nu_l}{a\left(\frac{Pr}{0.71}\right)^{1/3}}\right]^{1/n} \quad 4.11.$$

Where *a* and *n* are parameters that are dependent on Re for the flow over the cylinder. Based on this Re_i, an effective Reynolds number is found in order to see how far away the system is from the case of equal natural and forced convection,

$$Re_{eff} = [(Re_i + Re\cos\varphi)^2 + (Re\sin\varphi)^2]^{1/2} \quad 4.12$$

where φ is the angle of attack of the freestream on the cylinder. For a cross stream, φ = 90°. Finally the mixed convection Nusselt number is found using the following,

$$Nu = aRe_{eff}{}^n\left(\frac{Pr}{0.71}\right)^{1/3} \quad 4.13.$$

The heat transfer coefficient can be found by equating this to the Nusselt number in Eq. 4.1, replacing L with D for the wire diameter. This correlation determines the heat transfer along the face of each cylinder. Unfortunately FLUENT applies the inputted *h* as constant along the entire screen face. Therefore the *h* found and the *h* required contains different areas, and must be converted to reflect the correct physics. The ratio of the surface area where convection is taking place A_s, to the total frontal area A_T, must be found, and the heat transfer coefficient should be multiplied by this ratio. This surface area is dependent on the mesh geometry, and in order to analyze this, a small section of the screen must be looked at where it can be divided by symmetry. An example for 4 cylindrical wires meshed in a square configuration is shown in Fig.4.28.

The axis of symmetry can divide the wires in half, thus the surface area of a semi-circular cylinders must be found and then multiplied by four for the four wires. As a result of the overlapping of the wires in the corners, the surface area should not be double accounted; therefore when the perimeter of the semi-circle is multiplied by the width of the cylinder, the semi-circle radius must be subtracted from this width on both sides.

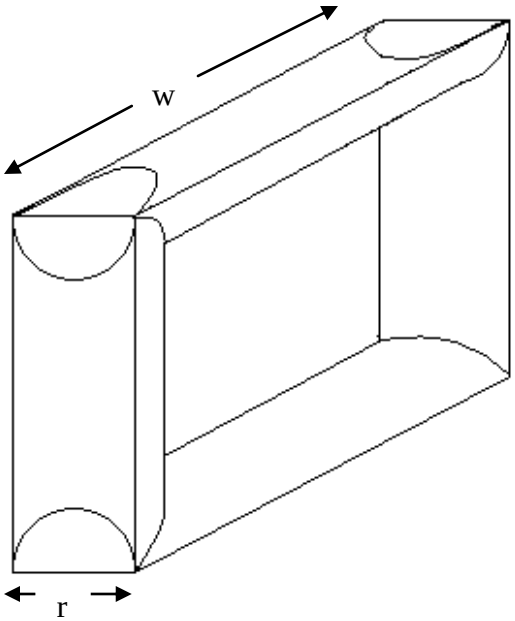

$$A_s = 4\pi r(w - 2r)$$
$$A_T = w^2$$

Fig.4.28. *Calculation of surface areas of convection for a square cylindrical wire mesh.*

Multiplying this ratio to the *h* found through correlation would give a better approximation of the true *h* needed to be applied across the screen face. With this value, the rest of the resistance network values can be found. This is one of many possible approaches, since there are several correlations that may apply to this situation. In order to determine the correct approach, experimentation may be required or modelling a small 3-D section of the screen. Computer modelling would be preferred because of the difficulty that arises in creating an isothermal screen through experimentation.

4.4.2 RESISTOR EQUATIONS

The layered setup for this window and insect screen model is shown in Fig.4.29

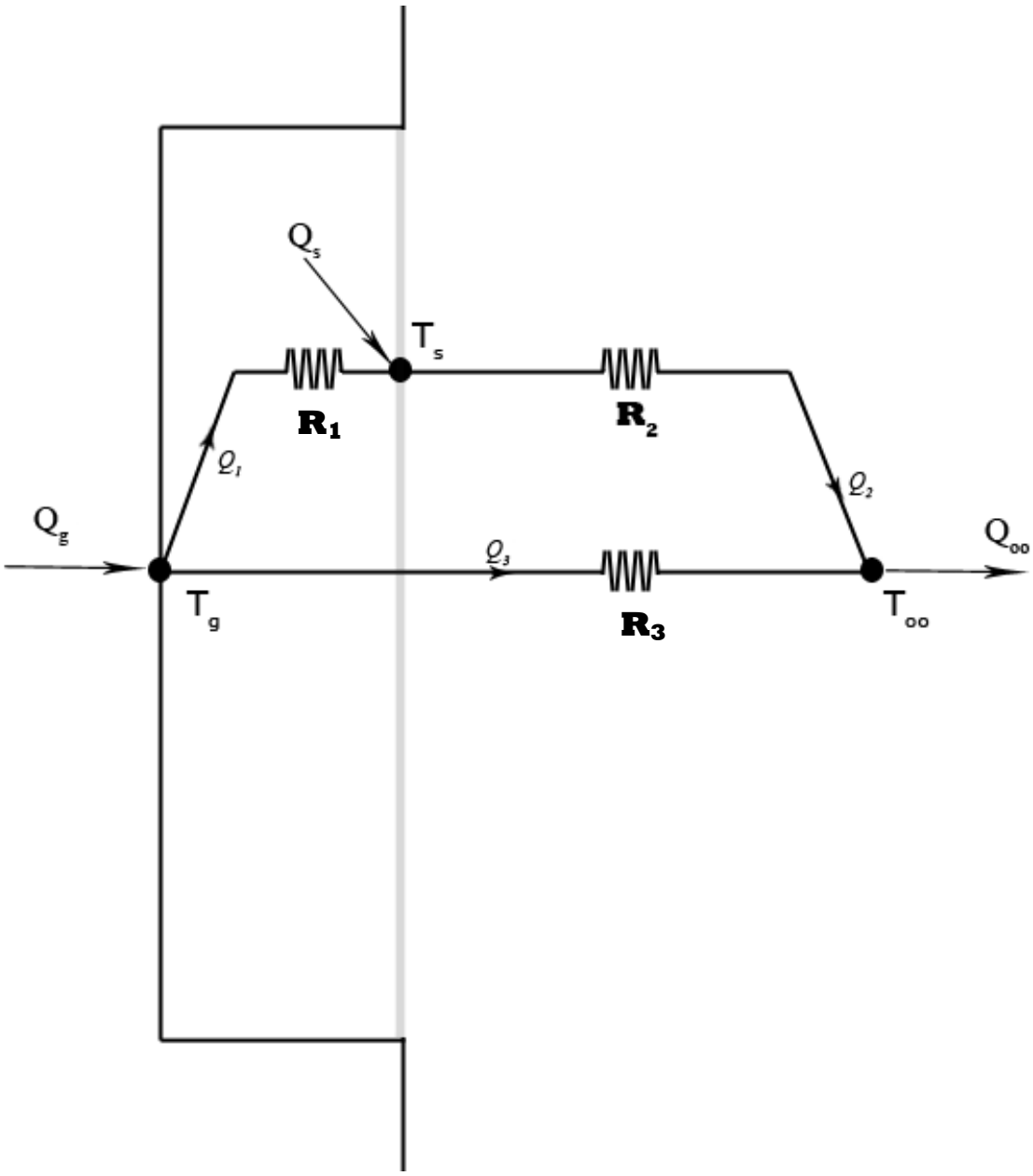

Fig.4.29 *Resistor network for a window and insect screen configuration*

For this insect screen system there are three paths for heat to flow, giving three resistances. The first, Q_1, is between the window and the screen, giving a resistance of R_1, the second, Q_2, is between the screen and the room, giving a resistance, R_2, and the third, Q_3, is heat transfer from the room directly to the window, giving the final resistance R_3. Energy is allowed to enter or leave the system through the window, Q_g, through the room, Q_∞ or through the screen, Q_s. Performing an energy balance on the system shown in Fig.4.29 gives the following equations.

$$Q_g = Q_1 + Q_3 = \frac{(T_g - T_s)}{R_1} + \frac{(T_g - T_\infty)}{R_3} \qquad 4.14$$

$$Q_s = Q_2 - Q_1 = \frac{(T_s - T_\infty)}{R_2} - \frac{(T_g - T_s)}{R_1} \qquad 4.15$$

The known values taken from the FLUENT model are Q_g, Q_s and the temperatures T_s, T_g and T_∞. This leaves all three resistances values (and their equivalent heat fluxes Q_1, Q_2 and Q_3) as unknowns. As such, there are not enough equations to solve for the unknowns.

Some simplifications can be made, depending on the model setup. When there is no screen, the only path is from the window to the room, thus Q_1 and Q_2 are eliminated from Eq.4.14 and 4.15, leaving only Q_3. Rearranging for R_3 gives

$$R_3 = \frac{(T_g - T_\infty)}{Q_g} \qquad 4.16$$

Additionally, from Equations 4.14 and 4.15, it can be seen that the heat flux paths Q_1, Q_2 or Q_3 can drop to zero when two set temperatures are equal, thus eliminating a resistance path, giving enough equations to solve for the rest.

When the glass temperature, T_g, is equal to the screen temperature, T_s, the heat fluxes become $Q_1 = 0$, $Q_2 = Q_s$ and $Q_3 = Q_g$. This eliminates R_1 from the equations, and the other two resistances can be solved for. R_3 is still defined as previously in Eq.4.16, but now R_2 can be calculated as

$$R_2 = \frac{(T_s - T_\infty)}{Q_s} \qquad 4.17$$

When the screen temperature, T_s, is equal to the ambient temperature, T_∞, the heat fluxes become $Q_1 = -Q_s$, $Q_2 = 0$ and $Q_3 = Q_g + Q_s$. This eliminates R_2 from the equations, giving the following for the remainder,

$$R_1 = -\frac{(T_g - T_s)}{Q_s} \qquad 4.18$$

$$R_3 = \frac{(T_g - T_\infty)}{Q_g + Q_s} \qquad 4.19$$

One additional set can be derived when the glass and ambient temperature are equal; however that condition was not modelled here, so these equations have not been included.

When there are not equal temperatures, another assumption must be made in order to create additional equations to solve for the resistances. The models must be perturbed, which presumes that by changing the value of T_g by a very small amount the resistance values will not change. Inserting a new perturbed glass temperature, $T_g^* = T_g + 0.1K$, into equations 4.14 and 4.15, two new equations can be created.

$$Q_g^* = Q_1^* + Q_3^* = \frac{(T_g^* - T_s)}{R_1} + \frac{(T_g^* - T_\infty)}{R_3} \qquad 4.20$$

$$Q_s^* = Q_2 - Q_1^* = \frac{(T_s - T_\infty)}{R_2} - \frac{(T_g^* - T_s)}{R_1} \qquad 4.21$$

Only one of these new equations is needed. Inserting Eq.4.21 into Eq.4.15, R_1 and R_2 can be found

$$R_1 = \frac{T_g^* - T_g}{Q_s - \grave{Q_s}} \qquad 4.22$$

$$R_2 = \frac{T_s - T_\infty}{Q_s + \frac{(Q_s - Q_s^*)(T_g - T_s)}{\grave{T_g} - T_g}} \qquad 4.23$$

Finally, inserting Eq.4.19 into 4.21, R_3 can be found,

$$R_3 = \frac{(T_g - T_{oo})}{Q_g - \frac{(Q_s - Q_s^*)(T_g - T_s)}{\grave{T_g} - T_g}} \qquad 4.24$$

With these equations, for any 3 temperatures, the resistance values can be found.

CHAPTER 5
CONCLUSION AND RECOMMENDATIONS

5.1 CONCLUSION

A numerical model of a window cavity with a variable porosity insect screen was developed using commercial Computational Fluid Dynamics software, FLUENT, in order to see what the effects of changing several system variables would be on the natural convection heat transfer rates through the cavity.

The effects were studied dimensionally for flow patterns, non-dimensionally for heat transfer patterns and in a simplified resistor network form for integration into ongoing window modelling at the University of Waterloo Solar Lab.

For the dimensional analysis, the following can be drawn from the study:

- Adding an insect screen to a window greatly reduces the flow speed and increases the thermal boundary layer. These effects become greater as the porosity of the screen is decreased.
- At 0.0127m sill depths, the space between the window and screen is so small that recirculation does not occur at any porosity. Increasing the temperature difference between the window and ambient air at this sill depth has no significant effect on the flow structure; it only increases the flow velocity slightly. As the porosity is decreased, the air movement in the cavity decreases, approaching still air, similar to a double pane window.
- With a sill depth of 0.0254m, there is recirculation present inside the window cavity. At high porosities there is some recirculation back up along the cavity, as well as a small recirculation zone at the very bottom corner. As the porosity is decreased, the recirculation begins to fill the entire cavity. These effects are made larger by increasing the temperature difference or by increasing the window height.

For the non-dimensional analysis, the following can be concluded:

- As porosity is decreased, the heat transfer lessens and the Nusselt number becomes more uniform across the cavity.
- For the smaller sill depth, the end effects as the flow navigates the corner are very small. Since the screen is so close to the window does not allow enough space for different flow structures and keeps the flow in the cavity all the way to the bottom, so the heat transfer decreases steadily in the lower portion of the window cavity.
- In the end effects, a jump in the heat transfer indicates a small recirculation zone. As the porosity decreases, these recirculation zones decrease, possibly because of the lower velocities throughout the cavity. This greatly lessens the end effects on the heat transfer.
- The larger sill depth shows much more heat transfer changes due to the end effects. The spacing is large enough to allow for recirculation back up along the screen, as well as large recirculation in the bottom corner.
- There is very strong similarity between the two window heights, and only deviate in each porosity with the magnitude of the end effects, the only difference being the smaller window height experiences less of a heat transfer jump
- The averaged values follow the same trend as empirical correlations for a flat plate and an enclosure and the majority of the data fits between the two correlations. The 0.25 porosity falls below the enclosure correlation, though it was noted that the enclosure correlation may not be quite appropriate for comparison. The correlation likely over predicts the heat transfer since the correlation was developed for two isothermal walls, while this data set was for one isothermal wall and a porous medium touching an infinite reservoir.

From the resistor network methedology, the following can be found:

- A methodology was proposed in order to determine the resistor values
- Calculating the heat transfer coefficient through the screen is difficult to determine as there are many correlations that could possibly apply. Determining which would be best would require difficult experimentation or 3-D modelling of a small section of screen.
- Once the h value is found, the resistor equations can be used to determine the resistor values and heat fluxes.
- A heat flux out of the screen is not a realistic condition, thus any conditions that produce Q_s as negative should be disregarded.

5.2 RECOMMENDATIONS

- In this study, laminar conditions were assumed. In the 1.22m windows, the critical Rayleigh number was reached. A possible follow up could include the effects of turbulence, which would allow larger windows to be analyzed, including very large patio doors, which almost always have sliding insect screens attached.
- A similarity correlation could be examined from the non-dimensionalized results
- In determining the heat transfer coefficient, only one correlation was presented. Other methods to determine h could be through a 3-D model of a very small section of screen with mixed convection.
- Several data sets are required for the resistor network correlation. The data sets should be based on the absolute temperature difference.
- There should be multiple entries for each temperature difference (two different temperature sets for a single temperature difference) for each resistance plot to make sure there is no dependence on another variable.
- Include much larger temperatures on the positive side for summer conditions and strong solar heating.
- Realistically, since Q_s represents solar heating, any case where Q_s is strongly negative should not be included since technically heat can enter the system through the screen as

radiation, but it cannot leave through the screen. However, they may be used for comparison for the positive temperature differences.

- In order to see at what porosity the model assumptions break down, experimentation may be required. This may also include running models with an intermediate porosity between 0.50 and 0.25. In Miguel [1997], there are pressure drop coefficients for 0.36.

REFERENCES

Abodahab, N., & Muneer, T. (1997). *Free convection analysis of a window cavity and its longitudinal temperature profile*. Energy Convers. Mgmt, 39, 257-267.

Bartzanas, T., Boulard, T., & Kittas, C. (2002*). Numerical simulations of the airflow and temperature distribution in a tunnel greenhouse equipped with insect-proof screen in the openings*. Computers and Electronics in Agriculture, 34, 207-221.

Brunger, A., West, L.E. (1998). Measurement of SHGC and U-Valure of Windows with Insect Screens. Prepared Report for NRCan No. EA-0721-98-3256.

Brunger, A., Dubrous, F., & Harrison, S. (1999). *Measurement of the Solar Heat Gain Coefficient and U Value of Windows with Insect Screens*. ASHRAE Transactions, 105, 1038-1044.

Collins, M.R., & Wright, J.L. (2006). *Calculating Center-Glass Performance Indices of Windows with a Diathermanous Layer*. ASHRAE Transactions, 112, 22-29.

Churchill, S.W., & Chu, H.H.S. (1975). *Correlating Equations for Laminar and Turbulent Free Convection from a Vertical Plate*. Int. J. Heat Mass Transfer, 18, 1323.

Cuddihy, J., Kennedy, C., & Byer, P. (2005). *Energy Use in Canada: environmental impacts and opportunities in relationship to infrastructure systems*. Canadian Journal of Civil Engineering, 32, 1-15.

Fatnassi, H., Boulard, T., Poncet, C., & Chave, M. (2006). *Optimisation of Greenhouse Insect Screening with Computational Fluid Dynamics.* Biosystems Engineering, 93, 301-312.

Forccheimer, P. (1901). *Wasserbewegung durch boden*. Z. Ver Deustsch, 45, 1782-1788.

Gebhart, B., Jaluria, Y., Mahajan, R.L., & Sammakia, B. (1988). *Buoyancy-Induced Flows and Transport*. Washington DC : Hemisphere Publishing.

Gustavsen, A., Thue, J.V. (2007). *Numerical Simulation of Natural Convection in Three-dimensional cavities with a high vertical aspect ratio and a low horizontal aspect ratio*. Journal of Building Physics, 30, 217-240

Hatton, A.P., Janes, D.D., Swine, H.W. (1970). *Combined Forced and Natural Convection with Low Speed Airflow over Horizontal Cylinders*. J. Of Fluid Mechanics, 42, 17-31.

Incropera, F.P., DeWitt, D.P. (2002). *Fundamentals of Heat and Mass Transfer 5th Ed*. Hoboken N.J., U.S.: John Wiley & Sons, Inc.

LeFevre, E.J. (1956). *Laminar Free Convection from a Vertical Plane Surface.* Proc. Ninth Int. Congr. Appl. Mech., 4, 168.

Miguel, A.F., van de Braak, N.J., & Bot, G.P.A. (1997). *Analysis of the Airflow Characteristics of Greenhouse Screening Materials*. Journal of Agricultural Engineering Research, 67, 105-112

Miguel, A.F., van de Braak, N.J., Silva, A.M., & Bot, G.P.A. (1998 a). *Physical Modelling of Natural Ventilation Through Screens and Windows and Greenhouses*. J. Of Agriculture Engineering Res. 70, 165-176

Miguel, A.F. (1998 b). *Airflow through porous screens: from theory to practical considerations*. Energy and Buildings, 28, 63-69.

Ménard, M. (2005). *Canada a Big Energy Consumer: A Regional Perspective*. Statistics Canada Publication Catalogue No.11-621-MIE2005023

Morgan, V.T. (1975). *Overall Convective Heat Transfer From Smooth Cylinders.* Advances in Heat Transfer, 11, 199-264.

Ostrach, S. (1953). *An Analysis of Laminar Free Convection Flow and Heat Transfer About a Flate Plate Parallel to the Direction of the Generating Body Force*. National Advisory Committee for Aeronautics Report 111.

Public Health Agency of Canada, (2006). *West Nile Virus – Protect Yourself*. Retrieved 2007, from www.westnilevirus.gc.ca

Rohsenow, W.M., Hartnett, J.P., Cho, Y.I. (1998). *Handbook of Heat Transfer 3rd Ed.* New York N.Y., U.S.: McGraw Hill

Shewen, E., Hollands, K.G.T., Raithby, G.D. (1996) Heat Transfer by Natrual Convection Across a Vertical Air Cavity of Large Aspect Ratio. Journal of Heat Transfer, 188, 993-995.

U.S. Department of Energy, (2006). *Window Operating Types*. Energy Efficiency and Renewable Energy. Retrieved 2007, from www.energysavers.gov/your_home/windows_doors_skylights/index.cfm/mytopic=13460

Versteeg, H.K., Malalasekera, W. (2007) An Introduction to Computational Fluid Dynamics 2nd Ed. Harlow, Essex, U.K.: Pearson Education Limited.

Wright, J.L., & Kotey, N.A. (2006). *Solar absorption by each element in a glazing/shading layer array*. ASHRAE Transactions, 112, 3-12

Wright, J.L., Jin, H., Hollands, K.G.T., & Naylor, D. (2006). Flow Visualization of natural convection in a tall air-filled vertical cavity. Int. Jour. Of Heat and Mass Transfer, 49, 889-904.

Wright, J.L., Collins M.R., Kotey, N.A., & Barnaby, C.S. (2009). *Improving Cooling Load Calculations for Fenestration with Shading Devices, Final Report.* ASHRAE 1311-RP

Zeng, M., & Tao, W.Q. (2003). *A Comparison study of the convergence characteristics and robustness for four variants of SIMPLE-family at fine grids*. Engineering Computations, 20, 320-340.

APPENDIX A: MESHING

Table A.1. *Meshing Size Information for 0.6096m Height, 0.0127m Sill*

	Cells	Faces	Nodes
Window Cavity (Quad)	3250	6651	3402
Screen Zone (Quad)	125	376	252
Open Air Zone (Mixed)	24553	39917	15365
Total	27928	46694	18767

Table A.2. *Meshing Size Information for 0.6096m Height, 0.0254m Sill*

	Cells	Faces	Nodes
Window Cavity (Quad)	6375	12926	6552
Screen Zone (Quad)	125	376	252
Open Air Zone (Mixed)	24553	39917	15365
Total	31053	52969	21917

Table A.3. *Meshing Size Information for 1.22m Height, 0.0127m Sill*

	Cells	Faces	Nodes
Window Cavity (Quad)	3900	7976	4077
Screen Zone (Quad)	150	451	302
Open Air Zone (Mixed)	22846	38019	15174
Total	26896	46146	19251

Table A.4. *Meshing Size Information for 1.22m Height, 0.0254m Sill*

	Cells	Faces	Nodes
Window Cavity (Quad)	7650	15501	7852
Screen Zone (Quad)	150	451	302
Open Air Zone (Mixed)	22846	38019	15174
Total	30646	53671	23026

APPENDIX B: ADDITIONAL PHOTOS

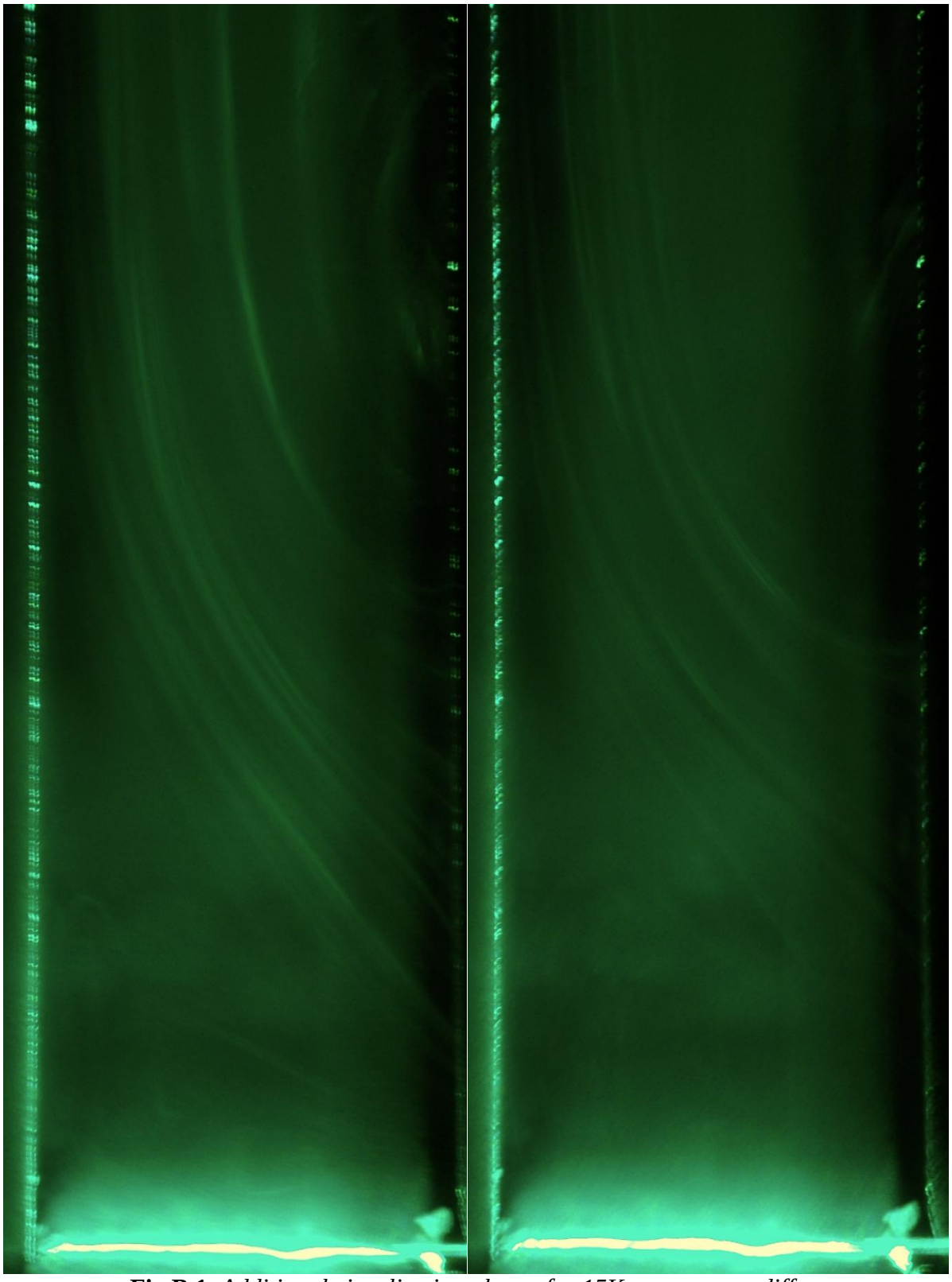

Fig.B.1. *Additional visualization photos for 15K temperature difference*

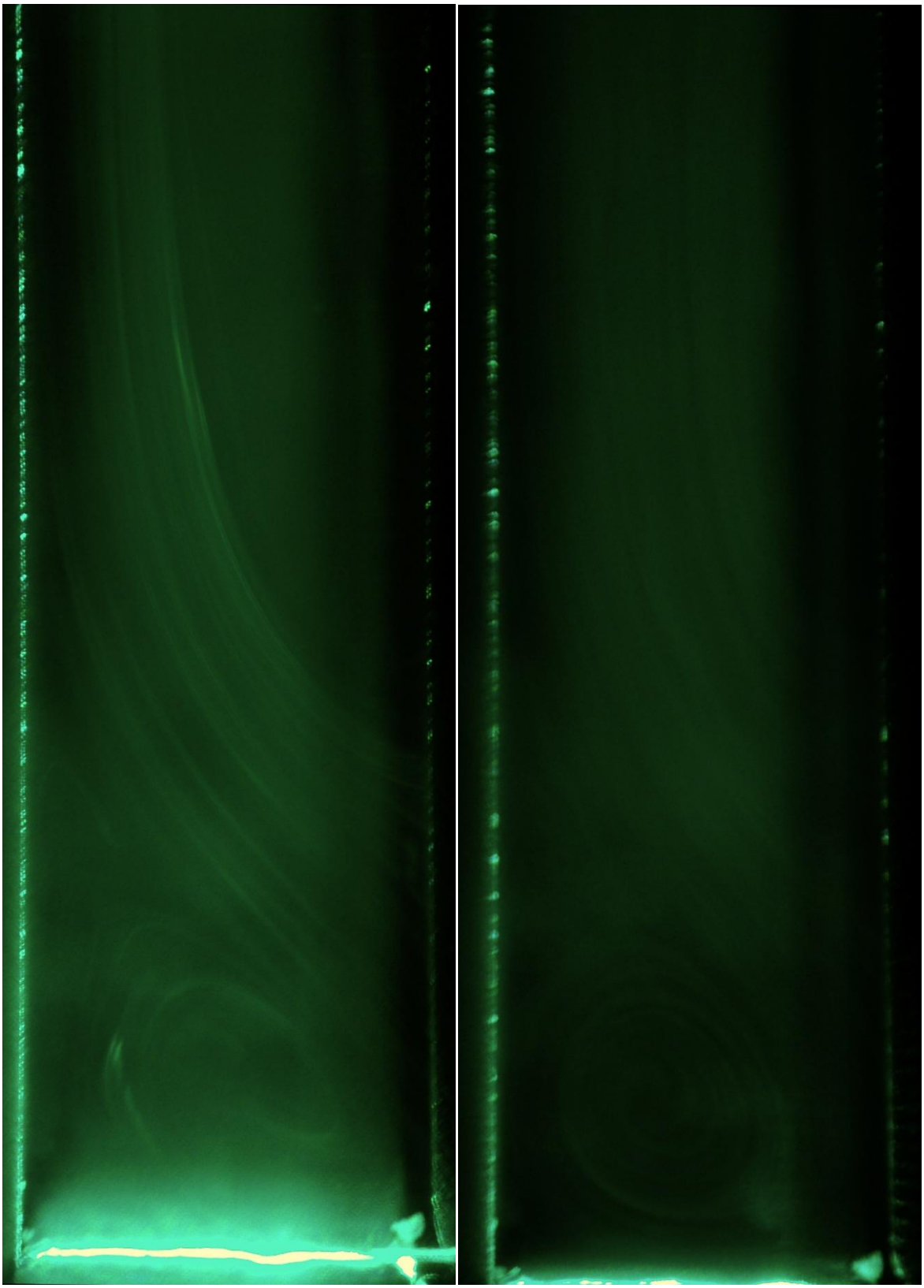

Fig.B.2. *Additional visualization photos for 26K temperature difference*